Giant planet formation and a large population study of protoplanetary disks

Apostolos Zormpas

München 2023

Giant planet formation and a large population study of protoplanetary disks

Apostolos Zormpas

Dissertation
an der Fakultät für Physik
der Ludwig–Maximilians–Universität
München

vorgelegt von
Apostolos Zormpas
aus Serres, Griechenland

München, den 13. März 2023

Erstgutachter: Prof. Dr. Til Birnstiel
Zweitgutachter: Prof. Dr. Barbara Ercolano
Tag der mündlichen Prüfung: 26. April 2023

Contents

Zusammenfassung

Unser Verständnis der Planetenentstehung und die Erforschung der Entwicklung protoplanetarer Scheiben hat sich in den letzten Jahrzehnten rasant entwickelt. Mit dem Aufkommen neuer Teleskope erhalten wir detailliertere Bilder als je zuvor, was uns hilft theoretische Modelle der Planetenentstehung besser einzugrenzen, aber auch zu Merkmalen wie Substrukturen führt, die von Planeten verursacht werden könnten. In zwei grob zusammenhängenden Studien untersuchen wir zunächst die Bildung von Riesenplaneten mit Hilfe des sich abzeichnenden Paradigmas der Kieselakkretion und führen dann eine große Populationsstudie protoplanetarer Scheiben durch, um die beobachteten Eigenschaften mit den simulierten Daten zu vergleichen. In unserer ersten Studie stellen wir fest, dass bei Verwendung einer realistischen Zustandsgleichung und Strahlungskühlung in hochkomplexen 3D-hydrodynamischen Simulationen der Planetenkern in der Lage ist, eine große Lücke zu öffnen, bevor er die für ein Runaway-Wachstum erforderliche Masse erreicht und auf diese Weise eine Übergangsscheibe entsteht. Daher können die Planeten an der Stelle des Jupiters bis zur Größe einer Super-Erde wachsen. In der zweiten Studie erklären wir den Ursprung der beobachteten Größen-Leuchtkraft-Relation (SLR) zwischen dem 68%-Effektivradius (r_{eff}) von Scheiben mit ihrer Kontinuumsleuchtkraft (L_{mm}) mit einfachen Modellen der Gas- und Staubentwicklung. Mit Hilfe von 10^5-Simulationen zeigen wir, dass ein größerer Anteil der Scheiben mit Substruktur die SLR bevölkert, wenn Planeten vorhanden sind, als wenn die Scheiben glatt sind und keine Unterstrukturen enthalten. Wir finden eine unterschiedliche SLR für glatte und unterstrukturierte Scheiben, was möglicherweise bedeutet, dass eine Mischung aus glatten und unterstrukturierten Scheiben in der beobachteten Probe vorhanden ist. Darüber hinaus schränken wir die Anfangsbedingungen für wichtige Parameter von protoplanetaren Scheiben ein.

Abstract

Our understanding of planet formation along with the study of protoplanetary disk evolution has been evolving rapidly the past decades. With the advent of new telescopes we get more detailed images than ever leading to constraints in planet formation but also to features as sub-structures that might be caused by planets. In two tangentially related studies, we first study the formation of giant planets via the emerging paradigm of pebble accretion and then we perform a large population study of protoplanetary disks to compare the observed properties to the simulated data. In our first study we find that when we use a realistic equation of state and radiative cooling in highly complex 3D-hydrodynamical simulations, the planetary core is able to open a large gap before reaching the required mass for runaway growth creating this way a transition disk. Therefore the planets at the location of Jupiter can grow up to a Super-Earth size. In the second study we explain the origin of the observed size-luminosity relation (SLR) between the 68% effective radius (r_{eff}) of disks with their continuum luminosity (L_{mm}) with simple models of gas and dust evolution. With the use of 10^5 simulations we show that a larger fraction of disks populate the SLR if planets are present compared to when the disks are smooth and they do not contain any sub-structures. We find a different SLR for smooth and sub-structured disks, potentially implying that a mixture of smooth and sub-structured disks are present in the observed sample. Moreover, we constrain the initial conditions on key properties of protoplanetary disks.

Chapter 1

Introduction

The word `planet` has its origins in ancient Greece and it was first used for star-like bodies that did not seem to follow the movement of the other objects in the sky, but they were "wandering" between the other stars as the seasons were changing instead. Later, with the approval of the heliocentric model, it became clear that the planets are objects orbiting the central star. Since then, people who wandered this planet and looked at the night sky have questioned, "are we alone in this Universe"? And while the definition of the word "Universe" has changed in the last century by discovering new galaxies, the question "are we alone", has become more intense. Our Universe is composed of some hundred billion galaxies, one of them being the Milky Way. "Our own galaxy" as we call it, even though we certainly do not hold any possession over it, as we do not hold have over "our planet". Galileo Galilei said, “The Milky Way is nothing else but a mass of innumerable stars planted together in clusters”, and he was not wrong. This galaxy is composed of gas and dust and several hundred million stars. In the outskirts of this galaxy, around a medium-sized star, there is a company of small worlds composed of different-sized planets, moons, meteorites, and comets. But the rapid development in astronomy in the last few decades helped to the discovery of more worlds similar to ours.

As of March 2023 besides the 8 planets of our own Solar system, we know more 5000 exoplanets[1] and in the next years the number of detections is set to exceed 10^4. From a statistical analysis of the microlensing data, Cassan et al. (2012) showed that every star in our galaxy is accompanied by at least one planet, while a similar result was obtained by Youdin (2011) from the analysis of the Kepler mission data.

A planet from the general point of view can be divided into different categories, from minor planets (Pluto, Ceres, etc) to giant planets (Jupiter, Saturn) or even rogue planets, therefore it became clear that the classical definition of a planet had to change and in 2006 the International Astronomical Union (IAU) redefined the term planet. Every body that

1. it is in orbit around the Sun,

2. has sufficient mass for its self-gravity to overcome rigid body forces so that it assumes hydrostatic equilibrium (nearly round shape),

---

[1] `www.exoplanets.org`

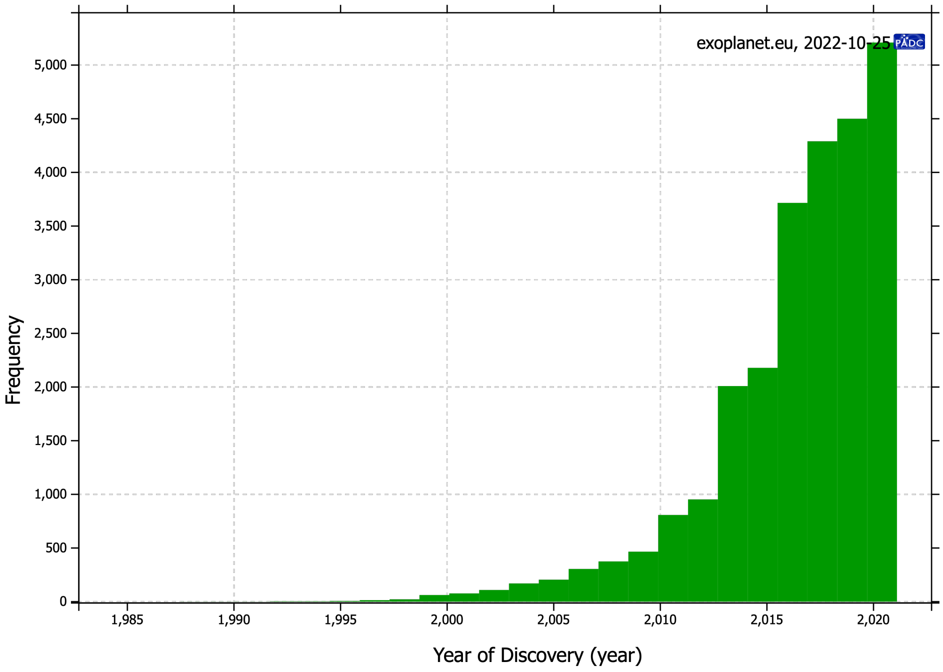

Figure 1.1: Cumulative number of exoplanets discovered and known as of 25.10.2022[2].

3. it has cleared the neighborhood around its orbit,

is considered a planet. Even though the first condition states that it should orbit the Sun it can be extended to any star in the universe. The last condition is the most important because it is based on our theoretical knowledge of how the planets form. A planet in order to clear its neighborhood has either to accrete all the minor bodies of the area close to it or drive them away. On the other hand, if all conditions apply except for the last one while also the object is not a satellite, the body is considered a dwarf planet.

We believe that at least half of the stars in the universe host a planet around them (Mayor et al. 2011; Fressin et al. 2013). The discovery of so many exoplanets expanded our understanding of the diversity of other planets and planetary systems compared to our Solar system. There have been discovered planets with a variety of masses, radii, and eccentricities. Compact planetary systems with many planets in the habitable zone of a dwarf planet as the TRAPPIST-1 system (Gillon et al. 2017), Super-Earths and giant planets that orbit their host star in a very close distance (hot Jupiters). In addition, the Atacama Large Millimeter/submillimeter Array (ALMA) allows us to observe in an angular resolution of $0.01''$, corresponding to few astronomical units (au), and while the first images of JWST already revolutionize the world as we know it, we expect more fascinating images for the planet formation community. This has opened up new horizons in the planet formation theory, leading to a rapid increase in studies that aim to explain the variety of the observed systems and correlations but it has also opened more questions to be answered.

Structure of this thesis

In chapter 1 we first introduce basic information about protoplanetary disks and their structure. In chapter 2, we review the current planet formation theories, focusing on pebble accretion, as it is part of the topic of this dissertation. We also explore the dust component in disks. In chapter 3 we introduce the concepts of radiative transfer and opacity and their application to our work. In chapter 4 we perform numerical simulations of protoplanetary disks focusing on the formation of giant planets by the pebble accretion scenario. In chapter 5 we perform a large population model of protoplanetary disks where we explore the theoretical findings with observed properties. In chapter 6 we summarize our work and propose future developments for this project and for the field of planet formation.

1.1 Observations of planetary systems

Planets form in protoplanetary disks, structures that are made of gas and dust and are observed around young stellar objects (YSOs). When a star is born, the gas around the object has angular momentum that does not allow it to collapse directly to the star, forming this way a rotating disk that survives as a quasi-equilibrium structure around the stellar core.

1.1.1 Disk classification

Initially, the stars are born in dense clumps of molecular clouds that are rotating slowly. When the mass of the cloud exceeds a certain mass known as the Jeans mass

$$M_{Jeans} = \left(\frac{5kT}{G\mu m_H}\right)^{3/2} \left(\frac{3}{4\pi\rho}\right)^{1/2} \tag{1.1}$$

the gravitational energy of the cloud will exceed the thermal energy, leading to lack of pressure support and consequently the collapse of the cloud under its own gravity. In the above equation, T is the temperature of the cloud, M is the mass, r the radius, k is the Boltzmann constant, G the gravitational constant, μ the gas mean molecular weight and $\mathrm{m_H}$ the hydrogen mass. Depending on the masses of the envelope and/or the development of a disk during the formation of the YSO, there is a empirical distinction between the pre-stellar and the proto-stellar phases (Maury et al. 2011). This distinction leads to four different classes (0 to III) (Lada 1987) visible in Figure 1.2. Class 0 and Class I are surrounded by an envelope that is accreting onto the proto-star. The Class II stage represents the most common stage of what we call a protoplanetary disk or classical T Tauri star where the YSO is still surrounded by gas that is accreting onto the star. This type of disk is the most relevant in our studies in this thesis. Class III, is the stage where the gas has almost dissipated leaving behind planetesimals and planets. The end product is a planetary system where there is no gas available and the newly formed star has entered the main sequence. This process should last around 10 Myr, which is the typical lifetime of a protoplanetary disk (see Section 1.2.1).

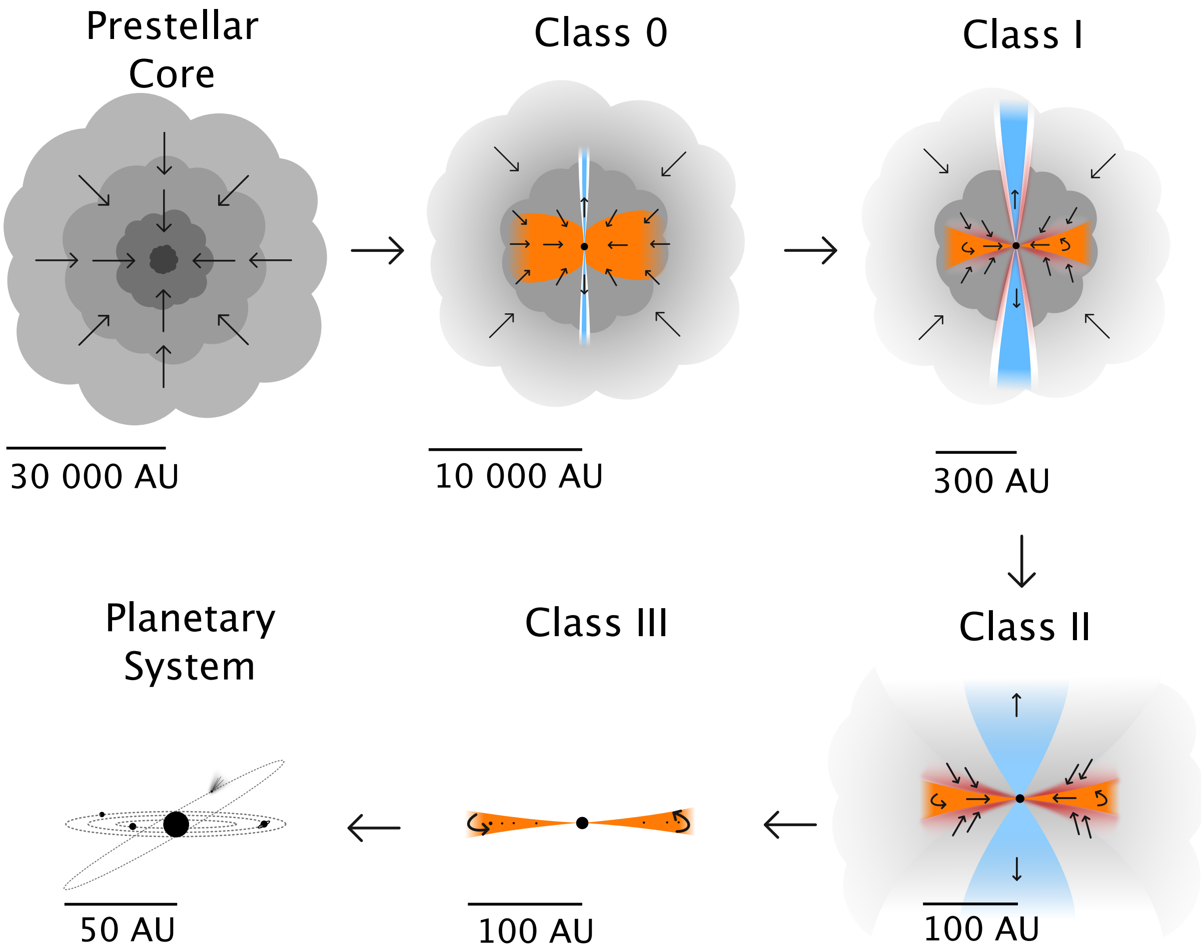

Figure 1.2: View of the different evolutionary stages of protoplanetary disks. Image taken from Persson, Magnus Vilhelm (2014).

The above classification is not arbitrary. It is based on the different Spectral Energy Distribution (SED) between these objects and pre-main sequence stars. YSOs show more emission in the infrared (IR) that is due to the presence of dust in the envelope or the disk. Therefore, the classification depends on the strength of the IR excess (Lada & Wilking 1984), with Class I having the strongest and Class III the least IR emission. Class 0 objects are optically thick, therefore their IR emission is undefined. The slope of the SED is defined as:

$$\alpha_{IR} = \frac{dlog(\nu F_\nu)}{dlog(\nu)} = \frac{dlog(\lambda F_\lambda)}{dlog(\lambda)} \tag{1.2}$$

where F is the flux, λ the wavelength and ν the frequency.

In Figure 1.3 we see the structure of the SED for the different classes in the left panel and for Class II specifically in the right panel. There are visible features in the spectrum related to

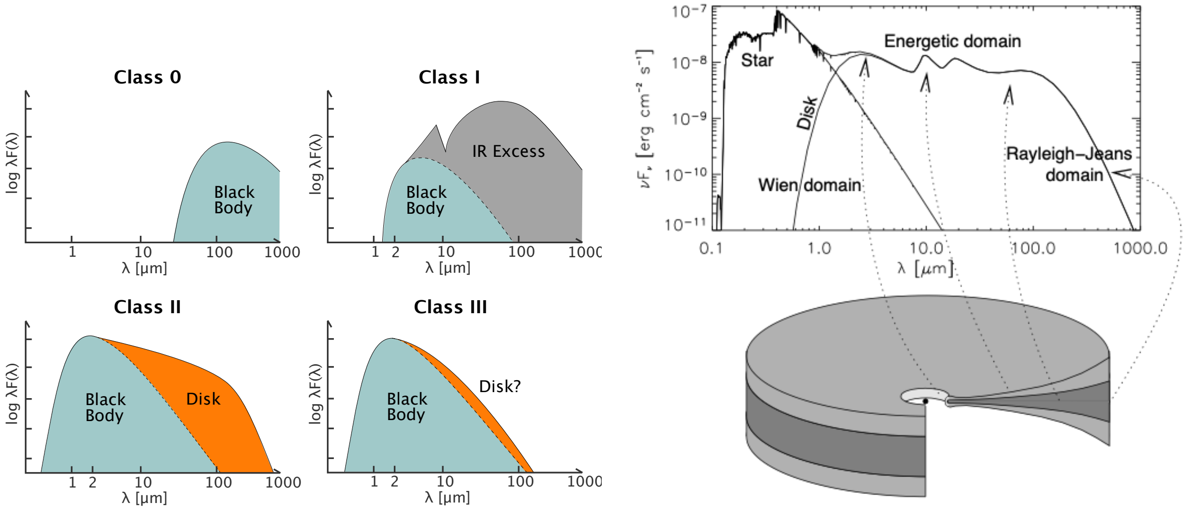

Figure 1.3: **Left panel**: Shape of the Spectral Energy Distribution (SED) of the different protostellar stages. Image taken from Persson, Magnus Vilhelm (2014).
Right panel: Build-up of the SED of a flaring protoplanetary disk and the origin of various components as taken from Dullemond et al. (2007): the near-infrared bump comes from the inner rim, the infrared dust features from the warm surface layer, and the underlying continuum from the deeper (cooler) disk regions. Typically the near- and mid-infrared emission comes from small radii, while the far-infrared comes from the outer disk regions. The (sub-)millimeter emission mostly comes from the midplane of the outer disk. Scattering is not included here.

certain regions in the disk. In the Class 0 phase, the cloud is emitting at long wavelengths as a blackbody at a very low temperature. On the other hand, class I to II show higher temperatures and a different shape than the blackbody. The reason is that the dust absorbs the stellar radiation and re-emits it at longer wavelengths, resulting in a stretched SED compared to the one expected by a blackbody. Since most of the dust is visible and available in Class I and Class II disks the SED stretches more to longer wavelengths in these two cases.

Observational properties

The observational properties of disks are key quantities to our understanding and the comparison with our theoretical models. The disk mass (gas and dust) is undoubtedly of great interest along with the size the temperature and the opacity. Knowing the above properties could help us to construct a much more robust theory in the evolution of disks.

1.1.2 Disk mass and density

Knowing the mass reservoir to form planets is tricky as the current resolution from our instruments does not allow for great spatial resolution, therefore measuring the dust surface density is not straight forward. The dust might represent only a fraction of the total disk mass ($\simeq 1\%$) relative to the gas, but it is the most crucial piece of the puzzle for planet formation as it shows the available reservoir for the formation of the solid cores. Therefore, our current understanding relies on theoretical models and strong assumptions when taking into account the measured continuum flux. The intensity of a plane-parallel layer with a homogeneous temperature can be calculated as

$$I_\nu = B_\nu(T_d)(1 - e^{-\tau_\nu}) \tag{1.3}$$

where τ is the optical depth (see chapter 3). In the optically thick limit ($\tau_\nu >> 1$) the dust temperature can be measured from the intensity as $I_\nu = B_{\nu(T_d)}$.

On the other hand, if the dust emission is optically thin ($\tau_\nu << 1$) the intensity is proportional to the absorption opacity κ_ν, the Planck function $B_\nu(T)$ at the dust temperature and the dust surface density Σ_d

$$I_\nu = B_\nu(T_d)\tau_\nu = \kappa_\nu \Sigma_d B_\nu(T_d) \tag{1.4}$$

By integrating the above equation it can be shown that Luminosity L_{mm} scales with the disk dust mass M_d as $L_{mm} \propto M_d$ (Hildebrand 1983; Beckwith et al. 1990). Our strong assumptions lie on the right hand side of Eq. 1.4 as if the opacity or the temperature is known then the surface density could be measured and vice versa. Therefore, we base our theoretical models in the premise that the emission is optically thin, in some standard opacity models (Birnstiel et al. 2018; Ricci et al. 2010, e.g.) and a temperature profile. Dust masses have been measured this way in various star-forming regions as for Taurus (Andrews et al. 2013), Lupus (Ansdell et al. 2016), Upper Scorpius (Barenfeld et al. 2016), Chameleon I (Pascucci et al. 2016), σ-Orionis, (Ansdell et al. 2018) and Perseus (Tychoniec et al. 2018). The results from these surveys are shown in Figure 1.4 where (Tychoniec et al. 2018) plotted the cumulative disk mass distribution for different star forming regions. It is shown that the mass decreases with time and the youngest star forming regions (Perseus, Lupus) contain the largest amount of solids (at least an order of magnitude more). The mass is lost due to radial drift or planet formation to the older regions (Upper Scorpius).

The disk gas mass is another property difficult to measure. Most of the disk mass resides in H_2 and using the measurements of dust mass as described above, and an assumed dust-to-gas ratio (usually 0.01, the gas mass can be calculated. Considering that the dust-to-gas ratio is not a well constrained value, the disk gas mass can be easily miscalculated. Another way to estimate the gas mass is via HD measurements, as a direct tracer of H_2, as well as the emission from the CO rotational transitions of one of the optically thin isotopologues via a CO-toH_2 ratio Schwarz et al. (e.g. 2016); Booth et al. (e.g. 2019). Typically, the CO abundance is assumed to be in the order of 10^{-4} based on interstellar estimates.

As the dust-to-gas ratio, the $CO - to - H_2$ ratio is also an uncertain quantity, due to evidence that CO is depleted due to freeze out, isotope-selective photo-dissociation and conversion to more complex chemical species Miotello et al. (e.g. 2016); Schwarz et al. (e.g. 2016). This depletion is believed to explain why the HD measurements for TW Hya is higher by 2 orders of magnitude than the CO estimate Bergin et al. (2013); Schwarz et al. (2016); Kama et al. (2020). Another approach is to measure the disk gas mass is to use theoretical models using the so called dust-line, which is the maximum radial emission of at a certain wavelength. Powell et al. (2017, 2018) linked this to the local surface of the disk and consequently to the dust-to-gas ratio (more details in chapter 6). A study from Franceschi et al. (2022) that used the model developed in this thesis

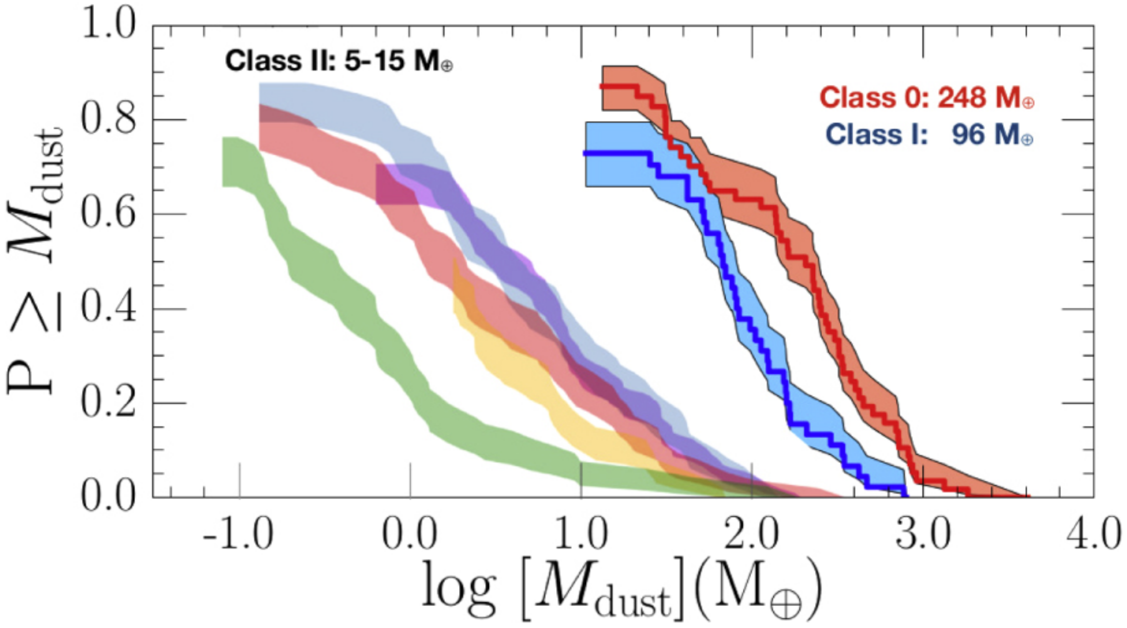

Figure 15. from The VLA Nascent Disk and Multiplicity Survey of Perseus Protostars (VANDAM). IV. Free–Free Emission from Protostars: Links to Infrared Properties, Outflow Tracers, and Protostellar Disk Masses
null 2018 APJS 238 19 doi:10.3847/1538-4365/aaceae
http://dx.doi.org/10.3847/1538-4365/aaceae

Figure 1.4: Cumulative disk mass distributions for different star forming regions as presented in (Tychoniec et al. 2018).

(see chapter 5) investigated if the dust-line is a good mass disk mass estimator. They conclude that it is a good approach to define the disk mass but the exact relation between the dust line location and disk mass depends on the disk structure.

Regardless of the different approaches, the total disk mass remains a fundamental, yet difficult to define quantity. In every method, multiple assumptions have to be made the can possibly lead to misleading results.

The density of protoplanetary disks can be derived by Eq. 1.4 if a fixed dust opacity and a temperature profile is assumed. New studies show that disks are not as massive as the Minimum Mass Solar Nebula (MMSN) (Tazaki et al. 2017), but the new high resolution images show significant sub-structures (Andrews et al. 2018b). These structures can optically thick and consequently they can hide mass that is not accessible to observations.

1.1.3 Protoplanetary disk sizes

The size of protoplanetary disks is not an easily defined measure. Since there is no clear edge at the end of the disk, it is usually fitted with models of viscous evolution (Manara et al. 2019).

A well known approach is to assign an effective radius r_{eff} as a radius that encloses a specific fraction of the luminosity (Tripathi et al. 2017; Andrews et al. 2018a).

Since a disk is consisted of gas and dust the size of the two might differ. A general trend in disk sizes is that Class II disks are larger in gas than in dust (Sanchis et al. 2021). These results have been observed in the infrared where the scattered light is traced. For the dusty disks, according to the most recent surveys (Pascucci et al. 2016; Ansdell et al. 2016) the disk sizes vary depending on their structure. Smooth disks that do not contain any substructure tend to be smaller and their size can be anywhere from 20 au to 40 au (Long et al. 2019). On the other hand, disks that have sub-structures can extend their radius up to 200 au. Sanchis et al. (2021) found from ALMA surveys that Class II disks that extend beyond 100 au are rare and they cover only a small fraction ($\simeq 15\%$) of the population. The same result applies to young Class 0 and I disks (Tobin et al. 2020). Zormpas et al. (2022) in chapter 5 showed that when sub-structures are included the dust size tends to get larger than 80 au.

From the measured effective radii, a tight correlation between the luminosity and the effective radius has been shown (Tripathi et al. 2017; Andrews et al. 2018a) that scales as $L_{\text{mm}} \propto r_{\text{eff}}^2$. This relation has been explored by Zormpas et al. (2022) and is a major topic of this thesis in chapter 5. The origin of this relation can be explained by the evolution of dust particles in the drift limit (Rosotti et al. 2019a; Zormpas et al. 2022) but there might be other reasons for its existence, namely high optical depths (Andrews et al. 2018a; Zhu et al. 2019). On the other hand, the gas radius is easier to measure as there are less assumptions to be made. Measurements are usually made by tracing the line emission of CO. According to Ansdell et al. (2018) the sizes extent up to $R_{\text{CO}} \simeq 500$ au.

1.1.4 Temperature

The knowledge of the dust temperature in the disk is another property that is not easily measured. It is a fundamental property that controls many key aspects of the disk as the dust dynamics, the dust continuum intensity and the chemical composition. As a first approximation, the disk is usually considered as passive, meaning that heating is originated from the star. Most part of the disk is heated by the dust. The solids in the disk are heated by the star and while they scatter the energy they heat the gas at the mid-plane (Chiang & Goldreich 1997; D'Alessio et al. 1998) leading to an increasing vertical gradient while it is also decreasing with the distance from the host (Kenyon & Hartmann 1987). The reason that the temperature is defined by the dust is that the gas opacity is small in the continuum therefore, a gas-only disk would be essentially transparent to the star radiation. On the other hand, the dust is mainly optically thick in optical wavelength.

The temperature is most commonly parametrized by the sound speed as $c_s \propto T^{0.5}$ and the pressure scale height

$$H_p = \frac{c_s}{\Omega_k} \tag{1.5}$$

where Ω_k is the Keplerian angular velocity. To calculate properly the dust temperature, requires radiative transfer calculations but usually a power-law as the following is assigned.

$$T(r) = 100 \left(\frac{r}{1au}\right)^{-0.5} K \tag{1.6}$$

Again, to constrain the temperature as mentioned in Section 1.1.2, an assumption of the opacity and the surface density has to be made and later a model of the Spectral Energy Distribution (SED) should be constructed. Therefore, a comparison with the observed SEDs is possible and the process continues until a similar SED is reproduced even though there are large uncertainties (Thamm et al. 1994; Heese et al. 2017). If the disk is in the optically thick limit, spatially resolved images allow for the direct measurement of the dust temperature which is identical to the brightness temperature.

There are different sources that can alter the temperature in the disk apart from the host star. External irradiation (Natta 1993; D'Alessio et al. 1997), viscous dissipation (D'Alessio et al. 1998), spiral schocks (Rafikov 2016) are some of them.

The gas temperature is more easily measured as there are direct methods from the gas emission line fluxed and the radial emission profiles or from molecular emission maps that can trace different ice lines at specific disk locations but it will not be o topic of this analysis.

1.1.5 Sub-structures

In the pre-ALMA years the observing spatial resolution was in the order or $15 - 20 \geq$ au (Andrews 2020), therefore there was often the case where details were not visible. In the last years ALMA revealed images with unprecedented resolution of the dust continuum (e.g. Andrews et al. (2018b)) and many disks appeared to have fine-scale features or structures as rings/cavities, gaps, vortices, arcs and spirals (see Figure 1.5).

- A ring is defined as a narrow ring that surrounds a clear and deep cavity (Andrews et al. 2011). The above morphology usually defines a transition disk (Espaillat et al. 2014). These disks are great examples of particles traps at maximum pressure (Pinilla et al. 2012b, 2018) and we think they can act as planet formation locations.

- Gaps are defines as concentric, axisymmetric pattern of alternating rings and gaps. Prime examples are visible in Figure 1.5.

- Arcs are non-axisymmetric structures that can appear to exterior to rings (Marino et al. 2015; van der Marel et al. 2016; Kraus et al. 2017; Boehler et al. 2018) or in a gap (Isella et al. 2018; Pérez et al. 2018) but they appear to be rare (Pérez et al. 2016a).

- Examples of spirals are rare in mm-continuum but they exist (Pérez et al. 2016a; Huang et al. 2018a). They are more often observed in scattered light (Muto et al. 2012; Grady et al. 2013; Akiyama et al. 2016).

Before the DSHARP survey the most well known example was HL Tau. A protoplanetary disk in the Taurus region where clear rings are present (ALMA Partnership et al. 2015). Later, more studies revealed sub-structures (Andrews et al. 2016, e.g.) and since then disk-substructures seem to be ubiquitous. After these discoveries, there is a shift towards studies that model substructures in disk evolution models. The reason of the formation of these structures is usually assumed to be due to planet formation (e.g. Dong et al. 2015; Zhang et al. 2015; Teague et al. 2018). They

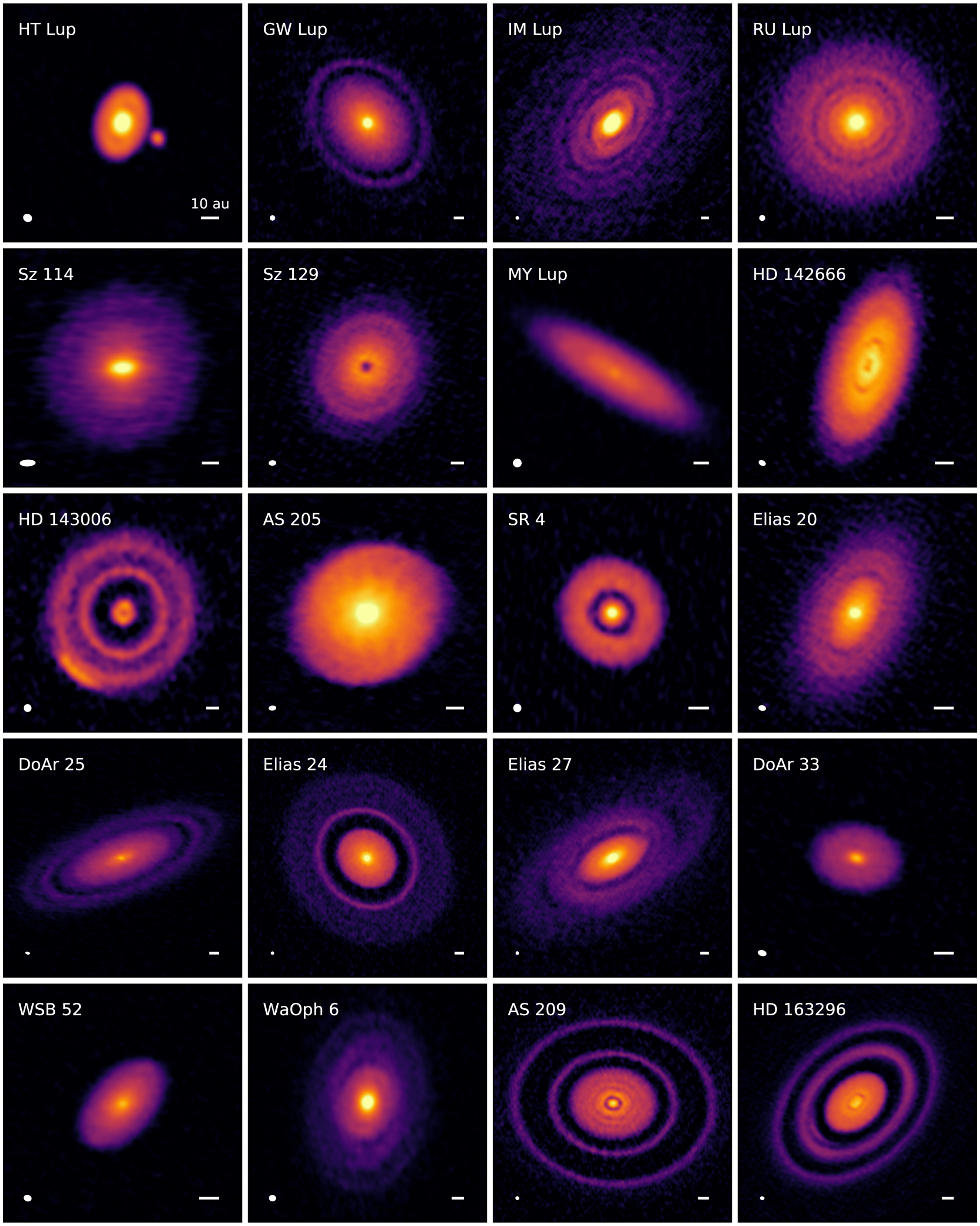

Figure 1.5: A gallery of 240 GHz 1.25 mm) continuum emission images for the disks in the DSHARP sample as adopted from Andrews et al. (2018b). The beam sizes are shown in the lower left and 10 au scale-bars are shown in the lower right corners of each panel, respectively.

can be found in any location in the disk and there is no relation between the location and the host properties (Pinilla et al. 2018; Long et al. 2018; Huang et al. 2018a; van der Marel et al. 2019). It is reasonable that substructures in the outer regions of the disks are larger as the disk scale height (H_p) increases with radius.

Sub-structures can also be observed by kinematical studies. Teague et al. (2018) measured the velocity perturbations in the disk HD163296 and showed that the rings could be a result of the presence of three Jupiter mass planets. Moreover, Pinte et al. (2018) used the kinks in the channel mass to find similar results, leading to the direction that these rings are most probably formed by planets.

In disk evolution models, the density (and consequently the pressure) is decreasing monotonically as a function of the radius and the disks are considered as smooth. Therefore the pressure gradient is negative and the gas should orbit at sub-keplerian velocity while drifting particles move towards the star. When a sub-structure is present the pressure gradient changes briefly to positive. With $dP/dr > 0$ the gas changes to super-Keplerian motion and particles move outwards. At the location of the maximum, the pressure gradient is zero and that location particles do not drift, therefore acting as a trap. If turbulence is not strong enough to replenishing the gap, a gap opens. Therefore, the surface density and the pressure is increasing with radius outside the orbit of a giant planet, until it reaches a maximum when then decreases again.

Another reason that substructures is believed to be the birthplaces of planet formation is due to the ability of traps to solve the well known drift problem (Pinilla et al. 2012b). In smooth disks the radial drift is too efficient, leading to fast depletion of the disk material and consequently limiting the time that a planet can form. When substructures are present within the disk the drift timescale is getting longer. Moreover, the dust-to-gas ratio in these traps can increase above unity, allowing the streaming instability scenario to take place and consequently the rapid creation of planetesimals (Youdin & Goodman 2005; Johansen et al. 2007).

1.1.6 Observed relations

The abundance of available data from ALMA have made it possible to construct relations between different properties of protoplanetary disks. These relations can give us valuable insights to the underlying properties of protoplanetary disks as we can have a birds eye view on a large sample of disks instead of studying disks individually.

A very famous relation which was the initial trigger dor this study is the Size-Luminosity relation (SLR) from Tripathi et al. (2017) which is studied extensively in this dissertation in chapter 5, and as the name suggests is compares the observed Luminosity of the disks to their size. Hendler et al. (2020) found that the same SLR is found in other star forming regions and it is getting flatter with the age of the region. In Upper Scorpius (10 Myr) the flattest relation is found (Figure 1.6, left panel). In our study, we found that the relation becomes flatter when sub-structures are included.

Besides the SLR there have been numerous more. For an example the relation between the host stellar mass and the disk dust mass. Pascucci et al. (2016) found that $M_{\rm dust} \propto M_\star^{1.3-1.9}$, which is a steeper than linear relation and it steepens with the age of the star forming region similar to the Size-Luminosity relation. A study from Pinilla et al. (2020) showed that a flatter relation

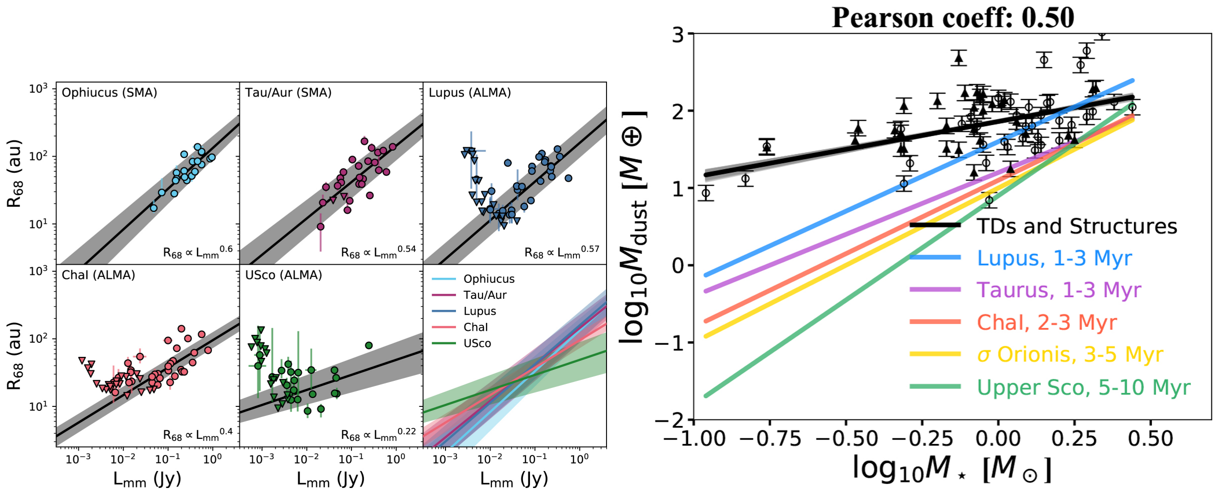

Figure 1.6: Left panel: $\log R_{\rm eff} - \log L_{\rm mm}$ relation taken from Hendler et al. (2020). The first 5 panels (left to right; top to bottom; ordered by region age) show the model results of each region as circles (resolved) and triangles (upper-limits). The best fit from MCMC linear regression is plotted as a black line, and surrounded by 68% confidence intervals in grey. The last panel replots the best fits of each region (and the corresponding 68% confidence intervals) so that they can be directly compared.
Right panel: Dust disk-to-star mass ratio from Pinilla et al. (2020) showing their data for transition disks in comparison to the observations

can be reproduced if the disks have large cavities as it is visible in Figure 1.6, right panel. This figure points to the fact that when disks contain large sub-structures they can remain massive independently of the host mass.

Taking into account different properties, such as the gas accretion rate from other than ALMA surveys (e.g. VLT/X-Shooter), there has been a relation between the disk dust mass and the gas accretion rate from Manara et al. (2016) with a ratio that is roughly consistent with the expected viscous timescale when assuming an interstellar medium gas-to-dust ratio. This study confirmed that mass accretion rates are related to the properties of the outer disk.

All planetary systems are produced by common physical mechanisms but they are different to one another. Not all planetary systems are the same, as already explained in chapter 1, disks come with different sizes, masses and general physical properties. In this chapter we will describe the key processes of planet formation and we will show how they can be combined to produce different planetary systems.

1.2 Observational constraints

All planetary systems are produced by common physical mechanisms but they are different from one another. Not all planetary systems are the same, as disks come with different sizes, masses and general physical properties. Consequently, this leads to planets with different sizes, radii, orbital periods and composition.

1.2.1 Disk lifetimes

Protoplanetary disks are born in young clusters which are traced by the hot dust that they contain (Haisch et al. 2001), but they seem to appear rarely in old clusters. By comparing a large number of young clusters of different ages between 0.3 and 30 Myr, it has been shown that the typical lifetime of a disk before it dissipates is a few Myr ($\propto$ 6 Myr) (Haisch et al. 2001), independently of the stellar mass. Afterward, this value changed according to different approaches but Mamajek (2009) parametrized the disk fraction for low mass stars within a cluster as an exponential expression and found that the lifetime of is the order of 2.5 Myr. This is shown in Figure 1.7, where we observe an exponential decay in the presence of a gaseous disk with respect to the age of the cluster. It is worth mentioning, that multiple observational biases might affect the outcome of this figure as the selections of stars that are cluster members can affect the interpreted disk dissipation timescale (Pfalzner et al. 2014).

In the later years, multi-wavelength studies (Ribas et al. 2014) found that disk lifetime increases when they are observed in longer wavelength and later they constrained the lifetime to 2.5 - 5 Myr. The wide approach is still that disks leave for a timespan of $\leq$ 10 Myr.

1.2.2 Observational constraints on Super-Earths and giant planets

The constraints on the characteristics of planets come mostly from Solar System measurements (e.g. measuring properties of meteorites), observations of other planetary systems and their exoplanets as well as from laboratory experiments.

Demographics

During the last decades a diversity of planets has been discovered even though observational biases are limiting our ability to observe small planets. It is worth mentioning that if our Sun was to be observed with the current technology, only Jupiter would be able to be observed (Morbidelli & Raymond 2016). Furthermore our Solar System does not contain any low-mass planet very close to the Sun (Mulders et al. 2018). In this thesis we focus on giant planets (especially around Sun-type stars) and super-Earths.

Giant planets

Due to data from different observational techniques such as radial velocity, direct imaging and microlensing, it has been found that giant planets are thought to exist in $\propto$ 10% of Sun-like stars (Cumming et al. 2008; Mayor et al. 2011). Very few of them are observed to be close-in hot Jupiters with a short orbital period in the order of hours or days. Even fewer appear to be warm Jupiters with radii (0.5-1 au, but the majority of the population occurs from 1 to several astronomical units, while it decreases again to the outskirts of the system.

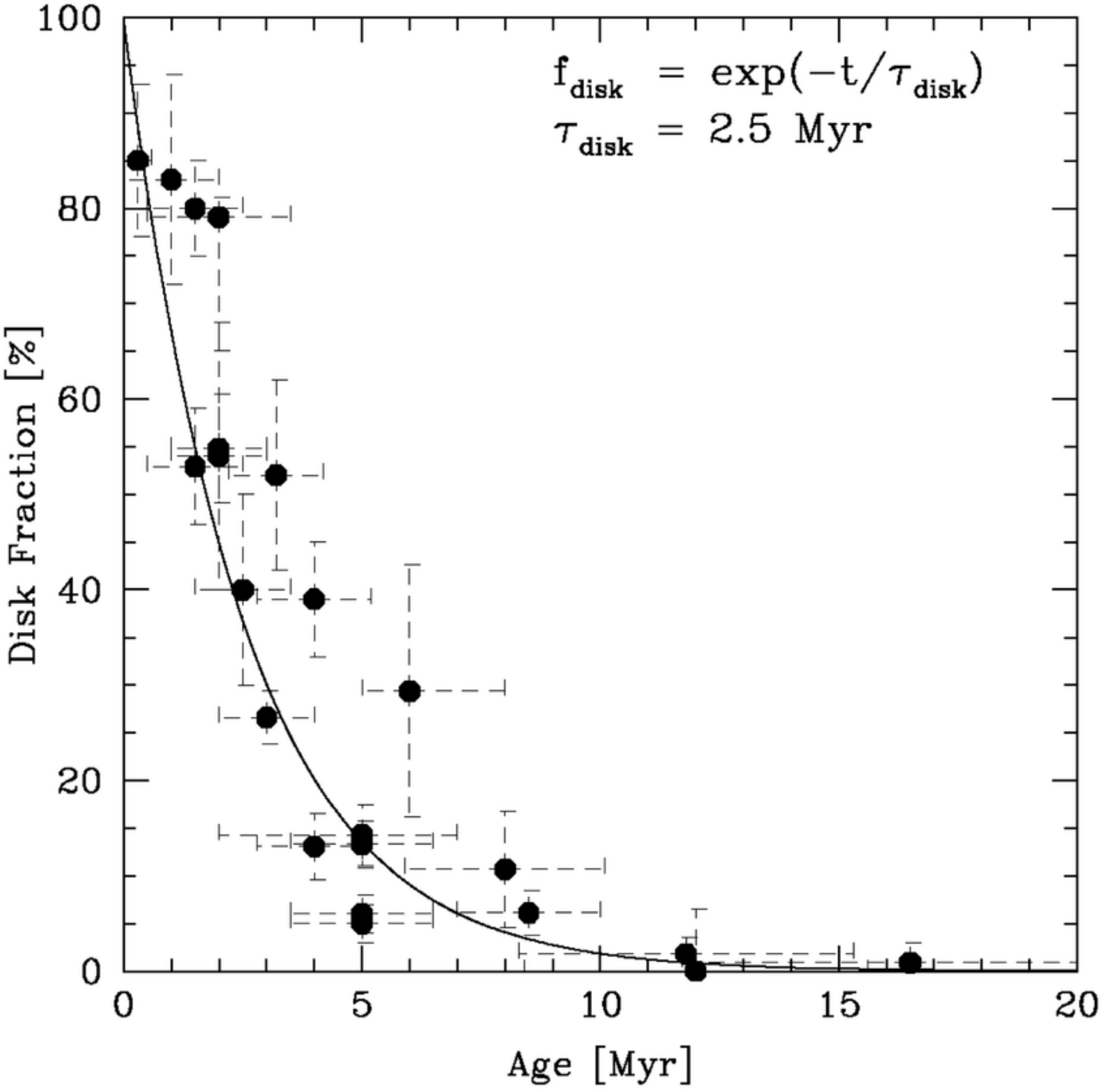

Figure 1.7: The age of a stellar sample against the fraction of stars with primordial disks. This spectroscopic survey of optically thick disks indicates an exponential decay with characteristic time. Plot adapted by Mamajek (2009)

Super-Earths

In the last years a shocking discovery was the existence of the so called Super-Earths at a high rate in exoplanetary systems. Roughly 30-50% of the observed systems around main sequence starts contain a planet with a mass between Earth and Neptune (below $10\,\mathrm{M}_{\mathrm{oplus}}$) and with a period shorter than 100 days (Mayor et al. 2011; Howard et al. 2012; Dong & Zhu 2013). In this group of planets, the ones with lower mass tend to have higher densities and vice versa. The lower mass planets are typically called Super-Earths and the higher mass planets are called mini-Neptunes.

Chapter 2

Planet formation

In this chapter we will describe the key processes of planet formation, starting from the underlying principles of dust evolution all the way to planet formation theories and we will show how they can be combined to produce different planets.

2.1 Dust evolution

Dust, even though it occupies only 1% of the mass of the disk, it is the material out of which planets and other smaller bodies form. It also defines the opacity and the temperature structure of the disk. Therefore, it is important to understand how dust evolves as it is a key component in protoplanetary disk. Understanding dust evolution requires the study of the protoplanetary disks structure and evolution, and the physics of dust collisions. While the massive distances from protoplanetary disks allow only for the exploration by observations of YSOs combined with theoretical models, the latter can luckily be studied in laboratory experiments that have been summarized by (Blum 2018a).

Figure 2.1 shows a protoplanetary disk where the physical properties are illustrated (Miotello et al. 2022). Some of these properties, relevant to our studies are analyzed in the following sections. On the left side, the dust temperature and the gas density are shown. Particles are represented as black dots and their size varies by the symbol. On the right there the regions probed by various wavelengths are illustrated. For example, scattered light is used to probe the surface of the disk while IR is for the mid-plane.

Measurements of interstellar extinction (Mathis et al. 1977) have shown that the interstellar dust grains have a size that ranges from $0.1 - 1\mu$m with a size distribution $\mathrm{n(a)} \propto \mathrm{a}^{-3.5}$, where $\mathrm{n(a)}$ denotes the number of particles with a given size a. New studies show that the exponent changes to 2.5 while a disk is drift dominated (Birnstiel et al. 2012; Zormpas et al. 2022). Through a series of collisions, these dust particles stick with each other due to adhesive forces until fully grown planets are formed. The initial growth of these particles can reach up to objects of km-size in diameter but the procedure is not smooth as many barriers can halt the process. The radial drift and fragmentation among others are some of the barriers that will be explored later as they are a core part of this thesis.

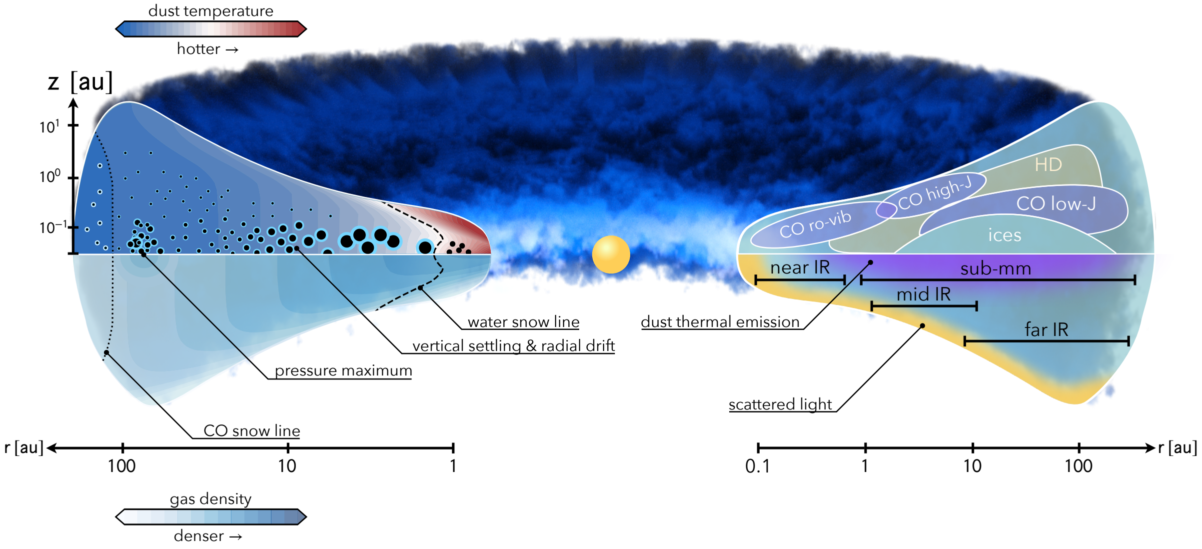

Figure 2.1: **Left**: Illustration of the dust temperature and gas density structure. A distribution of dust particles is shown by the black circles, whose size variation is represented by the symbol size. Bare grains are present within the water snow line (dashed curve), H2O-coated grains are contoured in blue, and CO-coated grains, outside the CO snow-line (dotted curve), are contoured in white. **Right**: A simplified representation of the emission regions of the main simple molecules is shown in the top panel, while the main dust thermal and scattered light emission regions are highlighted in purple and yellow in the bottom panel. Figure obtained by Miotello et al. (2022)

A useful quantity in dust evolution is the Stokes number. It is the dimensionless ratio of the stopping to the dynamical time scale

$$St = t_{stop}\Omega \tag{2.1}$$

where Ω is the local Keplerian frequency. The use of the Stokes number is visible between two particles that have different compositions, structures or masses but behave aerodynamically the same if they have identical Stokes numbers. The Stokes number is linearly dependent on the particle size if we assume a vertically isothermal gas disk with $H_g = c_s\Omega$ and gas surface density Σ_g. Then, the Stokes number at the mid-plane becomes

$$St = \frac{\alpha\rho_s}{\Sigma}\frac{\pi}{2} \tag{2.2}$$

where ρ_s is the internal density of the particles. In general, when the Stokes number decreases, the coupling to the gas becomes tighter and vice versa. A particle with Stokes number St << 1 is considered tightly coupled to the gas as it will adapt to the gas velocity in a shorter timescale than the orbital, while a large particle with St >> 1 is considered decoupled from the gas as its velocity will be altered significantly by the drag forces in several orbits.

2.1.1 Radial drift

Early in the 1970s Whipple (1972) and later Weidenschilling (1977), found that the dust particles in a disk migrate towards the star, a process called radial drift. The reason for the radial drift is that the particles are embedded in the gaseous disk and they feel the drag force from the gas. Therefore this drag removes orbital energy from the dust and consequently forces the dust particles to move with a different radial velocity than the gas, while the effect from the dust to the gas is negligible. The reason that the particles move inwards is not arbitrary. Generally, a disk is assumed to be smooth and that the pressure P(r) decreases monotonically. Therefore the gradient of the pressure dP/dr is always negative and the gas orbits at sub-Keplerian velocity. The radial dust drift speed can be described by

$$\upsilon_r = \frac{1}{St + St^{-1}} \eta V_k \tag{2.3}$$

V_k the Keplerian velocity and η shows how much slower the gas is orbiting than the Keplerian speed.

$$\eta = -\frac{1}{2} \left(\frac{H_p}{r}^2 \right) \frac{\partial lnP}{\partial lnr} \tag{2.4}$$

where H_p is the pressure scale height. When the particles grow due to collisions they reach a size where they are disconnected from the pressure support of the gas. Therefore, particles tend to move towards maximum pressure and since a disk is hotter and denser closer to the star, they move inwards. Generally, small particles with Stokes number St < 1 move slower as they are coupled to the gas and large particles move faster. Larger particles with St >> 1 tend to decouple from the gas and their drift velocity tends to zero, therefore equals the Keplerian velocity. Generally, radial drift is most efficient for pebble-sized particles (mm/cm sizes) at distances of tens of au.

The radial drift does not come without its drawbacks. In planet formation theory the key problem is that the radial drift is too efficient (Takeuchi & Lin 2002) and the dust is removed faster than it is needed to form planets. In simple terms, the drift timescale is shorter than the collision timescale, leaving no dust available to form large objects.

2.1.2 Dust Growth

Particles need to grow several order of magnitude to create a planet from a size of 1 μm to 10^6m (roughly the radius of Earth) or more. Not all particles can collide with each other as different velocities can alter the outcome. Moreover, two particles can only collide if they are in the vicinity of each other and how often this does happen can be calculated from their mean free path

$$l = \frac{1}{n_j \sigma_{ij}} \tag{2.5}$$

where n_j is the number density of particles j and $\sigma_{ij} = \pi(\alpha_i + \alpha_j)$ is the cross section of particles i and j, if the particles are spherical and have radii α_i and α_j respectively. Therefore, particles with a relative velocity $\Delta\upsilon_{\mathrm{ij}}$ will collide in a collision time scale

$$\tau = \frac{l}{\Delta\upsilon_{ij}}. \tag{2.6}$$

In reality, particles cannot always collide. Depending on many factors such as the impact velocity and composition, there are different collision outcomes. Two particles can stick, fragment, bounce or erode. Figure 2.2 show how a collision model works for two particles of different sizes. A lot of experimental studies have been performed on this topic (e.g. Blum & Wurm 2008). Particles can collide due to different kinds of impact velocities. Small particles ($\sim \mu$m) collide due to the Brownian motion, but when they start to grow, velocities due to turbulence become important (Birnstiel et al. 2011). The impact velocity of two equal size particles due to turbulence is:

$$\Delta\upsilon_{turb} \simeq \sqrt{\frac{3\alpha}{St + St^{-1}}} c_s \tag{2.7}$$

where α is the turbulence parameter (see Section 2.2.7) and c_s is the isothermal sound speed. This collision velocity increases up to St = 1 and then decreases. When particles become even larger (up to St $\simeq$ 1), then radial drift (see Section 2.1.1) velocities dominate (Testi et al. 2014). For particles with (St >> 1), azimuthal relative velocities dominate.

But depending on the composition a particle can reach a certain size before they fragment from the impact (Brauer et al. 2008; Birnstiel et al. 2009). We can define then a fragmentation size limit is

$$\alpha_{frag} = \frac{1}{3}\frac{v_{frag}^2}{\alpha c_s^2}. \tag{2.8}$$

v_{frag} is the fragmentation velocity and it varies according to the composition and the material properties of the particle. As an example, for standard silicate grains, the fragmentation velocity is $v_{\mathrm{frag}} = 1$ m/s (Blum & Wurm 2000; Poppe et al. 2000; Güttler et al. 2010a).

Besides the fragmentation limit, there is another barrier that halts the growth of particles called the drift size limit (Birnstiel et al. 2012). It is defined as the point where the local growth time scale ($t_{\mathrm{growth}} = 1/\epsilon\Omega_{\mathrm{K}}$) equals the local drift time scale (Klahr & Bodenheimer 2006)

$$\alpha_{drift} = \frac{\upsilon_K^2}{c_s^2}\epsilon\gamma^{-1}, \tag{2.9}$$

where $\gamma = |\mathrm{dlnP/dlnr}|$ and ϵ is the dust to gas ratio. What this size practically means is that particles below this curve in a particle size-radius diagram, grow faster than they drift while those above it drift faster than they grow.

In general Birnstiel et al. (2012) found that fragmentation dominates the inner regions of the disk (a few au) while the outer regions are dominated by drift because the growth timescale increases with radius. In chapter 5 for example, since we are focusing mostly on features in the outer part of the disk, most of the simulated disks are drift limited.

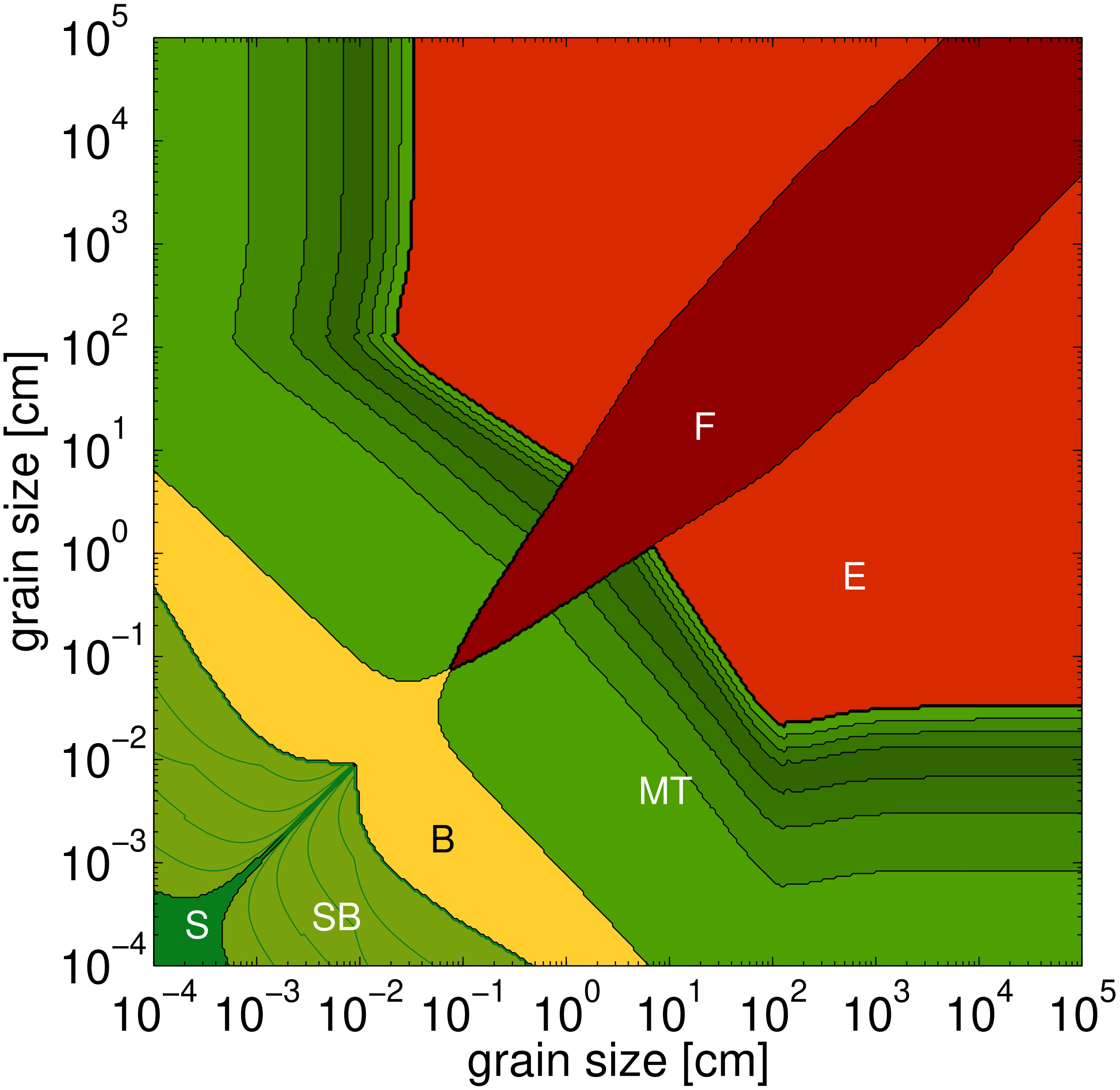

Figure 2.2: Collision outcomes in the parameter space for silicate grains as demonstrated in Windmark et al. (2012), at 1 au for a MMSN disk, based on the laboratory experiments. The green regions show growth of the larger collision partner due to mass transfer and sticking. The red regions show mass loss due to fragmentation and erosion, and the orange ones show bouncing collisions that do not affect the mass.

2.2 Planet formation theories

The fundamental question of how planets form is still a puzzle in modern astrophysics, but various pieces have been put into place throughout the last decades. Historically, the first records on this question were made by the Greek philosophers. In the 5th century BCE, Leukippos suggested that other Worlds form when bodies sink into the empty space and connect to each other. This sentence is not far from what is happening in large scale in reality. Around 300 years ago, Immanuel Kant (1755) and Pierre-Simon de Laplace (1796) suggested the nebular hypothesis, but the first physical model of planet formation was presented in 1969 (Safronov 1969). From the first exoplanet around around a solar-type star that was discovered in 1995 (Mayor & Queloz 1995), that was also awarded with a Nobel Prize in Physics in 2019, a lot of progress has been made towards a complete model of planet formation, but we are still far from an accepted theory as with the new observations more constraints are put into place.

Planets form in protoplanetary disks, structures that are made of gas and dust and are observed around young stellar objects (YSOs). When a star is born, the gas around the object has too much angular momentum to collapse directly to the star, forming this way a rotating disk around the stellar core (Terebey et al. 1984). Therefore the formation of disks is a consequence of angular momentum conservation. The typical lifetime of a protoplanetary disk is in the order of 10 Myr, a short timescale for astronomical objects, but enough to influence the system for billion of years. Within this time-frame planets need to form, therefore different theories have been established, trying to explain how could this be possible is such a short window. Since disks are the birthplaces of planets, their different characteristics such as mass, size, composition, etc, are crucial for their evolution and consequently for the characteristics of the forming planets. On both chapter 4 and chapter 5, we focus on giant planets, therefore in the next sections we will explore how massive planets can form in protoplanetary disks.

2.2.1 Core accretion

Giant planets (e.g. Jupiter) are objects that contain a large volume of hydrogen and helium and possibly a solid core. They are rare at small radial distances but they are most commonly found between $1-10$au and become increasingly rare at $10-100$au. The process to collect this amount of gas has been explored thoroughly by multiple theories over the years.

The current paradigm suggests that planet formation is a multi-part process, starting from micron-sized dust particles reaching all the way to gas giants, a process that spans over 12 orders of magnitude in size. This process can be summarized in Figure 2.4 from Drazkowska et al. (2022), where the different stages are named.

The standard model for planet formation is the so-called *core accretion* model (Pollack et al. 1996) in which giant planets are formed in the stages that are shown in figure (Figure 2.3)[1]. In this scenario, sub-μm dust grains grow due to collisions to $>$ km sized bodies, a process called bottom-up. These bodies, which are too small to be called planets but large enough to be gravitationally bound, are called planetesimals in the planet formation theory.

The general idea is that a planetary core is built from heavy elements and its growth is due to a combination of collisions of planetesimals Pollack et al. (1996), pebbles (Lambrechts & Johansen 2012) or both (Alibert et al. 2018). Planetesimals larger than 10 km in diameter collide under the influence of the gravitational force with the newly formed planetary core. For objects

---

[1] Available in Armitage (2010)

of this size, the effect of gas drag is negligible and the accretion is ruled only by gravitational dynamics, which leads to the gravitational focusing effect (Safronov 1969; Wetherill & Stewart 1989; Lissauer & Stewart 1993; Kokubo & Ida 1996). The solid core grows until it is so massive that it can retain a gaseous atmosphere that is accreted by its surroundings. The requirement for a planet to hold an atmosphere is that the escape velocity should be larger than the sound speed $v_{esc} > c_S$. When a critical mass is reached ($10M_\oplus$) and the gravity is high enough then runaway gas accretion is triggered (Perri & Cameron 1974; Mizuno 1980)) and the formation of a gaseous planet is possible. The remaining gas is accreted onto the planet up to a certain mass level. The accretion stops either due to the available reservoir being depleted or because the planet opens a gap to its surrounding and is isolated from the disk. Eventually, the planet cools down and is experiencing a quasi-hydrostatic (Kelvin-Helmholtz) contra

The core accretion theory does not stand without its limitations. Observations in the lifetimes of protoplanetary disks show that the gas dissipation holds approximately for at most 6 million years (Bell et al. 2013). As Lambrechts & Johansen (2012) mention, the core accretion by km-sized planetesimals fails to meet the timescale constraint from a theoretical point of view, especially for planets at tens or hundreds AU from the central star, where core growth timescales increase rapidly.

This is much shorter than the time needed to grow cores to completion in numerical simulations Levison et al. (2010) of disks with solid surface densities comparable to the minimum mass solar nebula (MMSN) Hayashi (1981). This timescale has some strong constraints on how quickly gas and ice giants with a solid core of approximately $10M_\oplus$, which is responsible for the gas attraction, can form. The solid materials accreting onto the forming planetary core can have different origins based on the local size distribution and stopping time of the solid disk. Moreover, the gaseous envelope does not grow with the same rate on a timescale of Myr (Lambrechts et al. 2014), due to the continued heating by accretion or remnant planetesimals, even after clearing most of its feeding zone (Pollack et al. 1996; Ikoma et al. 2000).

2.2.2 Gravitational Instability

The rival awe of the core accretion model is the top-down process, called gravitational instability (GI) (Boss 1997; Mayer et al. 2002) and it has its origins many years before the core accretion model, (Kuiper 1951; Cameron 1978). The formation route in this scenario is similar to the star formation process. When a protoplanetary disk has a high initial gas density, it is fragmented into clumps. The criteria for a disk to be gravitationally unstable are defined by Toomre (1964). A disk has to have globally

$$\frac{M_{disk}}{M_\star} \geq \frac{h}{r} \tag{2.10}$$

and locally

$$Q \equiv \frac{c_s\Omega}{\pi G\Sigma} \leq Q_{crit} \tag{2.11}$$

where $1 < Q_{crit} < 2$ is a dimensionless measure of the threshold below which instability sets in, called Toomre Q parameter. This criterion requires rather high surface densities, more than one order of magnitude higher than the Minimum Mass Solar Nebula (MMSN) (Armitage 2010). The

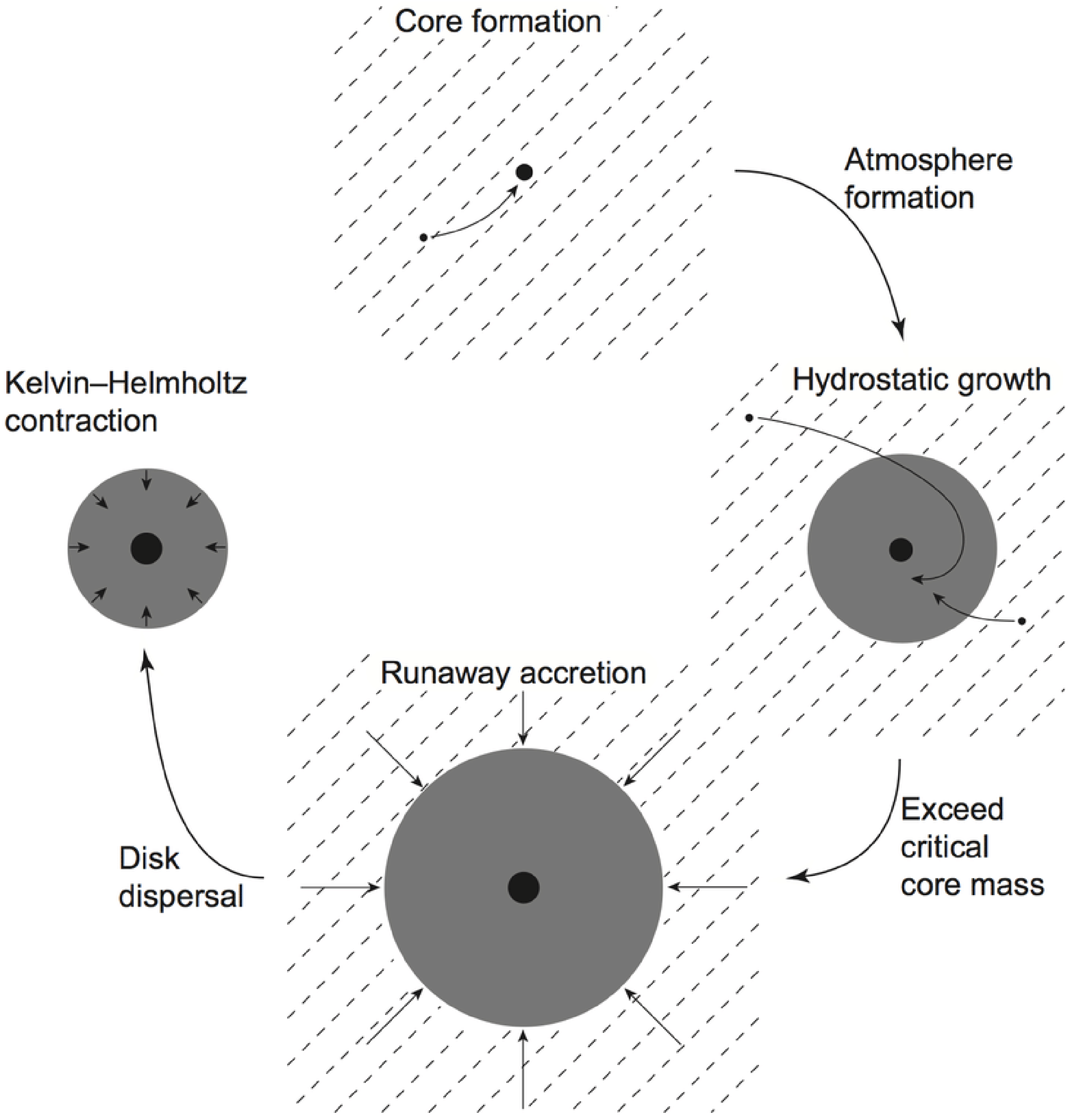

Figure 2.3: The four stages of giant planet formation via core accretion as demonstrated in Armitage (2010). The process starts from cores of solid material, which attract mass from their surroundings. When the body has reached a critical size, it triggers runaway accretion up to a certain mass, when it eventually contracts.

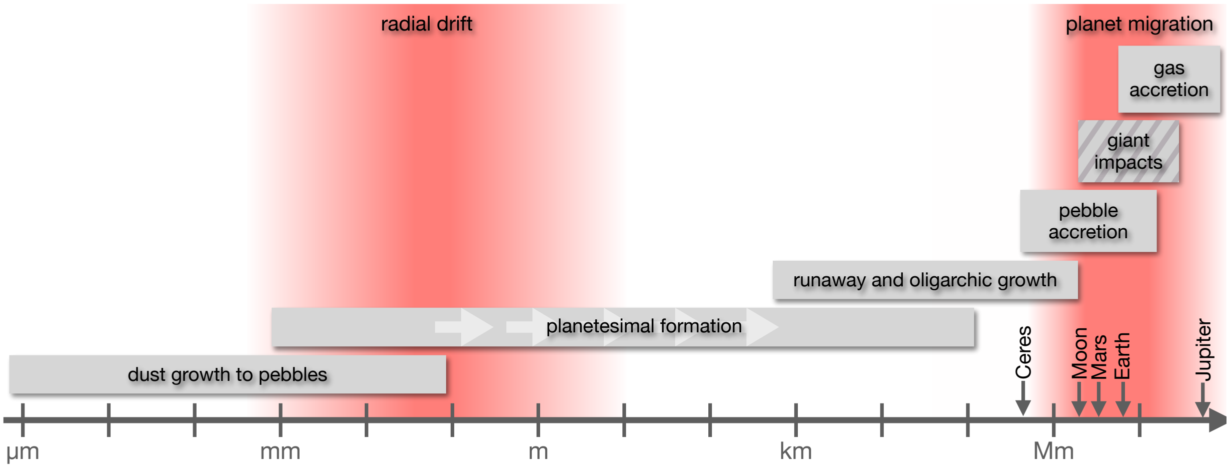

Figure 2.4: Overview of processes involved in planet formation and size scales at which they operate as in (Drazkowska et al. 2022). The grey rectangulars represent the known growth processes and the red shaded regions represent where the radial mass redistribution is effective. The white arrows in the planetesimal formation box represent the lack of the intermediate sizes during the collapse of pebble clouds. The giant impacts may happen both before and after the protoplanetary gas disk disperses, while the other processes happen in the presence of gas.

disk instability is therefore applied better in massive disks and in their cold regions. If the right temperature conditions apply to the clump the gravity overcomes gas pressure, and a massive, gas-rich planet forms. The coldest regions are at large radial distances, therefore GI can explain the formation of gas giants are large separations within a reasonable timescale.

Since GI results in fragmentation, we can estimate the masses than can be produced. The disk should be able to efficiently radiate its thermal energy for fragmentation to occur. The cooling timescale has to be shorter than one orbital period (Shlosman & Begelman 1989), otherwise a clump would have a chance to collide with other clumps and generate more heating, instead of cooling down and fragmenting into a dense clump. This leads to a characteristic object mass of $M_p\ \pi\lambda^2\Sigma$. For a given Solar mass star, disk scale height $h/r = 0.05$ and $Q_{crit} = 1.5$ this mass is independent of the orbital separation and it gives $M_p \approx 8M_J$, where M_J is the mass of Jupiter. (Armitage 2010)

In summary, disk instability could be a potential candidate for the formation of very massive planets, but it requires high surface density which is likely to be observed only in the very early stages of the protoplanetary disk when the accretion rate is large. We have not included GI models in this thesis as we focus on the pebble accretion scenario (see Section 2.2.3 and chapter 4).

2.2.3 Pebble accretion

Current observations show that there is gas and dust present in the protoplanetary disks throughout the evolution of the disk, including evolved times when planetesimal-sized objects have already formed. Therefore, a planet might interact with small particles (pebbles) and grow in mass as shown in Figure 2.4 in the right part. Pebble accretion is a process that can apply to bodies that are Mm in size.

Not every particle can collide with a planetary core. Small particles (St << 1) follow the gas since they are tightly coupled via aerodynamic forces. Therefore they do not interact with the core and flow around it. Objects with St >> 1 are mot coupled to the gas and they collide only if their trajectories crosses the geometric cross-section of the core. The geometric cross section is simply,

$$\sigma = \pi R_p^2 \left(1 + \frac{\upsilon_{esc}^2}{\delta\upsilon^2}\right) \tag{2.12}$$

where R_p is the radius, $\delta\upsilon$ is the relative velocity between the core and the pebble and

$$u_{esc} = \sqrt{\frac{2GM_p}{R_p}} \tag{2.13}$$

is the escape velocity. M_p is the mass of the accreting core and G the gravitational constant.

There is a category of particles that has Stokes number from $10^{-3} < \mathrm{St} < 1$ (typically cm to dm-sized particles depending on the location in the disk) and is moderately coupled to the gas. These are the particles called pebbles and they are responsible for the pebble accretion scenario (Ormel & Klahr 2010; Lambrechts & Johansen 2012). Particles of this size feel both gravitational and aerodynamic forces (gas drag) during their encounter and they lose angular momentum leading to accretion onto the planetary core as they spiral into the Hill sphere of the planet. The Hill sphere of an object is

$$R_H = \left(\frac{m_p}{3M_p}\right)^{1/3} \alpha_p \tag{2.14}$$

where m_p is the mass of a planetesimal (for pebbles it is negligible, M_p the mass of the planet and the α_p the semi-major axis of the object. In order for the pebbles to accrete onto the protoplanet, their stopping time tstop should be smaller than the encounter time between the pebble and the planet (Drazkowska et al. 2022). The feeding zone of pebbles is much larger than the one for the planetesimals due to the gas drag. Therefore the radius that the planet can accrete from can contain a very large reservoir of pebbles. Even if the pebble accretion efficiency is not large, the vast amount of pebbles can contribute to the fast growth of the planet (Guillot et al. 2014; Ormel 2017).

Due to the obvious difficulties for a core to grow more that $50 - 100\mathrm{M}_\oplus$ (the pebble isolation mass increases with the radial distance) at wider orbits, the gas disk phase remains supported by accretion heat and in hydrostatic balance, leading the core to accrete only a thin layer of gas (hydrogen and helium) mixed with large amounts of water vapor obtained by the sublimation of the icy particles. Consequently, the presence of ice giants such as Uranus and Neptune can be explained at wider orbits. According to Lambrechts et al. (2014), apart from the solar system, most of the exoplanets that have been discovered at very large separations from the star must be similar to the ice giants unless the very unlikely case that a core grows more than $50\mathrm{M}_\oplus$, within the disk life-time. The pebble accretion models have some limitations as they usually require constant fluxes of pebbles which might not be easily feasible when the observed disks are abundant in sub-structures.

2.2.4 Isolation mass

In the pebble accretion scenario, there is an upper limit that the planetary core can reach and it is called pebble isolation mass (Lambrechts et al. 2014). When the core mass becomes too massive, it opens a gap in the surrounding gas disk, terminating the flow of the pebbles towards the planetary core stopping them at the pressure maxima outside of the planet location. Therefore the planet cannot grow any further, limiting this way its mass to the isolation mass.

$$M_{iso} \approx 25 M_{\oplus} \left(\frac{H/r}{0.05}\right) \left(\frac{M_{\star}}{M_{\odot}}\right) \tag{2.15}$$

As the planet grows, the pebble isolation mass changes and the pressure gradient modifies the rotation velocity of the gas, which halts the drift of pebbles to the core. The value of the pebble isolation mass depends dominantly on the orbital radius through the disk aspect ratio, $\mathrm{M_{iso}}$ $(\mathrm{H}/\alpha)^3$. Therefore the pebble isolation becomes harder to attain at wider orbital separations. In our study in chapter 4 (Zormpas et al. 2020), we find that the isolation mass changes if an ideal equation of state is used since the disk scale height decreases faster.

When the isolation mass is reached, the gas is accumulated in an area outside of the planet's location leading to the formation of a ring that acts as a trap for gas and dust. These rings are signals of planet formation and they are visible in many images as in Andrews et al. (2018b).

2.2.5 Planetesimal formation via streaming instability

In order to grow planets via pebble accretion, planetesimals should be formed first and fast, so that planetary cores can form later. A prominent scenario is the streaming instability, suggested by Youdin & Goodman (2005). Similar to the gravitational instability the solid particles concentrate into clumps which can gravitationally collapse and form planetesimals. In several studies (Blum et al. 2017; Nesvorný & Vokrouhlický 2019), it was found that planetesimals with sizes of around 100 km were formed in the separation of the asteroid belt (Simon et al. 2016; Schäfer et al. 2017; Klahr & Schreiber 2020), but in order to work, pebbles need to have a Stokes number of $\mathrm{St} \geq 10^{-3}$ and the dust-to-gas ratio should in the order of unity in the mid-plane (Carrera et al. 2016; Li & Youdin 2021).

2.2.6 Radial drift and observations

In observations there are are several proofs that the radial drift is a key factor of planet formation. For example, it is needed to explain the difference between the radial extend of the gas and millimeter dust disk (Drazkowska et al. 2022). If this difference is larger than a factor of two then radial drift can be the reason for it Facchini et al. (2017); Trapman et al. (2020). For example as

Facchini et al. (2019) found, CX Tauri is surrounded by a disk with a gas radii five times larger than the dust radii. Radial drift could explain this difference. Another explanation could be that the current instruments are not sensitive enough to detect accurately the outer gas radii (Carney et al. 2018). Moreover, it can explain the sharp decrease of the dust emission in the outer part of a disk as it has been predicted by Birnstiel & Andrews (2014); Cleeves et al. (2016).

2.2.7 Turbulence

Protoplanetary disks are not static and they evolve with time. Since the gas is dominating the mass of the disk, there are equations that approximate the gas surface density $\Sigma(\mathrm{r}, \mathrm{t})$ evolution. Since the disk mass has to be conserved the evolution of $\Sigma(\mathrm{r}, \mathrm{t})$ can be expressed by the continuity equation as:

$$r\frac{\partial \Sigma}{\partial t} + \frac{\partial}{\partial r}(r\Sigma \upsilon_r) = 0 \tag{2.16}$$

in cylindrical coordinates, where υ_{r} is the gas radial velocity.

The disk mass is also depleting with time and there has to be accretion onto the star. Accretion is not a process that one can easily think of, as an object in orbit can never accrete to the star unless there are other forces that will push it inwards. Since the gravitational force is a central force, this can happen only if there is a process that reduces the semi-major axis and consequently makes the gas to lose angular momentum. This is known as the angular momentum problem and is a known challenge in the disk accretion theory. Therefore, accretion can only be possible through a mechanism that can be friction or more well known as viscosity (Shakura & Sunyaev 1973). Since the disk is a fluid and there is differential rotation depending on the semi-major axis, we can divided the disk in infinite rings of infinitesimal size. Due to the differential rotation, there is a shear caused between two adjacent gas rings and while they exchange mass, angular momentum is transported outwards leading to the inner ring to move inward. Therefore, the inner regions move inwards and accrete onto the star while the outer disk spreads outwards and the disk radius increases with time (Lynden-Bell & Pringle 1974a). So when a viscous fluid is considered, the above equation becomes

$$\frac{\partial \Sigma}{\partial t} = \frac{3}{r}\frac{\partial}{\partial r}\left[r^{1/2}\frac{\partial}{\partial r}(\nu \Sigma r^{1/2})\right] \tag{2.17}$$

where $\nu(\mathrm{r})^{\gamma}$ is the kinematic viscosity. There has to be noted that this is not a microscopic process that originates from the gas particles motion, as in terrestrial fluids the molecular viscosity is so small that it could never lead to accretion in the lifespan of the observed disks. It is instead a turbulent effective viscosity. The source of viscosity can be one of the many mechanisms that have been proposed through the years. One prime example is the magneto-rotational instability (MRI) (Balbus & Hawley 1991), or the graviational instability (GI) (Lin & Pringle 1987) or lastly the vertical shear instability (VSI) (Nelson et al. 2013; Stoll & Kley 2014).

Another way that can transport angular momentum is disk winds (see Turner et al. (2014) and the references therein) but we do not explore this option in this thesis. Instead, the turbulence can be parameterized and described by the α model as in Shakura & Sunyaev (1973)

$$\nu = \alpha \frac{c_s^2}{\Omega} = \alpha c_s H \tag{2.18}$$

where H is the scale height and c_s the isothermal sound speed

$$c_s = \sqrt{\frac{k_B T}{\mu m_H}} \tag{2.19}$$

where k_B is the Boltzmann constant, T the gas temperature, μ the mean molecular weight and m_H is the hydrogen mass. The α is a dimensionless parameter that controls how strong the viscosity is and measures the efficiency of angular momentum transport due to turbulence. We can constrain $\alpha < 1$ as the turbulent velocities cannot be supersonic. The smaller the α, the less turbulence. In our studies chapter 5 we find that this value should be $\alpha < 10^{-3}$ but it can range anywhere between $10^{-5} < \alpha < 10^{-1}$. The most common way to determine the value of α is to measure the non-thermal broadening of molecular emission lines, that lead to values $\alpha < 3 \cdot 10^{-3}$ (Flaherty et al. 2018; Teague et al. 2018).

The α-model does not come without its limitations. The α-value is usually considered to be homogeneous throughout the disk but there is no evidence to support this. It may vary according to radius, temperature or density as far as we know. Especially if there are dead-zones in the disk (Gammie 1996), which are locations where the ionization is low, it is expected that the viscosity would be lower there.

Apart from the gas, this turbulence affects also the dust in the disk and acts as diffusivity as if $\nu = 0$ is set in Eq. 2.17 no diffusion can occur, while the surface density stays constant. The dust diffusivity is modeled as

$$D_d = \frac{\nu}{1 + St^2} \tag{2.20}$$

and it shows that smaller particles that are coupled with the gas are affected greater than the larger ones (Youdin & Lithwick 2007).

2.2.8 Steady-state solution

For some applications it is useful to derive a solution which is independent of ν. Therefore, Eq. 2.17 can be integrated numerically to be applied in numerical codes. The simplest solution is to consider $\frac{\partial}{\partial t} = 0$ in Eq. 2.17 and a steady state solution for the disk can be obtained

$$\nu \Sigma = \frac{\dot{M}}{3\pi} \left(1 - \sqrt{\frac{R_\star}{r}} \right) \tag{2.21}$$

where M is the gas accretion rate and $R_\star$ is the zero torque boundary ($d\Omega/dR = 0$) or simpler the inner disk boundary. For large radii ($r >> R_\star$) the equation simplifies to

$$\dot{M} = 3\pi \nu \Sigma \tag{2.22}$$

and it shows that the viscosity is inversely proportional to the gas surface density. This relation is used to model the effect of planets in the disk in chapter 5, by altering locally the viscosity.

2.2.9 Self-similar solution

A solution that is more commonly used is the self-similar solution (Lynden-Bell & Pringle 1974a). Protoplanetary disks evolve with time and the accretion rate changes over time therefore it is better to obtain a general solution that requires the knowledge of the dependence in the viscosity in the form of a power-law ($\nu \propto \mathrm{r}^{\gamma}$). Solutions that solve Eq. 2.17 with this assumption on the viscosity, are usually called self-similar solutions.

The solution has the following form:

$$\Sigma_g(r) = \Sigma_0 \left(\frac{r}{r_0}\right) exp\left(\frac{-r}{r_c}\right) \tag{2.23}$$

where $\mathrm{r_c}$ is the cut-ff radius (or characteristic radius) and Σ_0 and $\mathrm{r_0}$ are normalization constants

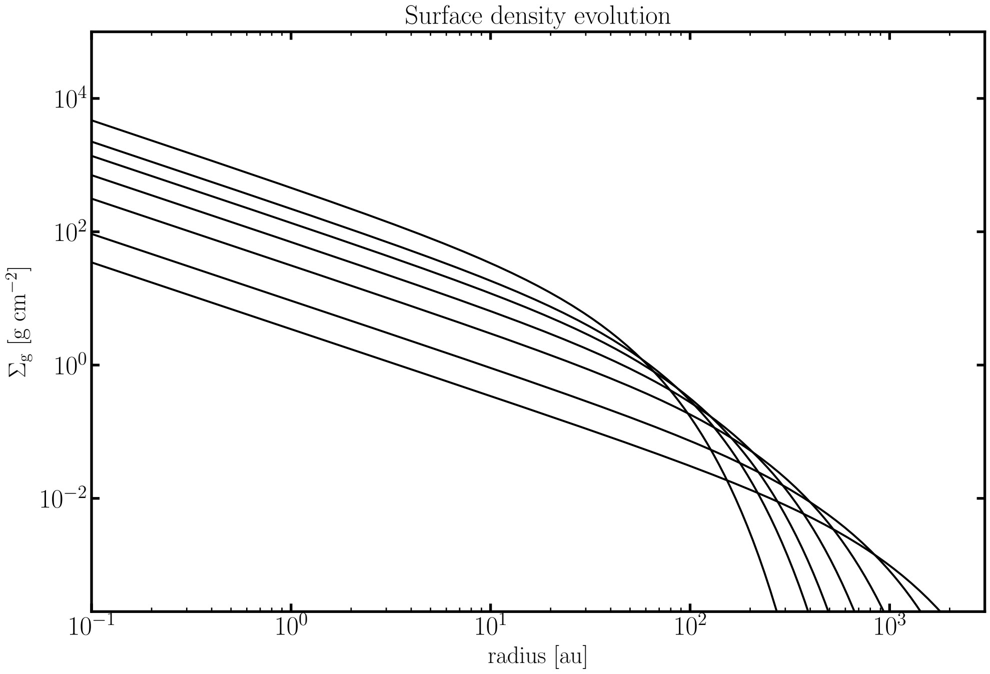

Figure 2.5: Surface density evolution of a disk. The self-similar solution Eq. 2.23 is plotted from 0 to 5 Myr for a viscosity $\nu \propto \mathrm{r}$. The viscous spreading is visible as the time increases and the radius of the disk increases too. The initial conditions are $\mathrm{r_c} = 30$ au and $\alpha = 10^{-2}$.

(where the viscosity is also included). From this equation it can be shown that the disk mass decreases over time and the characteristic radius increases to conserve angular momentum, leading to the expansion of the disk. In Figure 2.5 we see the self-similar solution as a function of time with a characteristic radius $\mathrm{r_c} = 30$ au initially. The surface density decreases over time as a power-law for radii $\mathrm{r} < \mathrm{r_c}$. For the regions with $\mathrm{r} > \mathrm{r_c}$ the surface density decreases rapidly due to the exponential drop. While the disk is expanding the exponential factor become less and less important and the surface density follows the same evolution as the other part of the disk. From this figure is visible the description given above. Only the inner part of the disk is accreting while the outer one is expanding.

This self-similar form is used to evolve the disks analytically in chapter 5, and to compare the observed properties (masses or radii) with our numerical results.

Chapter 3

Radiative transfer

The transport of energy through radiation is of great importance in various astrophysical phenomena from planet, to star and galaxy formation. Since radiative transfer (RT) calculations can be a challenging topic, most of the times numerical solutions are required through codes that can treat radiative transfer recipes. In astrophysics, radiative transfer is the main cooling and heating process, while it is also the main link between theory and observations.

Radiative transfer can help shed light to the new features that have been revealed by the high resolution images (see Figure 1.5). These structural properties such as non-axisymmetric sub-structures, spirals, gaps, etc, can be reconstructed by detailed radiative transfer models and the temperature profile of disks can be calculated. Multiple radiative transfer packages have been developed and most of them are following a "Monte Carlo" numerical approach, named after the town of Monte Carlo. This is a probabilistic method which can simulate multiple scattering processes (see next sections), by following the path of a photon from one scattering event to another by using random numbers. With this method the dust temperature can be computed and with further assumptions a model of protoplanetary disk can be made reconstructing some of these observed features.

Radiative transfer calculations are not an easy task. The complexity lies on scattering and the fact that radiation affects the state of the medium itself. While the radiative transfer approximation is easy if the injection and the removal rates of the photons is known, scattering introduces random effects as the photons scatter on dust particles in arbitrary directions and cannot anymore be traced back to its origin. In chapter 4 we explore the effect of radiative transfer on pebble accretion without scattering, while the effect of scattering is explored in chapter 5.

3.1 Opacity

The ability of a medium to absorb photons is given by the mean free path $\mathrm{l}_{\mathrm{free}} = (\sigma \mathrm{n})^{-1}$ of a photon, where σ is the cross-section and n is the number or particles per unit volume. A photon can travel a finite number of mean free path lengths before it is absorbed by the medium. This number is called optical depth τ_ν. When $\tau_\nu >> 1$, the medium is called optically thick, while a medium with $\tau_\nu << 1$ is optically thin.

Typically, dust mediums are consisted of solids in the form of silicates, carbonaceous materials and ices such as water, CO and more, depending on the distance from the main star. For our understanding, these solids are considered to be spherical with a certain radius even though in general they can have very irregular shapes. Moreover, they are assumed to be a mixture of the typical solids mentioned above since they collide with each other. In protoplanetary disks, the dust mass consists only $\sim 1\%$ of the total mass of the disk. Nevertheless, dust particles are the main source of continuum opacity. Therefore, dust is responsible for the temperature structure of the disk as it is absorbing the stellar irradiation while it is re-radiated in the infrared. At every location of the disk, the dust opacity is a function of the temperature, the chemical composition of the disk and the particle size distribution. The temperature determines which type of dust and in which form are present and the distribution varies according to possible coagulation and fragmentation within the disk. The cross-section of a dust particle is the geometric cross-section

$$\sigma_{geo} = \pi a^2 \tag{3.1}$$

where a is the particle radius. For multiple particles, the frequency dependent opacity per gram is defined as:

$$\kappa_\nu = \frac{\sigma_{geo}}{m} \tag{3.2}$$

where μ is the particle mass (assuming a spherical particle). Depending on the material of the particle, radiation can be either absorbed or scattered or both. This can be expressed by a number called albedo η_ν, with $\eta_\nu \in [0, 1]$. We define the albedo as

$$\eta_\nu = \frac{\kappa_\nu^{sca}}{\kappa_\nu^{abs} + \kappa_\nu^{sca}} \tag{3.3}$$

where $\kappa_\nu^{\mathrm{abs}}$ and $\kappa_\nu^{\mathrm{sca}}$ are two different but complimentary opacities. The absorption opacity $\kappa_\nu^{\mathrm{abs}} = \eta_\nu \kappa_\nu$ and the scattering opacity $\kappa_\nu^{\mathrm{sca}} = (1 - \eta_\nu)\kappa_\nu$. The sum of the two opacities leads to the total opacity $\kappa_\nu^{\mathrm{abs}} + \kappa_\nu^{\mathrm{sca}} = \kappa_\nu$.

In the inner region of the disk, the disk scale height is much larger than the mean free path of the thermal radiation. While the radiation field is approximately isotropic and blackbody and the flux is proportional to the gradient of the energy density of the radiation $\mathrm{F_{rad}} = -\mathrm{c}\nabla(\mathrm{aT}^4)/(3\kappa_\mathrm{R}\rho)$. The relevant opacity that enters into the equation for the flux is the Rosseland mean opacity (or Rosseland mean) is a weighted average (across frequency) of the opacity of a material, through which electromagnetic radiation is passing.

$$\frac{1}{\kappa_R} = \frac{\int_0^\infty (1/\kappa_\nu)(\partial B_\nu/\partial T)\, d\nu}{\int_0^\infty (\partial B_\nu/\partial T)\, d\nu} \tag{3.4}$$

where B_ν is the Planck function. The Rosseland mean covers all frequencies (and consequently wavelengths) instead of varying the calculation for every frequency.

3.2 Scattering

As mentioned, scattering complicates radiative transfer calculations massively. While photons can encounter multiple random scattering events they cannot deterministically be traced to their original state. There are approaches to simplify the scattering complexity. The simple case is known as the single scattering approximation and it is considered for very optically thin mediums $\tau << 1$. The lower the optical depth the better this assumption works. In this case it is assumed that every photon that scatters into the line of sight experienced no scattering events before that. On the other hand, if we tackle the problem to its core, we can argue that we cannot isolate one ray and study its path as the rays affect each other when crossing. Therefore, we would require to solve all rays simultaneously and this is where its complexity lies. The simplest example of ray coupling is a process called isotropic scattering. In this case a medium consisting of dust particles can scatter radiation to arbitrary directions while the direction of a photon in a scattering event has no dependence in the direction it had before the event.

Scattering can be divided into three regimens which can be defined by the ratio of the size of the particle over the wavelength, the so-called size parameter x,

$$x = \frac{2\pi a}{\lambda} \tag{3.5}$$

where λ is the wavelength. Again, assuming spherical particles there are three different types of scattering. When x << 1, the particle is much smaller than the wavelength and the scattering is called the Rayleigh scattering. The solution then can be simplified with the Mie theory for a given refractive index. The Mie theory is a series approximation to the Maxwell equations, that calculates the scattering and absorption cross sections for all wavelengths for spherical particles. In the Rayleigh regime the scattering opacity goes as $\kappa_\nu^{\mathrm{sca}} \sim \lambda^{-4}$ and the absorption opacity as $\kappa_\nu^{\mathrm{abs}} \sim \lambda^{-1}$. When x $\simeq$ 1 and the particle has a similar size to the wavelength, the Maxwell equations need to be solved to calculate the scattering. Lastly, when x >> 1 and the particle size is much larger than the wavelength, it is in the geometric optics regime and Mie theory cannot be applied as more terms are required in the series expansion.

3.2.1 Effects of grain growth on dust opacity

The opacity is wavelength dependent, meaning that a particle can absorb or scatter changes with the size of the particle. Scattered light probes particle sizes in the order of $0.01 - 10\,\mu$m and these observations are responsible for the surface layer of the disk. Longer (from far-IR to mm) wavelengths probe deeper in the disk (mid-plane) where most of the mass is. The opacity can then be approximated as a power-law κ_ν^β where β is the spectral index that depends on the maximum grain size of the dust particles (Miyake & Nakagawa 1993), the porosity and the composition of the particle and the grain size distribution. This value is usually in the order of 1 for mm particles (see Figure 3.1). As mentioned Section 2.2, the distribution is approximated as a power-law (Natta et al. 2007)

$$dN = n(a)^{-q} da \tag{3.6}$$

with a values that usually lies between 2.5-3.5. Through the value of the spectral index, the disk dust mass can be estimated. When observing at wavelengths larger than the dust size the value of β is getting smaller as these particles cannot absorb or emit at this wavelength. These are shown in Figure 3.1 from Birnstiel et al. (2018) where in the top panel the scattering and absorption opacity, the spectral index $\beta = \partial \ln \kappa_\nu^{\mathrm{abs,tot}} / \partial \ln \nu$ and the extinction probability (see Birnstiel et al. (2018) for details) are shown as a function of the maximum particle size a_{max}. A key outcome of this figure is that size distributions that extend up to $a_{\mathrm{max}} \gtrsim 100\,\mu$m, the scattering opacity $\kappa_\nu^{\mathrm{sca,tot}}$ exceeds the absorption opacity $\kappa_\nu^{\mathrm{abs,tot}}$.

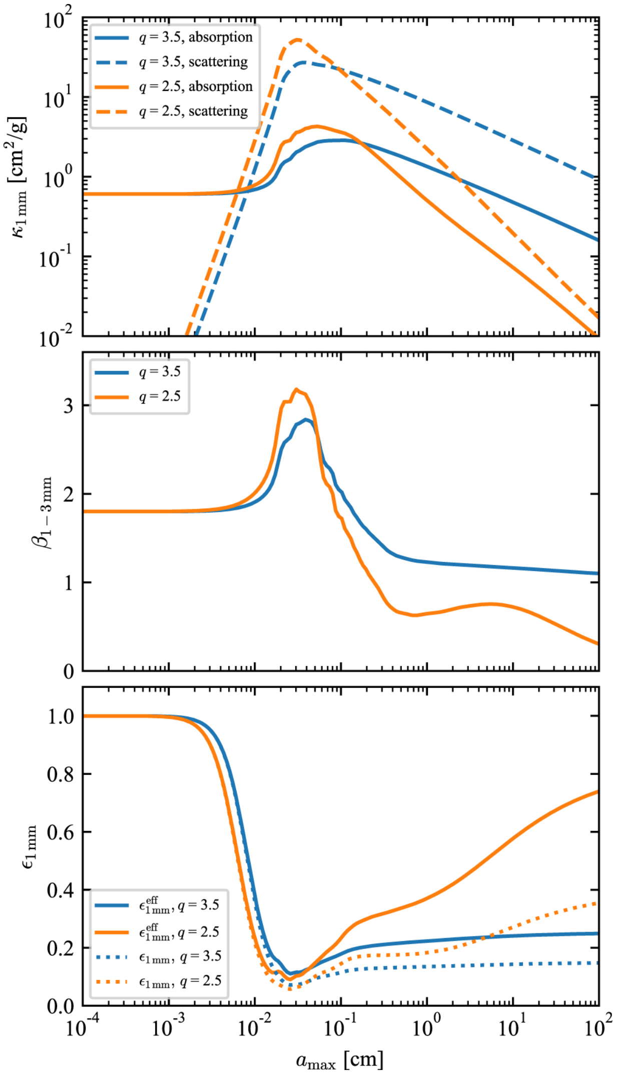

Figure 3.1: Particle size averaged opacities adapted from Birnstiel et al. (2018). **Top panel**: scattering ($\kappa_\nu^{\mathrm{sca,tot}}$) and absorption ($\kappa_\nu^{\mathrm{abs,tot}}$) opacity at 1 mm. **Middle panel**: spectral index β measured at 1–3 mm. **Bottom panel**: extinction probability $\epsilon^{\mathrm{eff}}_{1\,\mathrm{mm}}$. The assumed size distribution for these averaged properties follows a power law $n(a) \propto a^{-q}$ from the minimum size of 10^{-5} cm up to maximum size $\mathrm{a_{max}}$. Blue lines denote the MRN-slope of q = 3.5, and orange lines correspond to q = 2.5.

3.3 Application of RT to our work

In chapter 4 we have to solve the time dependent equations of radiation hydrodynamics. In our work this was performed by the code $PLUTO$ (Mignone et al. 2007), by using a specific radiation hydrodynamics module developed by Kolb et al. (2013).

The solver is based on the flux-limited diffusion approximation in the two-temperature approach. The equations are solved in the co-moving frame in the frequency independent (gray) approximation. The hydrodynamics is solved by the different Godunov schemes implemented in $PLUTO$, and for the radiation transport we use a fully implicit scheme. The resulting system of linear equations is solved using matrix solvers that are available in the $PETSc$ library. We briefly present the methodology as is described by Kolb et al. (2013). We used the solver in spherical coordinate systems in parallel computing using MPI, without irradiation by a the central star.

3.3.1 Flux-limited diffusion approximation

The main equations that describe this analysis, are the Euler equations of ideal hydrodynamics with an extra equation for the radiation energy that comes from the two-temperature approximation. To follow the transport of radiation, we applied the flux-limited diffusion approximation and treated the exchange of energy and momentum between the gas and the radiation field with additional terms in the gas momentum and energy equations. The relevant equations can be found in chapter 4.

The system of equations cannot be solved without additional assumptions for the radiative flux **F**. As in Kolb et al. (2013), we used the flux-limited diffusion approximation (FLD) where the radiation flux is given by a diffusion approximation

$$\mathbf{F} = -\lambda \frac{c}{\kappa_R \rho} \nabla E \tag{3.7}$$

where κ_R is the Rosseland mean opacity. The importance of the flux-limiter λ, is that describes the transition from very optically thick regions with $\lambda = 1/3$ to optically thin regimes, where $\mathbf{F} \rightarrow -\mathrm{cE}\frac{\nabla \mathrm{E}}{|\nabla \mathrm{E}|}$. This leads to the formal definition of the flux-limiter, which is a function of the dimensionless quantity

$$R + \frac{|\nabla E|}{\kappa_R \rho E} \tag{3.8}$$

with behavior

$$\lambda(R) = \begin{cases} \frac{1}{3}, R \rightarrow 0 \\ \frac{1}{R}, R \rightarrow \infty \end{cases} \tag{3.9}$$

The flux-limiters have to fulfill the equation 3.9 in the given limits and describe the behavior between the limits approximately. For our purpose, we use the flux limiter from Kley (1989).

$$\lambda(R) = \begin{cases} \frac{2}{3+\sqrt{9+10R^2}}, & 0 \leq R \leq 2 \\ \frac{10}{9+\sqrt{180R+81}}, & 2 < R \leq \infty \end{cases} \tag{3.10}$$

In general, the equations need to be solved for every frequency that there is in the physical problem. For simplicity reasons, we used the so-called gray approximation, where all radiative quantities plus the opacity, are integrated over all frequencies.

Chapter 4

Solid accretion onto planetary cores in radiative disks

The contents of this chapter were published in the Astronomy & Astrophysics Journal. Credit: Solid accretion onto planetary cores in radiative disks, Zormpas et al., A&A 638, A97 (2020), under the Creative Commons Attribution License 4.0.

Some contents have been part of an initial study during my Master Thesis (see Section 4.4 for more details).

4.1 Abstract

The solid accretion rate, which is necessary to grow gas giant planetary cores within the disk lifetime, has been a major constraint for theories of planet formation. We tested the solid accretion rate efficiency on planetary cores of different masses embedded in their birth disk by means of 3D radiation-hydrodynamics, where we followed the evolution of a swarm of embedded solids of different sizes. We found that by using a realistic equation of state and radiative cooling, the disk at 5 au is able to efficiently cool and reduce its aspect ratio. As a result, the pebble isolation mass is reached before the core grows to $10\,\mathrm{M}_\oplus$, thus fully stopping the pebble flux and creating a transition disk. Moreover, the reduced isolation mass halts the solid accretion before the core reaches the critical mass, leading to a barrier to giant planet formation, and this explains the large abundance of super-Earth planets in the observed population.

4.2 Introduction

The formation of the solid core of gas giant planets is still an open question in regards to the core accretion model (Pollack et al. 1996). The timescale on which a core of critical mass must be formed in order for runaway gas accretion to set in is given by the disk lifetime. Depending on the stellar properties, this period has been found observationally to be between 3 and 10 Myr for Solar-type stars (Ribas et al. 2015). On this short timescale, interstellar medium μm dust grains must grow by almost 14 orders of magnitude in size and 40 orders of magnitude in mass. The critical core mass value at which the hydrostatic equilibrium breaks down is in the $5-20\,M_\oplus$ range (Mizuno 1980; Béthune 2019), depending on how the envelope is able to cool (Rafikov 2006; Piso et al. 2015), and it is strongly dependent on the adopted opacity (Mordasini 2014; Ormel 2014; Brouwers & Ormel 2019). Furthermore, due to the interaction between the planetary core and its natal circumstellar disk, planets migrate and can be accreted onto the central star if no other physical processes stop them.

In order to match the observed population of gas giants, a faster growth timescale is needed in the core accretion paradigm. In recent years, two promising mechanisms have been studied. Under certain circumstances, the streaming instability might allow for the growth of planetesimal-sized objects directly from small dust particles (see e.g., Johansen et al. 2014, for a review), while pebble accretion might enhance the solid accretion on growing planetary cores (Ormel & Klahr 2010; Lambrechts & Johansen 2012).

Although these mechanisms have successfully reduced the time required to form giant planetary cores, a further barrier must be overcome in order to reach the core mass necessary to ignite the rapid gas accretion phase. A growing planet is able to open a partial gap in the surrounding gaseous disk by generating a pressure maximum, which effectively halts the inward drift of solids in the disk, in particular the pebble component. The mass at which the pebble flux is halted has been defined as the pebble isolation mass by Lambrechts et al. (2014), and it varies based on the local physical properties of the disk (Bitsch et al. 2018; Ataiee et al. 2018; Picogna et al. 2018).

Within this framework, we study the pebble accretion rate and isolation mass, in realistic 3D radiative hydrodynamical simulations, and how this affects the efficiency of gas giant planet formation. In Sect. 4.3 we describe the numerical set-up adopted to model the solid evolution and accretion onto a planetary core embedded in a disk with a realistic equation of state. We then discuss our results in Sect. 4.5 and draw the main conclusions in Sect. 4.6.

4.3 Numerical methods

We consider the same setup as in Picogna et al. (2018) to allow for a direct comparison; the only exception is that instead of using a locally isothermal equation of state for the gas, we adopted the ideal equation of state and included the radiative transfer in the flux-limited diffusion approximation (FLD) (Kolb et al. 2013), and we consider laminar viscous disks.

4.3.1 Gas component

The disk was initially set in an axisymmetric configuration ranging from 2.08 to 13 au (0.4-2.5 in code units, where the unit of length is 5.2 au). In the vertical direction, the domain extends from $\theta_{min} = 83^\circ$ to $\theta_{max} = 90^\circ$ (half disk), corresponding to 5 disk scale heights H in the initial setup, and in the ϕ direction from $\phi_{min} = 0^\circ$ to $\phi_{max} = 360^\circ$ (full disk). In the three coordinate system's directions (r, θ, ϕ), we used a $600 \times 64 \times 1024$ grid resolution. The grid cells are spaced logarithmically in the radial, and linearly in the other directions. The main parameters of the simulations are summarized in Table 4.1.

The initial density profile created by force equilibrium is given by

$$\rho(R,Z) = \rho_0 \left(\frac{R}{R_\mathrm{p}}\right)^p \exp\left\{\left[\frac{GM_\mathrm{s}}{c_\mathrm{s}^2}\left(\frac{1}{r} - \frac{1}{R}\right)\right]\right\}, \tag{4.1}$$

where $R = r\sin\theta$ describes the cylindrical radius, ρ_0 is the gas mid-plane density at the planet location $R = R_\mathrm{p} = 1$, $p = -1.5$ the density exponent, and c_s is the isothermal sound speed. The disk's initial aspect ratio was set to $h = H/R = 0.05$, which corresponds to a temperature profile of

$$T(R) = T_0 \left(\frac{R}{R_\mathrm{p}}\right)^q, \tag{4.2}$$

with $q = -1$ and $T_0 = 121\,\mathrm{K}$.

The gas moves with an azimuthal velocity given by the Keplerian speed around a $1\,\mathrm{M}_\odot$ star, corrected by the pressure support (Nelson et al. 2013):

$$\Omega(R,Z) = \Omega_\mathrm{K}\left[(p+q)h^2 + (1+q) - \frac{qR}{\sqrt{R^2+Z^2}}\right]^{\frac{1}{2}}, \tag{4.3}$$

where Ω_K is the Keplerian orbital frequency. At the inner and outer boundary, we adopted reflective conditions, and we damped the density as well as the radial and vertical velocity to the initial values at the timescale of a fraction of a local orbit in order to prevent reflection of the spiral wave caused by the planet-disk interaction onto the boundary. The damping was applied in the intervals $[0.4, 0.5]\ r_\mathrm{p}$ and $[2.3, 2.5]\ r_\mathrm{p}$. For the vertical boundaries, a mirror condition was implemented at the disk midplane, while an open boundary was applied in the disk atmosphere, and in the azimuthal direction a periodic condition was applied. We adopted a constant of $\alpha = 5\cdot 10^{-4}$, which is consistent with values generated by hydrodynamical turbulences (see e.g., Stoll et al. 2017).

We employed the radiation hydrodynamics module developed by Kolb et al. (2013) for the PLUTO code (Mignone et al. 2007). The solver is based on the FLD approximation in the two-temperature approach. The equations were solved in the co-moving frame in the frequency-independent (gray) approximation.

The motion of the gas is described by the Navier-Stokes equations (eqs. 4.4, 4.5, 4.6) that are coupled with radiation transport (eq. 4.7)

$$\frac{\partial}{\partial t}\rho + \nabla\cdot(\rho\boldsymbol{v}) = 0, \tag{4.4}$$

$$\frac{\partial}{\partial t}\rho\boldsymbol{v} + \nabla\cdot(\rho\boldsymbol{v}\otimes\boldsymbol{v} - \boldsymbol{\sigma}) + \nabla p = -\rho\nabla\Phi, \tag{4.5}$$

$$\frac{\partial}{\partial t}e + \nabla\cdot[(e+P)\boldsymbol{v}] = -\rho\boldsymbol{v}\cdot\nabla\Phi + (\boldsymbol{\sigma}\cdot\nabla)\boldsymbol{v} - \kappa_p\rho c(a_R T^4 - E), \tag{4.6}$$

$$\frac{\partial}{\partial t}E + \nabla\cdot\mathbf{F} = \kappa_p\rho c(a_R T^4 - E), \tag{4.7}$$

where the first three equations describe the evolution of the gas motion where ρ is the gas density, P corresponds to the thermal pressure, $\boldsymbol{v}$ is the velocity, $e = \rho\epsilon + 1/2\rho v^2$ the total energy density

Table 4.1: Model parameters

Parameter	Value
Grid	
Radial range [au]	2.08 – 13
Vertical range [H]	5
Azimuthal range [rad]	2π
Radial resolution	600
Polar resolution	64
Azimuthal resolution	1024
Gas	
Density index p	-1.5
Temperature index q	-1.0
Eqn. of state	Ideal, Isothermal
H/R	0.05, 0.02
α	$5 \cdot 10^{-4}$
γ	1.4, 1
μ	2.35
Planet	
Planet mass [$M_\oplus$]	5, 10, 100
Dust	
Particle size [cm]	$0.01, 0.1, 1, 10, 30$ $100, 300, 10^3, 10^4, 10^5$
Total number	10^6

(i.e., the sum of internal and kinetic energy) of the gas without radiation, $\epsilon = C_V T$ is the specific internal energy in which C_V is the specific heat capacity (assumed constant here), $\boldsymbol{\sigma}$ is the viscous stress tensor, and Φ is the gravitational potential. This system of equations is closed by the ideal gas equation of state

$$P = (\gamma - 1)\rho\epsilon = \rho \frac{k_B T}{\mu m_H}\,, \tag{4.8}$$

where γ is the ratio of specific heats, T represents the gas temperature, k_B is the Boltzmann constant, $\mu = 2.35$ the mean molecular weight, and m_H is the hydrogen mass.

The evolution of the radiation energy density E is given by equation 4.7, where **F** denotes the radiative flux, which was computed in the FLD approximation as in Kolb et al. (2013), κ_P is the Planck mean opacity, c corresponds to the speed of light, and a_R is the radiative constant. This implementation does not include the advective transport terms for the radiation energy and radiative pressure work in equations 4.6 and 4.7, since these terms are of minor importance for low-temperature disks. For the computational boundaries, we adopted, for the radiative part, reflective conditions in the radial direction, a symmetric condition at the disk midplane, and a fixed temperature of 5 K in the upper boundary. Period boundaries were applied in the azimuthal direction.

4.3.2 Dust component

The solid fraction of the disk is modeled with 10^6 Lagrangian particles divided into ten size bins as reported in Table 4.1. This approach has the great advantage of modeling a broad range of dynamical behaviors self-consistently, using the same modeled particles. The trade-off is that in the regions of low density, the resolution of the dust population is lower. However, for our study, this is not a problem since we are mainly interested in the dynamical evolution of dust particles; thus we do not take into account collisions between particles or the back-reaction of the dust onto the gas. We study particles with sizes s from 0.1 mm up to 1 km and internal density $\rho_\mathrm{d} = 1\,\mathrm{g\,cm^{-3}}$. The particle sizes were chosen to cover a wide range of different dynamical behaviors. The initial surface density profile of the dust particles is

$$\Sigma_\mathrm{d}(r) \propto R^{-1}. \tag{4.9}$$

This particle distribution leads to an equal number of particles in each radial ring as the grid is spaced logarithmically in the radial direction. The resulting dust profile is steeper than the gas profile, and it allows for a better sampling of the dust dynamics in the vicinity of the planet location. The dust particles were initially placed with a vertical distribution given by the local disk scale height and the dust diffusion coefficient (see e.g., Youdin & Lithwick 2007). The evolution of dust particles is given by the gravitational interaction with the planet and central star, turbulent kicks from the gas that resemble a realistic turbulent behavior, and the drag force from the interaction with the gaseous disk

$$\mathbf{F}_\mathrm{drag} = -\frac{m_\mathrm{d}}{t_\mathrm{s}}\mathbf{v}_\mathrm{r}\,, \tag{4.10}$$

where m_d is the dust particle mass, and t_s is the stopping time which represents the timescale on which the embedded dust particle approaches the gas velocity and, for well-coupled particles, it is given by

$$t_\mathrm{s} = \frac{s\rho_\mathrm{d}}{\rho\bar{v}_\mathrm{th}}\,, \tag{4.11}$$

or, in its dimensionless form (hereafter, Stokes number), as

$$\tau_\mathrm{s} = t_\mathrm{s}\Omega_\mathrm{K}(\mathbf{r})\,, \tag{4.12}$$

which describes the effect of a drag force acting on a particle independently of its location within the disk. Here, $\bar{v}_\mathrm{th}$ represents the mean gas thermal velocity. Dust particles were introduced at the beginning of the full 3D simulation in thermal equilibrium, and they evolve with two different integrators depending on their τ_s (see Picogna et al. 2018, for further details). We do not consider the effect of the disk self-gravity on the particle evolution. Particles that leave the computational domain at the inner boundary re-enter at the outer boundary. This solution allowed us to keep a constant number of particles, which is beneficial from a numerical point of view, and it does not affect the load balance between the computational cores. Adding particles at a constant rate from the outer boundary would only make sense if we were considering the evolution of small planets for longer times. As shown in Fig. 4.5, the disk close to the planet location does not run out of particles within the simulated time even for the fast evolving pebbles. Accreted particles are flagged but were otherwise kept in the simulations (see Sec. 4.5 for further details).

4.3.3 Planets

We embed a planet, with a mass in the range of $[5, 10, 100]\ M_\oplus$, orbiting a solar mass star on a circular orbit with semi-major axes $R_p = 1$ (5.2 au) in code units. The planet does not migrate and its mass is kept fixed. Its gravitational potential is smoothed with a cubic expansion inside its Hill sphere

$$r_\mathrm{H} = r\left(\frac{M_p}{3M_\star}\right)^{1/3} \tag{4.13}$$

(Klahr & Kley 2006). In order to obtain the initial conditions, we evolved the disk for ~ 200 orbits, with lower resolution in the azimuthal direction, until its scale height was not changing considerably. This allowed us to start our simulation with the disk in thermal equilibrium. Subsequently we increased the resolution to the one reported in Tab. 4.1, and added the dust component. After the dust component has been evolved for six orbits in the computational domain, the planetary mass slowly increases over an additional 20 orbits to allow for a smooth initial phase. Each simulation was evolved for 100 orbital periods of the planet when the disk structure is close to a stationary state and further changes are small, so we do not expect them to affect our results.

4.4 How is pebble accretion affected by radiative transfer?

Some contents of the preceding sections were originally part of a Master Thesis project, titled:

> "How is pebble accretion affected by radiative transfer?"

with the translated German title:

> "Wie wird die Akkretion kieselsteingroßer Körper durch Strahlungstransport beeinflusst?",

as part of the Master of Science in Physics of the Ludwig-Maximilians-Universität with the supervision of Prof. Dr. Barbara Ercolano, with a submission date on the 15th of September, 2017. In that study we performed a series of 3-D hydrodynamical simulations using the hydro code PLUTO (Mignone et al. 2007) and the radiative transfer module developed by Kolb et al. (2013). This is the same setup as described above but in the original study we used only two different planets of 10 $\mathrm{M}_\oplus$ and 100 $\mathrm{M}_\oplus$. We evolved the disk according to viscous heating until it reached a stable as already described.

However, the computational demands did not allow for extensive simulations with different planetary masses and an additional isothermal simulation as in the published paper (Zormpas et al. 2020). Moreover, crucial points that have a large impact on the results were not fully investigated as for example the role of radiative transfer in the simulation which is the main outcome of the published study (Zormpas et al. 2020). Moreover, due to the lack of the additional simulations we could not explain the observed result of the low gas giant planet frequency. Furthermore we did not investigate the relation for the pebble efficiency as a function of the particle Stokes number for a 3D disk (see Section 4.5 and Section 4.6).

Therefore as part of my Ph.D., we performed the required simulations for the remaining planetary masses and the isothermal simulation for comparison, we addressed the open questions from the Master Thesis and we expanded the contents to a more comprehensive study that was published in Astronomy & Astrophysics Journal. Credit: Solid accretion onto planetary cores in radiative disks Zormpas et al., A&A 638, A97 (2020),under the Creative Commons Attribution License 4.0. The remaining content of this section are the results and the conclusions as published in the mentioned paper.

4.5 Results

4.5.1 Gas evolution

The presence of a planet significantly alters the gas structure close to its location even if it is not massive enough to open up a gap (see e.g., Lin & Papaloizou 1993; Lambrechts et al. 2014). In Fig. 4.1 we show the azimuthal gas velocity in units of the Keplerian speed as a function of radius. In this case, we compared our results with those of Picogna et al. (2018) for a viscous locally isothermal disk with a disk scale height of $H/R = 0.05$ and with an isothermal case with $H/R = 0.02$. This helps us to understand the influence of radiative cooling. The first thing to notice is that changing the disk aspect ratio changes the pressure support of the gas as well, so that the disk becomes more Keplerian on average, going from $H/R = 0.05$ (purple line) to $H/R = 0.02$ (black line). This plays an important role in the dust evolution because whenever the gas becomes super-Keplerian, the head-wind felt by the dust particles is reduced, meaning that the particles slow their inward migration down or stop it altogether. Thus, for a colder (thinner) disk, smaller planets can halt the dust evolution more easily. As seen from the parameter study probed, a 5 $\mathrm{M}_\oplus$ planet can create a super-Keplerian flow outside its location for an $H/R = 0.02$, while the flow remains sub-Keplerian everywhere for the same planet in a hotter disk ($H/R = 0.05$).

The radiative case lies in the middle of the two cases presented above even though the initial aspect ratio of the disk was 0.05 in this case and the 5 $\mathrm{M}_\oplus$ planet almost pushes the gas to the Keplerian speed (blue line). This points to the fact that the disk was able to effectively cool and adapt to a new equilibrium aspect ratio. This effect is highlighted in Fig. 4.2 where the two isothermal cases are plotted with purple dotted lines for reference. The radiative case settles to a disk scale height that is close to 0.03 at the planet location, with small perturbances in the planet

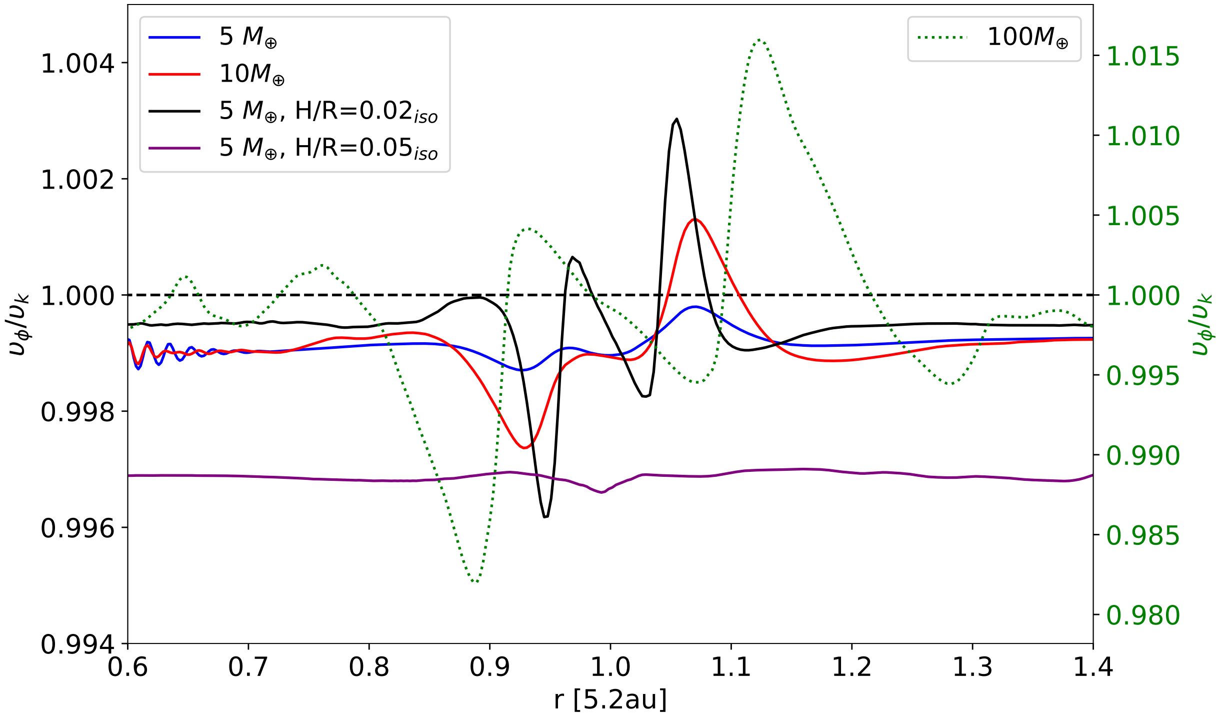

Figure 4.1: Azimuthal gas velocity in units of the Keplerian speed as a function of radius for the different planetary masses and models. When the gas speed becomes super-Keplerian outside the planet location, the dust-filtration process occurs and the pebble isolation mass is reached. The purple line shows the corresponding simulation from Picogna et al. (2018) at the same time span. The 100 $M_\oplus$ planet corresponds to the right axis and it is shown with a green dotted line.

vicinity depending on its mass. The features in the disk scale height can be directly related to the temperature structure (shown in Fig. 4.2, lower panel). There, we see that the region close to the location of the planet is significantly hotter than the surrounding disk. We show this effect in more detail in Fig. 4.3 where we plotted the temperature map at the disk mid-plane for the 10 $M_\oplus$ planet. For a planet at a larger separation, this effect could be even more pronounced and indirect evidence for the planet (see e.g., Tsukagoshi et al. 2019).

4.5.2 Dust distribution

The different particle sizes modeled encompass a wide range of stopping times. In Figure 4.4 we show the dust surface number density after 100 planetary orbits for three representative sizes and the three planetary masses. In particular, the middle column shows the distribution of pebble-sized particles, which are defined here as particles with a Stokes number of order unity and correspond to meter-sized objects in our setup.

The 5 $M_\oplus$ planet (first row) is not massive enough to open up a gap in the gas and particle disk as seen for the small (coupled) dust in the left column. The only exception is for the planetesimal-sized objects (right column), which do not feel a strong gas drag, and the planetary core can

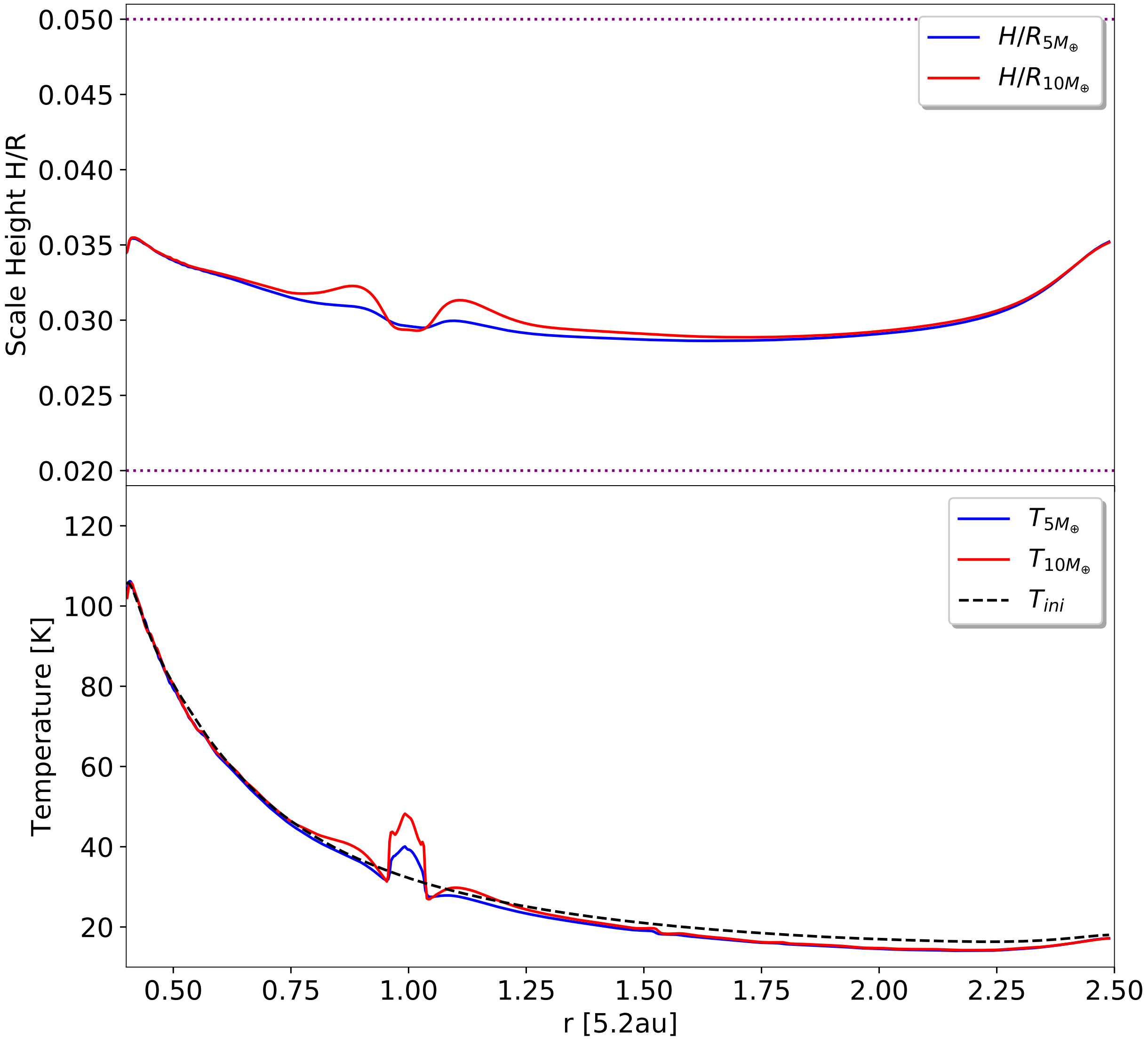

Figure 4.2: *Upper panel*: Disk scale height (H/R, solid lines) as a function of radius for the different planetary masses, $5\,\mathrm{M}_\oplus$ (blue) and $10\,\mathrm{M}_\oplus$ (red), for the models with radiative transfer. The purple dotted lines at 0.05 and 0.02 represent the H/R of the isothermal simulations performed, respectively.
Lower panel: Midplane gas temperature (T, solid lines) for the corresponding models as on the top panel. The black dashed line represents the initial temperature.

gravitationally perturb their orbits, depleting the co-orbital region (Dipierro & Laibe 2017). In the middle row, on the other hand, the $10\,\mathrm{M}_\oplus$ planet has stopped the inflow of pebble-sized particles (middle column), creating an overdensity at the location of the outer pressure bump and a depleted inner disk (Paardekooper & Mellema 2006; Rice et al. 2006; Pinilla et al. 2012a). The $100\,\mathrm{M}_\oplus$ planet is able to carve a deep gap in both the gas and the small particles (last row,

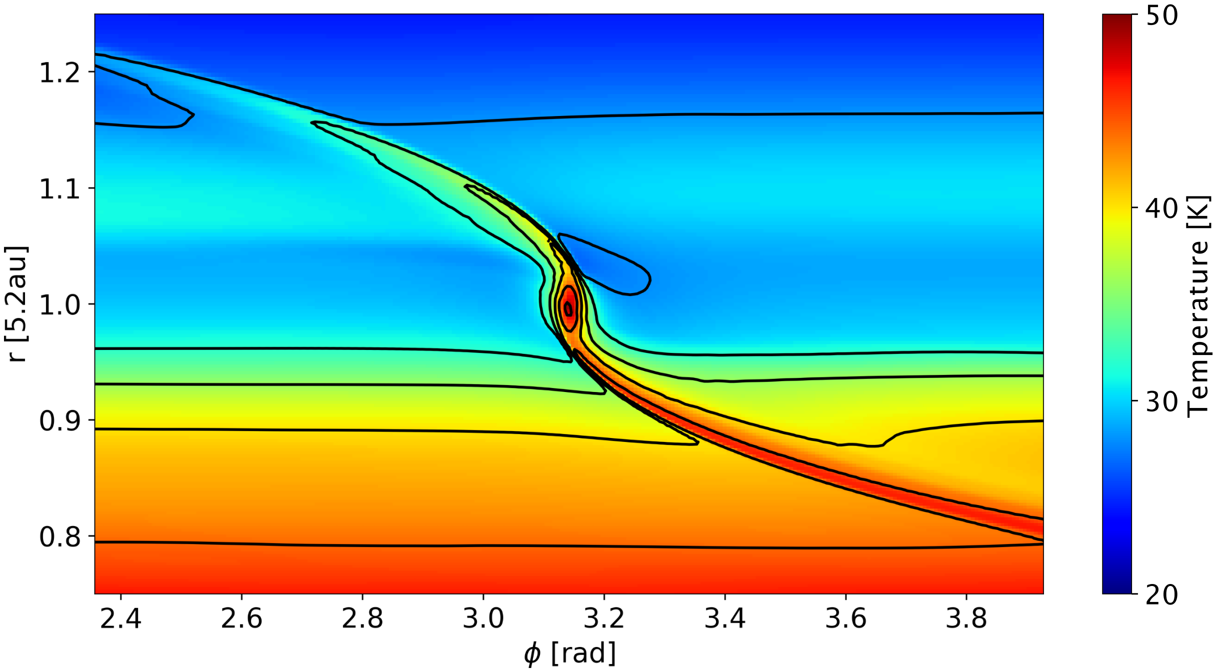

Figure 4.3: Gas temperature map at the disk mid-plane for the $10\,\mathrm{M}_\oplus$ planet. The temperature close to the planet location increases significantly.

first column), where the spiral arms launched by the planet are visible as well. The gap edges also become Rossby wave unstable, generating vortices (Lovelace et al. 1999), as is visible in the larger particle distribution. In the pebble-sized objects (last row, middle column), the distribution of solids shows two concentric rings in the inner side of the planet caused by the perturbance in the gas Keplerian speed by the massive planets, which generates two confined regions where the gas becomes super-Keplerian (see Fig. 4.1).

4.5.3 Dust evolution

In Figure 4.5 we show the temporal evolution of the radial distribution for the same dust particles presented earlier as a function of planetary mass. The plot shows that a quasi-equilibrium state has been obtained for the dust distribution at the end of the simulated period. The $5\,\mathrm{M}_\oplus$ planet (first row) is not able to stop the radial inflow of the well-coupled dust particles (left column), while a small overdensity is building up outside its location for the pebble-sized particles (middle column). On the other hand, a $10\,\mathrm{M}_\oplus$ planet is able to stop the flux of pebble-sized objects efficiently (second row, middle column), thus creating a transition disk where the inner disk is depleted of dust as they are not able to cross the pressure bump created by the planet. The mass at which a planet is able to effectively stop the influx of pebble-sized objects is called pebble isolation mass (see e.g., Morbidelli & Nesvorny 2012). This effect becomes even stronger for the 100 $\mathrm{M}_\oplus$ planet (last row) where already after 60 planetary orbits, the pebble particles (middle column) inside the planet location are only present in two confined regions (as described earlier). In looking at the right column, one can see the strong mass dependence of the gap width for planetesimal-sized objects as well (Ayliffe et al. 2012; Weber et al. 2018).

4.5.4 Solid accretion

The solid accretion rate onto the planetary cores is computed in a post-processing phase using two different criteria, depending on the ratio between their Stokes number and the time they need to cross the planet's Hill sphere (see Picogna et al. 2018, for a detailed description). A sample of particles for each size was chosen outside the planet location and followed for 50 planetary orbits, after which we checked the fraction of accreted and nonaccreted particles (see Fig. 10 of Picogna et al. 2018). Mass is not added to the planet, and even if accreted particles can remain close to the planet or reach a high speed, they do not influence the simulation since the interaction between dust particles and back reaction onto the gas are neglected. We verified that the total solid accretion rate reached a quasi-equilibrium state after 100 planetary orbits when the simulation was stopped.

We can then compute an effective accretion efficiency, P_{eff}, that is, the number of accreted particles onto the planet divided by the number of particles that would otherwise drift across the location of the planet in an unperturbed disk (Ormel & Klahr 2010)

$$P_{\mathrm{eff}} = \frac{\dot{M}_{\mathrm{acc}}}{\dot{M}_{\mathrm{drift}}}, \tag{4.14}$$

where $\dot{M}_{\mathrm{acc}}$ is the measured accretion rate through the criteria explained above, while $\dot{M}_{\mathrm{drift}}$ is the particle drift through the disk $\dot{M}_{\mathrm{drift}} = 2\pi r \Sigma_{\mathrm{p}} v_{\mathrm{drift}}$, where Σ_{p} is the particle surface density and v_{drift} is the unperturbed dust radial drift speed (see e.g., Nakagawa et al. 1986).

In Figure 4.6, we plotted the accretion efficiency for two different planetary masses, 5 $\mathrm{M}_\oplus$ and 10 $\mathrm{M}_\oplus$, and we excluded the 100 $\mathrm{M}_\oplus$ planet because it is capable of carving a gap very quickly, thus strongly depleting the solid accretion for all the studied particle sizes. Again, we compare the radiative case (blue) with two locally isothermal ones with different aspect ratios (red & black). As already pointed out by Picogna et al. (2018), we can only trust the middle part of this plot (in the Stokes number range from 0.1 to 10) because for larger or smaller particles, the planet moves faster than the dust and the accretion efficiency cannot be computed correctly with our method, since the sample of particles outside the planet location chosen for the efficiency calculation is not able to cross its location. Therefore, we highlight the relevant region with a gray color.

For the 5 $\mathrm{M}_\oplus$ planet (Fig. 4.6, left panel), the accretion efficiency in the radiative case (blue line) has a similar steepness but it has increased with respect to the locally isothermal case with $H/R = 0.05$ (red line), by a factor of three to four; whereas, for the case with a lower aspect ratio, the "pebble isolation mass" has already been reached, effectively stopping the inflow of pebble-sized particles. The difference becomes striking for the 10 $\mathrm{M}_\oplus$ planet (Fig. 4.6, right panel). The pebble isolation mass is reached for the radiative case (blue line), and the overall accretion efficiency is reduced. While in the isothermal case with a higher aspect ratio (red line),

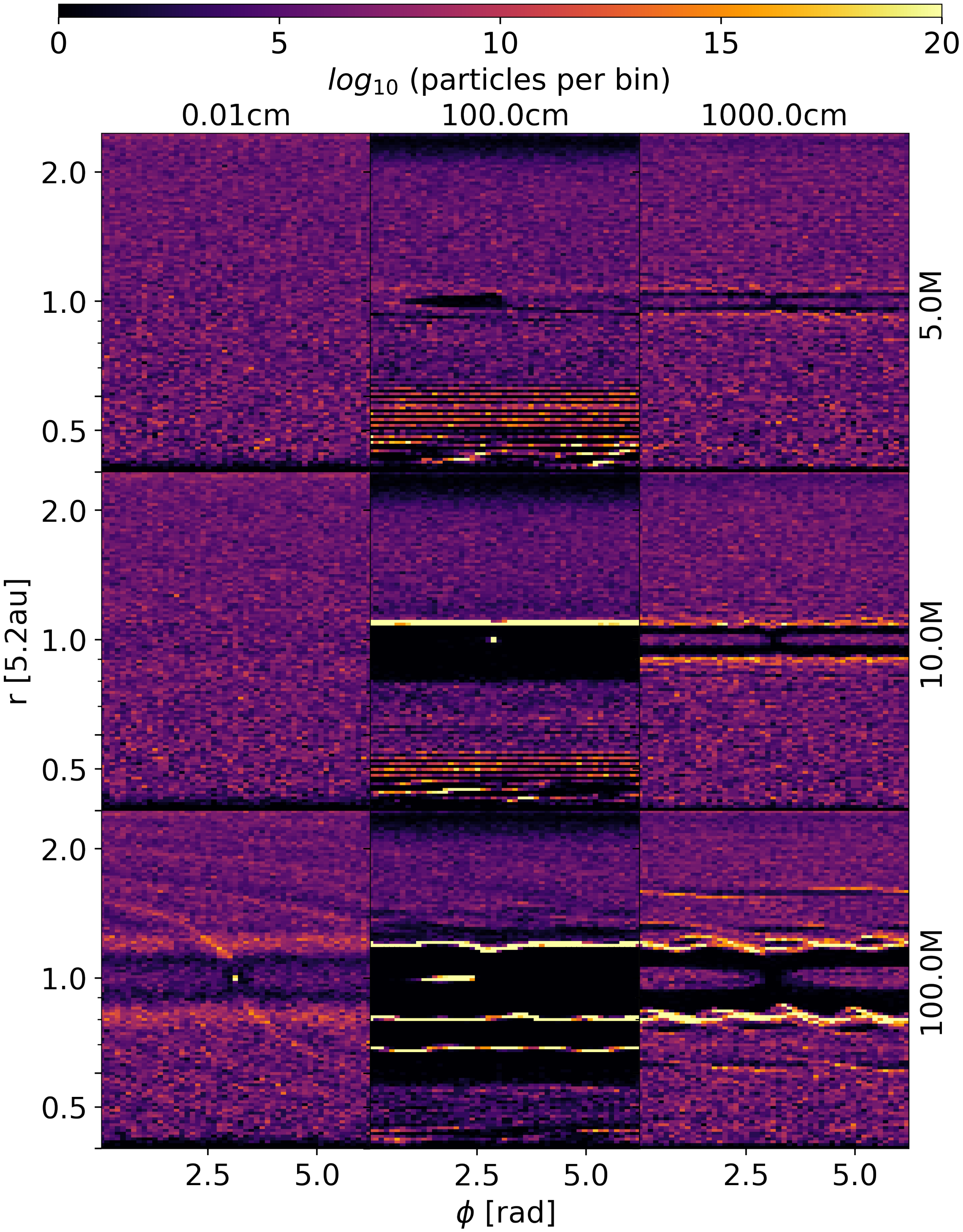

Figure 4.4: Spatial distribution of the dust particles after 100 planetary orbits for the different planetary masses and for three representative particle sizes. The Stokes numbers at the planet location from left to right are, 0.08, 1.23, and 67.2, respectively.

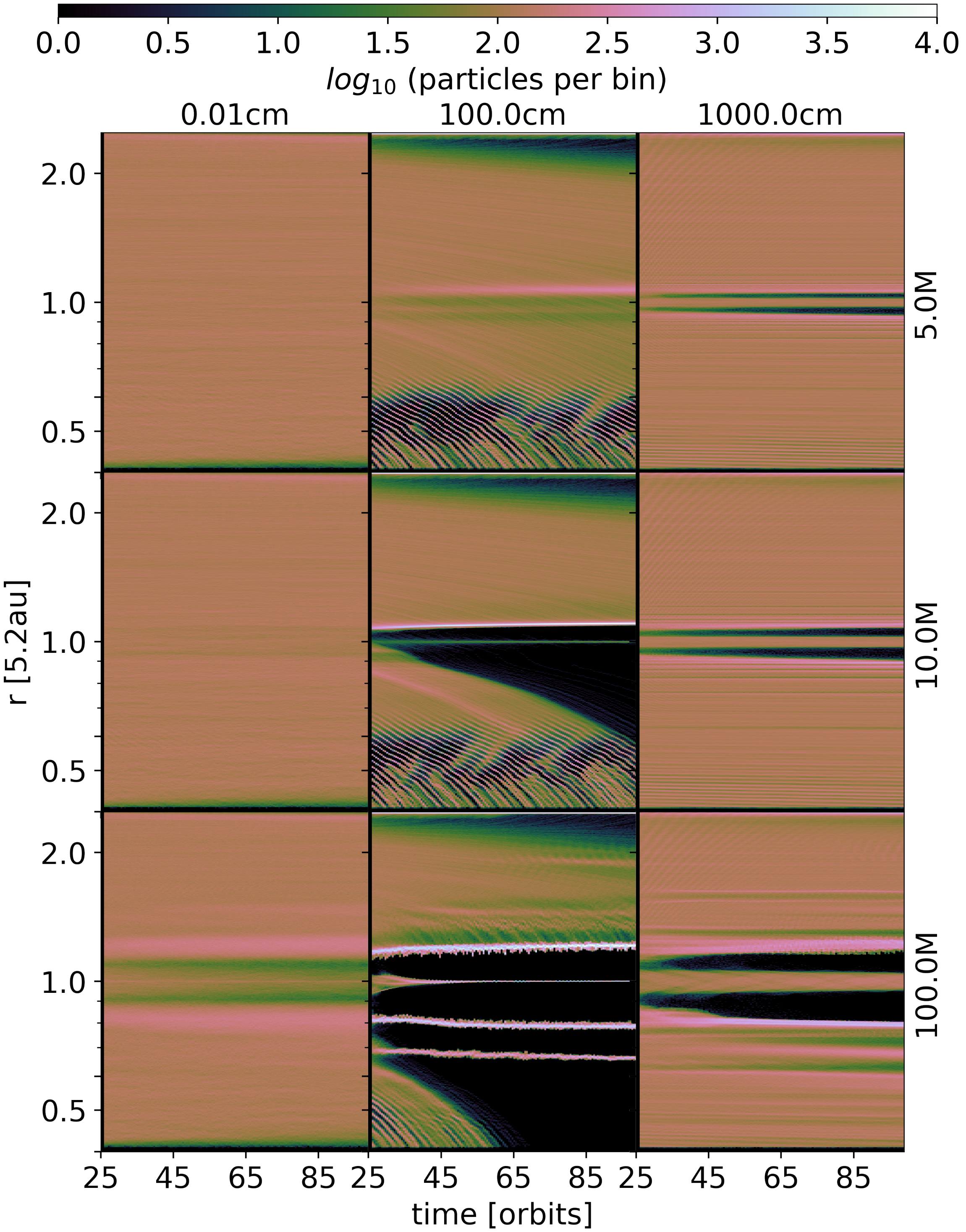

Figure 4.5: Radial distribution (averaged over azimuth) of the dust particles as a function of time for the different planetary masses and for three representative particle sizes. The $10\,M_\oplus$ planet is able to stop the pebbles efficiently, thus creating a transition disk, suggesting that the pebble isolation mass can be less than $10\,M_\oplus$. The Stokes numbers at the planet location from left to right are 0.08, 1.23, and 67.2 after 100 planetary orbits, respectively.

the planet is still accreting pebble-sized objects efficiently. The reason for this difference can be attributed to the change in the disk aspect ratio at equilibrium for the radiative disk compared to the locally isothermal ones (see Fig. 4.2). This effect has been predicted by Bitsch et al. (2018), who found that the pebble isolation mass scales strongly with the disk aspect ratio for a locally isothermal disk

$$M_{\rm iso} \propto \left(\frac{H/R}{0.05}\right)^3 . \tag{4.15}$$

In Figure 4.7 we compare the pebble isolation mass found for our simulations (with error bars given by the bin size in planetary mass used) with the analytical prescription from Bitsch et al. (2018), and we find good agreement when taking the reduced disk scale height at equilibrium for the radiative case into account.

We fit the accretion efficiency with an analytical prescription in the Stokes number range considered, (see green line in Fig. 4.6) as

$$P_{\rm eff} = \frac{3}{\pi\eta}\left(\frac{\tau_s}{0.1}\right)^{-2/3}\left(\frac{r_{\rm H}}{r}\right)^2 \tag{4.16}$$

where $r_{\rm H}$ is the Hill radius, and

$$\eta = -\frac{1}{2}\left(\frac{H}{r}\right)^2 \frac{\partial \ln P}{\partial \ln r} = 8.56 \cdot 10^{-4} \tag{4.17}$$

is the value at 5.2 au in our simulation, just before the planet was included.

This relation is similar to the one obtained by Lambrechts & Johansen (2014, see their eq. 33), but it shows a steeper dependence on the Stokes number τ_s. Their analytical derivation gives a correlation to the Stokes number as $P_{\rm eff} \propto {\tau_s}^{-1/3}$. There are two main reasons to explain why our study yields a steeper relation. First of all, their relation only holds up to $\tau_s = 0.1$. This is because the ratio of the pebble accretion rate (see eq. 28 of Lambrechts & Johansen 2014), given by $\dot{M}_c \propto \tau_s^{2/3}$, and the pebble flux through the planet $\dot{M}_f \propto v_r \propto \frac{\tau_s}{\tau_s^2+1} \simeq \tau_s$ gives this proportionality. However, this last relation breaks down for $\tau_s > 0.1$. In our case, the proportionality of $-2/3$ holds for all of the values of τ_s that are in agreement with our method (τ_s from 0.1 - 1.0, gray area in Fig. 4.6). Furthermore, we are treating a full 3D disk with turbulent kicks on the dust particles, which is difficult to model using an analytic prescription, as in Lambrechts & Johansen (2014). In our 3D simulations, the small particles are lifted to a higher disk scale height compared to the larger particles that settle in the midplane. Hence, the accretion rate increases for smaller dust particles, and a steeper gradient of the efficiency as a function of the particle Stokes number develops.

4.6 Conclusions

We can summarize the main results of this study with the following points.

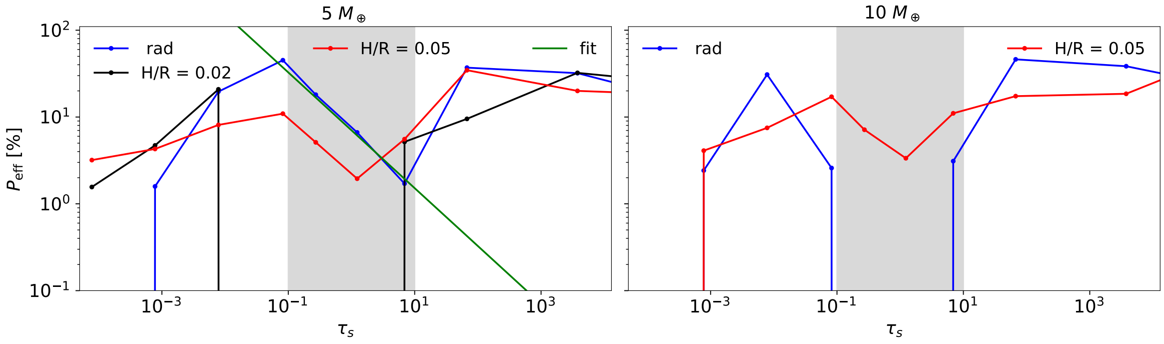

Figure 4.6: Efficiency of accreted particles as a function of Stokes number for different planetary masses. The blue line (rad) refers to the new simulations performed with radiative transfer, the black line corresponds to the isothermal case with $H/R = 0.02$, and the red line ($H/R = 0.05$) represents the isothermal case from Picogna et al. (2018). The fit from eq. 4.16 is over-plotted with a green line. We shaded the intermediate τ_s values in gray for which the method adopted to calculate the efficiency holds (see text).

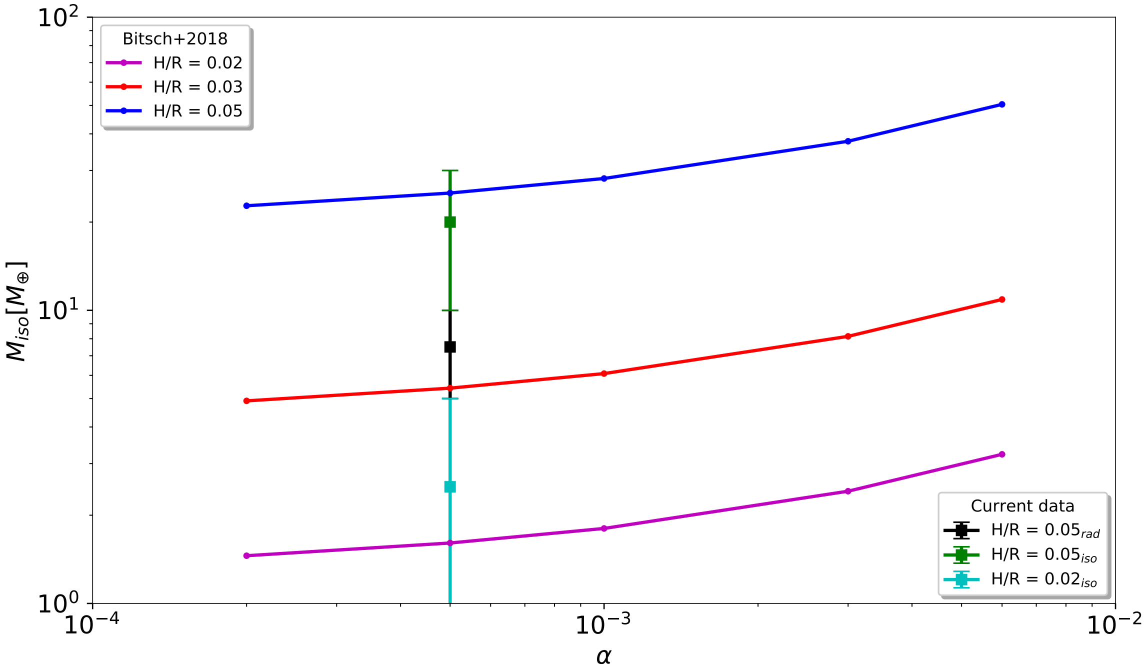

Figure 4.7: Pebble-isolation mass as a function of α and for different aspect ratios H/R. The lines show the pebble isolation mass for different α values and they follow the fit from Bitsch et al. (2018). Squares and error bars correspond to the data from Picogna et al. (2018) and the new models with radiative transfer.

- The main effect of radiative transfer within the bulk of the disk is to produce a cooler and thinner disk (lower H/R, see also Kley et al. (2009)). This allows the growing protoplanet to enhance its efficiency at halting the flux of pebbles and decrease the pebble isolation mass. Since this limit becomes lower than 10 $M_{\oplus}$, which corresponds to the mass at which the core can start its runaway gas accretion, this result can simply explain the observed, relatively low gas giant planet frequency.

- We found a new relation for the pebble efficiency as a function of the particle Stokes number for a 3D disk (see eq. 4.16), where the dependence on the Stokes number is steeper than the one obtained by the analytical derivation of Lambrechts et al. (2014).

- The planetary cores at the end of the disk lifetime would have had time to grow until this limit, which is consistent with the finding that the majority of exoplanets are in the mass range between Earth and Neptune.

- Decreasing the limit of planetary masses that are able to stop the inflow of pebbles from the outer to the inner disk, with respect to the planet location, can help to explain the population of transition disks observed around young stars (with high accretion rates), in a natural way.

The main limitations of this study are the lack of dust back-reaction, particle growth, and irradiation from the central star. Dust coagulation and fragmentation can increase the fraction of solids crossing the planet location by grinding them down at the pressure bump and regrowing them in the inner disk (Drążkowska et al. 2019). Along the same lines, dust back-reaction would modify the pressure gradient outside the planet location, reducing the planet efficiency in stopping the pebble flux (Kanagawa et al. 2018). In this respect, our work, which does not take these two effects into account, underestimates the pebble isolation mass. However, Drążkowska et al. (2019) found that the effect of back-reaction can be strongly reduced when taking a full coagulation model into account. Stellar irradiation is expected to play an important role in modifying the disk aspect ratio and potentially the pebble isolation mass. This effect is, nevertheless, only stronger in the outer, irradiation dominated, disk. We looked in detail to understand the impact of stellar irradiation in Appendix 4.6, confirming that its contribution at the location studied is negligible. We did focus on a planet at 5.2 au where viscous heating is still the main heating term (see e.g., Ziampras et al. 2019), and so our results can be safely generalized to a more complex model.

The fact that our conclusions do not hold for larger radii could imply that giant planets only form in the irradiation dominated region, and the signature of this effect can still be present in the bulk composition of the observed giant planets. Finally, we modeled a laminar viscous disk. It has been shown that, even in magnetically inactive regions, hydrodynamical instabilities can develop (see e.g., Stoll et al. 2017, for the vertical shear instability, VSI). As seen by Stoll & Kley (2016), VSI has a significant effect on reducing the effective viscosity and the disk scale height while increasing the dust vertical spreading. Its effect on solid accretion rates and isolation masses has been studied in the context of locally isothermal disks in Picogna et al. (2018) who found a negligible difference. However, for radiative disks, the damping effect of VSI on the disk scale height can further strengthen our main conclusions.

Appendices

Importance of stellar irradiation

In this work, we ignore the contribution of the stellar irradiation to the disk temperature structure. Since one of our main results is the reduction of the pebble isolation mass due to the decreased disk aspect ratio, we tested our assumption. We performed an extra run (without planet and dust particles) including stellar irradiation (with $T_\star = 5772$ K), until thermal equilibrium was reached at the planet location. As shown in Fig. 4.8, the disk scale height at the planet location is unaffected by the contribution of the stellar irradiation (red line) when comparing it to the run for the $5M_\oplus$ planet (and no stellar irradiation, blue line). On the other hand, this effect plays a major role in an extended disk (see Fig. 4.9).

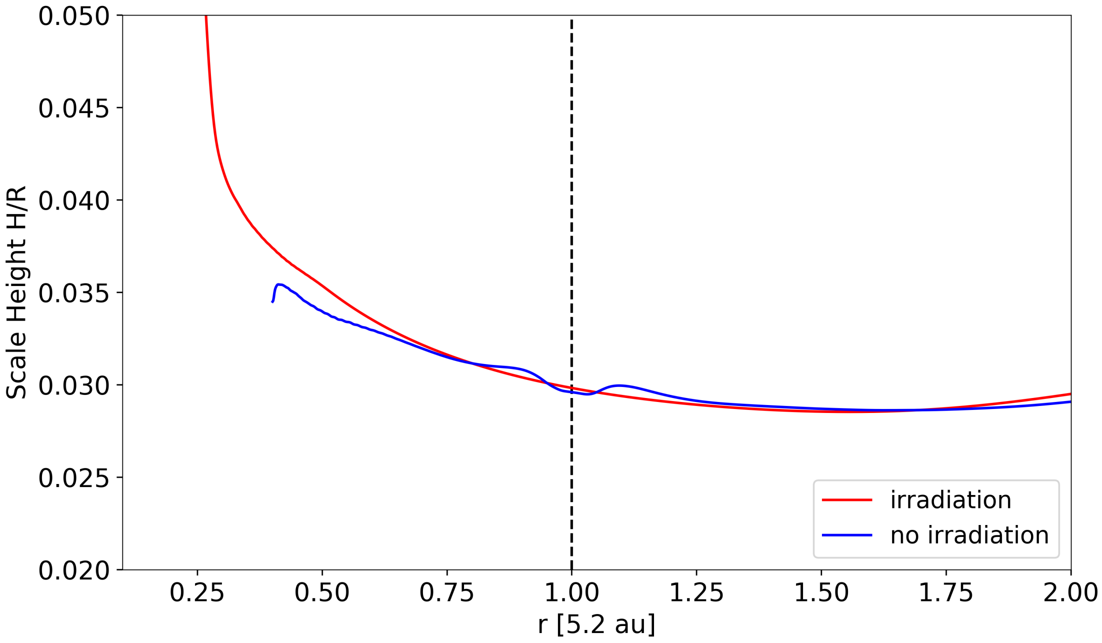

Figure 4.8: Disk scale height for a stellar irradiated disk (red) compared with the disk scale height of the run with a $5M_\oplus$ planet (blue).

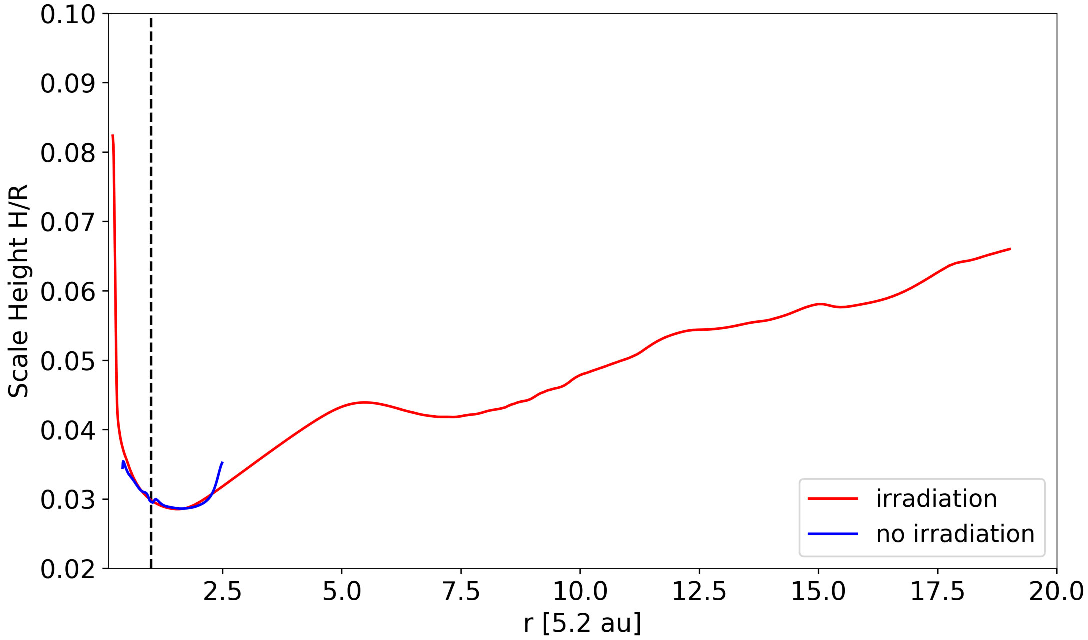

Figure 4.9: Disk scale height for a stellar irradiated disk with a 100 au outer radius (red) compared with the disk scale height of the run with a $5M_{\oplus}$ planet (blue).

Chapter 5

A Large Population Study of Protoplanetary Disks

The contents of this chapter were published in the Astronomy & Astrophysics Journal. Credit: A Large Population Study of Protoplanetary disks - Zormpas et al., A&A 661, A66 (2022), under the Creative Commons Attribution License 4.0.

5.1 Abstract

Recent subarcsecond resolution surveys of the dust continuum emission from nearby protoplanetary disks show a strong correlation between the sizes and luminosities of the disks. We aim to explain the origin of the (sub-)millimeter size-luminosity relation (SLR) between the 68% effective radius (r_{eff}) of disks with their continuum luminosity (L_{mm}), with models of gas and dust evolution in a simple viscous accretion disk and radiative transfer calculations.

We use a large grid of models (10^5 simulations) with and without planetary gaps, and vary the initial conditions of the key parameters. We calculate the disk continuum emission and the effective radius for all models as a function of time. By selecting those simulations that continuously follow the SLR, we can derive constraints on the input parameters of the models.

We confirm previous results that models of smooth disks in the radial drift regime are compatible with the observed SLR ($L_{\mathrm{mm}} \propto r_{\mathrm{eff}}^2$), but only smooth disks cannot be the reality. We show that the SLR is more widely populated if planets are present. However, they tend to follow a different relation than smooth disks, potentially implying that a mixture of smooth and substructured disks are present in the observed sample. We derive a SLR ($L_{\mathrm{mm}} \propto r_{\mathrm{eff}}^{5/4}$) for disks with strong substructure. To be compatible with the SLR, models need to have an initially high disk mass ($\geq 2.5 \cdot 10^{-2} M_\star$) and low turbulence-parameter α values ($\leq 10^{-3}$). Furthermore, we find that the grain composition and porosity drastically affects the evolution of disks in the size-luminosity diagram where relatively compact grains that include amorphous carbon are favored. Moreover, a uniformly optically thick disk with high albedo (0.9) that follows the SLR cannot be formed from an evolutionary procedure.

5.2 Introduction

Planet formation is a process far from having a complete, robust, and widely accepted theory. Multiple theories aim to explore the way planets form (e.g., Benz et al. 2014; Kratter & Lodato 2016; Johansen & Lambrechts 2017). To understand planet formation, high resolution observations and large surveys of the birth places of planets, the protoplanetary disks (PPDs), are essential. In recent years the Atacama Large Millimeter/Submillimeter Array (ALMA) has not only provided a sizable number of highly resolved observations of PPDs, but due to its high sensitivity it has also enabled several large intermediate resolution (on the order of 100 mas) surveys of different star-forming regions (for a review see Andrews 2020, and references therein) providing crucial information on population properties such as distributions of disk sizes, fluxes, or spectral indices for disks across stars of different masses and ages and across star-forming regions in different environments.

Highly resolved observations and large intermediate resolution surveys are complementary and are both essential for understanding the connections between key properties of PPDs. One of the important diagnostics is the continuum luminosity (L_{mm}) at (sub-)millimeter wavelengths since it can be a tracer of the disk mass that is produced by the solid grains (Beckwith et al. 1990) (i.e., the amount of material available to form planets). Assuming a constant dust-to-gas ratio (usually 0.01 based on observations of the interstellar medium, see Bohlin et al. 1978), the dust mass can be converted to the total disk mass (dust and gas). Surveys that measure the disk dust mass (M_{dust}) have been used to correlate this property with the mass of the host star ($M_{\star}$), and a linear relation has been found between them (Andrews et al. 2013) that appears to steepen with time (Pascucci et al. 2016; Ansdell et al. 2017; Barenfeld et al. 2016). Furthermore, a steeper than linear relationship has been observed between L_{mm} and $M_{\star}$ (Andrews et al. 2013; Pascucci et al. 2016; Ansdell et al. 2016). Recently, theoretical studies have started to explain these correlations (e.g., Pascucci et al. 2016; Stammler et al. 2019; Pinilla et al. 2020) using numerical dust evolution models that include grain growth, radial drift, fragmentation of dust particles, and particle traps (e.g., Birnstiel et al. 2010, 2012; Krijt et al. 2016).

These observations of dust thermal continuum emission are crucial for the characterization of disk evolution. However, the methods described above that relate dust emission to physical quantities like total disk masses carry uncertainty arising from the multiple assumptions such as the dust opacity and the disk temperature that may vary for every disk (e.g., Hendler et al. 2017; Ballering & Eisner 2019). The grain opacity depends on the unknown particle size distribution, composition, and particle structure (e.g., Birnstiel et al. 2018, and references within), although considerable efforts have been undertaken from modeling (e.g., Wada et al. 2008, 2009; Okuzumi et al. 2009; Seizinger & Kley 2013; Seizinger et al. 2013) and experimental studies (e.g., Blum & Wurm 2008; Güttler et al. 2010b; Gundlach & Blum 2015) of aggregation and of the computation of optical properties of aggregates (e.g., Kataoka et al. 2014; Min et al. 2016; Tazaki et al. 2016).

Another important property for the characterization of a disk population is the disk size. Viscous theory (Lynden-Bell & Pringle 1974b) predicts that a fraction of the disk mass keeps moving outward, known as viscous spreading, suggesting the disk size should increase with time. In principle a measurement of disk size as a function of time could measure this evolution to test viscous theory and measure its efficiency. The most readily available tracer of the disk size is the continuum as gas tracers suffer from uncertain abundances (due to freeze-out and dissociation, among others) and sensitivity constraints. Since the disk does not have a clear outer edge, we need to introduce an effective radius and express the size as a function of the total continuum emission. This size metric is called emission size or effective radius (r_{eff}) (Tripathi et al. 2017).

However, the dust component does not behave in the same way as the gas mainly due to an effect termed radial drift (e.g., Whipple 1972; Weidenschilling 1977; Takeuchi & Lin 2002). The dust particles interact with the sub-Keplerian gas disk via aerodynamic drag forces, leading them to migrate toward the star. As an observational implication, the dust emission is less extended than the gas emission (e.g., Andrews et al. 2012; Isella et al. 2012; Andrews et al. 2016; Cleeves et al. 2016) predicted by Birnstiel & Andrews (2014) (but see Trapman et al. 2020). Radial drift is also heavily dependent on the grain size; therefore, grain growth (e.g., Birnstiel et al. 2012) has to be included in the numerical studies that aim to use the dust disk radius. Rosotti et al. (2019b) studied theoretically how the evolution of the disk dust radius changes with time in a viscously evolving disk and addressed whether the evolution of the dust disk radius is set by viscous spreading or by the dust processes such as grain growth and radial drift. They found that viscous spreading influences the dust and leads to the dust disk expanding with time.

Many surveys have been performed to explore the relation between the two diagnostics (e.g., Andrews et al. 2010; Piétu et al. 2014; Hendler et al. 2020). Recently, a subarcsecond resolution survey of 50 nearby protoplanetary disks, conducted with the Submillimeter Array (SMA) by Tripathi et al. (2017), showed a strong size-luminosity relation (SLR) between the observed population. The follow-up program in Andrews et al. (2018a), a combined analysis of the Tripathi et al. (2017) data and the ALMA data from the Lupus disk sample (105 disks in total), confirmed the scaling relations between the r_{eff} and the L_{mm}, $M_{\star}$. However, not all studied star-forming regions show the same correlation, but appear to vary with the age of the region (Hendler et al. 2020).

In recent years, due to the unprecedented sensitivity and resolution, ALMA has provided a plethora of groundbreaking images of protoplanetary disks. Most of these disks do not show a smooth and monotonically decreasing surface density profile, but instead are composed of single or multiple symmetric annular substructures, for example HL Tauri (ALMA Partnership et al. 2015), TW Hya (Andrews et al. 2016; Tsukagoshi et al. 2016), HD 163296 (Isella et al. 2016), HD 169142 (Fedele et al. 2017), AS 209 (Fedele et al. 2018), HD 142527 (Casassus et al. 2013), and many more in the recent DSHARP survey (Andrews et al. 2018b). Moreover, non-axisymmetric features like spiral arms (e.g., Pérez et al. 2016b; Huang et al. 2018b) and lopsided rings (e.g., van der Marel et al. 2013) have been observed.

Many ideas for the origin of these ring-like substructures have been explored but one of the most favorable explanations is the formation of gaps in the gas surface density, due to the presence of planets. A massive planet ($\geq 0.1 M_{jup}$) (Zhang et al. 2018) is able to open a gap in the surrounding gaseous disk, thereby generating a pressure maximum. Later on, the dust particles migrate toward the local pressure bump, due to radial drift (Weidenschilling 1977; Nakagawa et al. 1986), and consequently lead to the annular shape (e.g., Rice et al. 2006; Pinilla et al. 2012a). These narrow rings may be optically thick or moderately optically thick, but between these features the material is approximated as optically thin (Dullemond et al. 2018). However, these rings can contain large amounts of dust that can increase the total luminosity of a disk and its position with respect to the SLR.

The SLR might contain crucial information about disk evolution and planet formation theory. Our goal is to explore the physical origins of the SLR from Tripathi et al. (2017) and Andrews et al. (2018a) by performing a large population study of models with gas and dust evolution. We aim to characterize the key properties of disks that reproduce the observational results. We explore the differences in the SLR of disks that have a smooth surface density profile and disks that contain weak and strong substructures. In Section 5.3, we discuss the methods we used to carry out our computational models. The results of this analysis are presented in Section 5.4, where we explain the global effect of every parameter in the population of disks and we present the general properties that disks should have to follow the SLR. In Section 5.5 we discuss the theoretical and observational implications of our results. We draw our conclusions in Section 5.6.

5.3 Methods

We carry out 1D gas and dust evolution simulations using a slightly modified version of the two-population model (two-pop-py) by Birnstiel et al. (2012, 2015), while we also mimic the presence of planets. As a post-processing step, we calculate the intensity profile and the disk continuum emission. With the purpose of running a population study, we use a large grid of parameters (see Table 5.1), so that we can explore the differences that occur due to the different initial conditions. In the next sections, we explain the procedure in more detail.

5.3.1 Disk evolution

The gas follows the viscous evolution equation. For the disk evolution, we use the turbulent effective viscosity as in Shakura & Sunyaev (1973),

$$\nu = \alpha_{\mathrm{gas}} \frac{c_s^2}{\Omega_K} , \tag{5.1}$$

and the dust diffusion coefficient as

$$D = \alpha_{\mathrm{dust}} \frac{c_s^2}{\Omega_K} , \tag{5.2}$$

with α_{gas} being the turbulence parameter, c_s the sound speed, and Ω_K the Keplerian frequency. The above equation lacks the term $\frac{1}{1+\mathrm{St}^2}$, where St is the Stokes number, but we can ignore it since the Stokes number is always < 1 in our simulations (Youdin & Lithwick 2007). We differentiate the α parameter in two different values. One for the gas α_{gas} and one for the dust α_{dust}, since we later mimic planetary gaps by locally varying the viscosity (see Section 5.3.3). In the smooth case $\alpha_{\mathrm{dust}} = \alpha_{\mathrm{gas}}$.

The dust is described by the two populations model of Birnstiel et al. (2012) which evolves the dust surface density under the assumption that the small dust is tightly coupled to the gas while the large particles can decouple from the gas and drift inward. The initial dust growth phase is using the current dust-to-gas ratio instead of the initial value as in Birnstiel et al. (2012).

We set the initial gas surface density according to the self-similar solution of Lynden-Bell & Pringle (1974b),

$$\Sigma_g(r) = \Sigma_0 \left(\frac{r}{r_c}\right)^{-\gamma} \mathrm{Exp}\left[-\left(\frac{r}{r_c}\right)^{2-\gamma}\right], \tag{5.3}$$

where $\Sigma_0 = (2-\gamma)M_d/2\pi r_c^2$ is the normalization parameter, which is set in every simulation by the disk mass M_d. The other parameters are $\gamma = 1$, which is the viscosity exponent and it is not varied throughout our models and r_c which is the characteristic radius of the disk (see Table 5.1). When $r \ll r_c$, then Σ_g is a power law and when $r \geq r_c$, Σ_g is dominated by the exponential factor.

The initial dust distribution follows the gas distribution with a constant dust-to-gas ratio of Σ_d/Σ_g=0.01. The initial grain size (= monomer grain size) is $a_{\min} = 0.1\,\mu$m. This monomer size stays constant in time and space, while the representative size for the large grains increases with time as the particles grow. The particle bulk density is $\rho_s = 1.7\,\mathrm{g/cm^3}$ for the standard opacity model from Ricci et al. (2010) and $\rho_s = 1.675\,\mathrm{g/cm^3}$ for the DSHARP (Birnstiel et al. 2018) opacity, but decreases for different values of porosity (see Section 5.3.4). We evolve the disks up to 10 Myr to study the long-term evolution, but in the following analysis we only show results from 300 kyr to 3 Myr (see Section 5.3.5).

Our 1D radial grid ranges from 0.05 to 2000 au and the grid cells are spaced logarithmically. We use adaptive temperature, which depends on the luminosity of every star. Since the stellar mass changes in our grid, the stellar luminosity changes as well. We follow the temperature profile,

$$T = \left(\phi \frac{L_\star}{4\pi\sigma_{SB} r^2} + (10\,\mathrm{K})^4\right)^{1/4}, \tag{5.4}$$

as in Kenyon et al. (1996). In this equation $L_\star$ is the stellar luminosity, $\phi = 0.05$ is the flaring angle, σ_{SB} is the Stefan-Boltzmann constant, and r is the radius. The term 10^4 is a lower limit so that we do not allow the disk temperature to drop below 10 K at the outer parts of the disk. We use the evolutionary tracks of Siess et al. (2000) to get the luminosity of a 1 Myr old star of the given mass. The stellar luminosity and effective temperature is not evolved in our simulations. However, the luminosity of a $1\,M_\odot$ star would decrease from $\sim 2.4\,L_\odot$ at 1 Myr to $\sim 1\,L_\odot$ at 3 Myr. In Section 5.5.8 we explore how a change in stellar luminosity affects our results.

5.3.2 Population study

We use an extended parameter grid, by varying the initial values of the turbulence parameter (α_{gas}), disk mass (M_d), stellar mass ($M_\star$), characteristic radius (r_c), and fragmentation velocity (v_{frag}). For every parameter, we pick the ten values specified in Table 5.2, taking all the possible combinations between them leading to a total of 100.000 simulations.

5.3.3 Planets

A large planet embedded in a disk produces a co-orbital gap in the gas density. To mimic gap opening by planets in our simulations, we altered the α_{gas} turbulence parameter. Since in steady

Table 5.1: Grid parameters of the model

Parameter	Description	Value-Range
$\Sigma_{\mathrm{d}}/\Sigma_{\mathrm{g}}$	initial dust-to-gas ratio	0.01
ρ_{s} [g/cm^3]	particle bulk density	1.7, 1.675
γ	viscosity exponent	1
r [au]	logarithmic grid extent	0.05 – 2000
$\mathrm{n_r}$ [cells]	grid resolution	400
t [years]	duration of each simulation	10^7

Table 5.2: Variables of the model

Parameter	Description	Values
α	viscosity parameter	$\{1, 2.5, 5, 7.5\} \cdot 10^{-4}$ $\{1, 2.5, 5, 7.5\} \cdot 10^{-3}$ $\{1, 2.5\} \cdot 10^{-2}$
$\mathrm{M_d}$ [$\mathrm{M_\star}$]	initial disk mass	$\{1, 2.5, 5, 7.5\} \cdot 10^{-3}$ $\{1, 2.5, 5, 7.5\} \cdot 10^{-2}$ $\{1, 2.5\} \cdot 10^{-1}$
$\mathrm{M_\star}$ [$\mathrm{M_\odot}$]	stellar mass	$0.2, 0.4, 0.6, 0.8, 1.0$ $1.2, 1.4, 1.6, 1.8, 2.0$
r_{c} [au]	characteristic radius	$10, 30, 50, 80, 100$ $130, 150, 180, 200, 230$
$\mathrm{v_f}$ [cm/s]	fragmentation velocity	$200, 400, 600, 800, 1000$ $1200, 1400, 1600, 1800, 2000$
q	planet/star mass ratio	$3 \cdot 10^{-4}$, 10^{-3}, $3 \cdot 10^{-3}$
r_p [r_c]	planet position	$1/3$, $2/3$

state $\alpha_{\mathrm{gas}} \cdot \Sigma_{\mathrm{g}}$ is constant, the α parameter and the surface density Σ_{g} are inversely proportional quantities, so a bump in the α_{gas} profile leads to a gap in the surface density profile. The reason for the change in α_{gas} and not in Σ_{g} is that the surface density evolves according to Eq. 5.3. By inserting the bump in the α_{gas}, the Σ_{g} still evolves viscously and at the same time produces a planetary gap shape.

Following the prescription from Kanagawa et al. (2016), we mimic the effect of planets with different planet/star mass ratios q (see Table 5.1). For reference, $q = 10^{-3}$ represents a Jupiter-mass planet around a solar-mass star. This way, we can study the effect of planetary gaps and rings in the observable properties of the disk and extract the key observables in a computationally efficient way, avoiding the need to run expensive hydrodynamic simulations for each combination of parameters.

Choosing the appropriate profile that mimics a planetary gap is tricky, so we performed hydrodynamical simulations using FARGO-3D (Benítez Llambay & Masset 2015), and we compared the effect on the observable quantities. The Kanagawa et al. (2016) profile is an analytical approximation of the gap depth and width, but does not necessarily represent the pressure bump that is caused by the bump. Therefore, we tested how strongly this assumption affects the properties of the dust in the trap by comparing them against proper hydrodynamical solutions and disk evolution. We found that the depth of the gap is not as important to the evolution of the disk on the SLR, but the width is the dominant factor. As long as the planet is massive enough to create a strong pressure maximum and thus stop the particles, the position of the pressure maximum is more important than a precise value of the gap depth. In summary, the gap depth is not what matters the most but the associated amplitude and location of the pressure maximum. We should mention that the precise amount of trapping in the bumps should still matter, for example in planetesimal formation, but for our results this is less relevant. We provide comparison plots and more details in Section A.3.

We define the position of the planets in the disk $\mathrm{r_p}$, as a function of the characteristic radius r_c (see Table 5.1). We locate them either at $2/3$ or at $1/3$ of r_c. In our simulations we used zero, one, or two planets in these positions. We refer the reader to Section 5.4.1 for the effect of the planet location and mass in the simulations.

5.3.4 Observables

Since the disk size is not one of the parameters that we measure directly, using the characteristic radius r_c as a size metric is problematic (Rosotti et al. 2019b). For this reason we define an observed disk radius using the calculated surface brightness profile. Following Tripathi et al. (2017) we adopt their approach to defining an effective radius ($\mathrm{r_{eff}}$) as the radius that encloses a fixed fraction of the total flux, $\mathrm{f}_\nu\ (\mathrm{r_{eff}}) = \mathrm{xF}_\nu$. We choose x = 68% of the total disk flux as a suitable intermediate value to define $\mathrm{r_{eff}}$ as it is comparable to a standard deviation in the approximation of a Gaussian profile.

We calculate the mean intensity J_ν profile by using the scattering solution from Miyake & Nakagawa (1993) of the radiative transfer equation

$$\frac{J_\nu(\tau_\nu)}{B_\nu(T(r))} = 1 - b\left(e^{-\sqrt{3\epsilon_\nu^{eff}}\left(\frac{1}{2}\Delta\tau - \tau_\nu\right)} + e^{-\sqrt{3\epsilon_\nu^{eff}}\left(\frac{1}{2}\Delta\tau + \tau_\nu\right)}\right), \tag{5.5}$$

with

$$b = \left[\left(1 - \sqrt{\epsilon_\nu^{eff}}\right) e^{-\sqrt{3\epsilon_\nu^{eff}}\Delta\tau} + 1 + \sqrt{\epsilon_\nu^{eff}}\right]^{-1}, \tag{5.6}$$

where B_ν is the Planck function and

$$\tau_\nu = \left(\kappa_\nu^{\mathrm{abs}} + \kappa_\nu^{\mathrm{sca,eff}}\right)\Sigma_d \tag{5.7}$$

is the optical depth with $\kappa_\nu^{\rm abs}$ the dust absorption opacity and $\kappa_\nu^{\rm sca,eff}$ the effective scattering opacity, which is obtained from Ricci et al. (2010) or Birnstiel et al. (2018) (see below). As effective scattering opacity we refer to

$$\kappa_\nu^{\rm sca,eff} = (1 - g_\nu)\kappa_\nu^{sca}, \tag{5.8}$$

where g_ν is the forward-scattering parameter, $\Delta\tau$ is

$$\Delta\tau = \Sigma_{\rm d}\kappa_\nu^{\rm tot}\Delta {\rm z}, \tag{5.9}$$

while

$$\epsilon_\nu^{eff} = \frac{\kappa_\nu^{abs}}{\kappa_\nu^{abs} + \kappa_\nu^{sca,eff}} \tag{5.10}$$

is the effective absorption probability. To calculate the intensity $I_\nu^{\rm out}$ we follow the modified Eddington-Barbier approximation as in Birnstiel et al. (2018),

$$I_\nu^{out} \simeq \left(1 - e^{-\Delta\tau/\mu}\right) S_\nu\left(\left(\frac{1}{2}\Delta\tau - \tau_\nu\right)/\mu = 2/3\right), \tag{5.11}$$

where $\mu = \cos\theta$ and

$$S_\nu(\tau_\nu) = \epsilon_\nu^{eff} B_\nu(T_d) + (1 - \epsilon_\nu^{eff}) J_\nu(\tau_\nu) \tag{5.12}$$

is the source function.

Two-pop-py evolves only the dust and gas surface densities and the maximum particle size,[1] thereby implicitly assuming a particle size distribution. The grain size at each radius is set by either the maximum size possible in the fragmentation- or drift-limited regimes, whichever is lower (see Birnstiel et al. 2012, for details). To compute the optical properties of the dust, we therefore considered a population of grains with a power-law size distribution, $n(a) \propto a^{-q}$, with an exponent $q = 2.5$, for $a_{\rm min} \leq a \leq a_{\rm max}$. This choice follows Birnstiel et al. (2012) where the size distribution is closer to $q = 2.5$ for disks that are in the drift limit, while for the fragmentation-limited ones, a choice of $q = 3.5$ would be more suitable. Considering the disk mass is dominated by the large grains, the choice of a smaller exponent does not alter our results significantly, but it matters for the details. Since the smooth simulations are mostly drift-limited the choice of $q = 2.5$ fits these disks better. Moreover, if a disk is fragmentation-limited then it is so mostly in the inner part, but the bulk of the disk that defines the luminosity is in the outer part. Therefore, the luminosity will still depend mainly on the drift-limited regime. The disks with substructures can be fragmentation-limited farther out in the formed rings, but considering that these rings are mostly optically thick, the difference between exponents is much smaller than for the smooth disks.

The grain composition consists of 10% silicates, 30% carbonaceous materials, and 60% water ice by volume. For a direct comparison with observations (Tripathi et al. 2017; Andrews et al. 2018a), we calculate the opacity in band 7 (i.e., at 850 μm). Afterward, we use the absorption opacity to calculate the continuum intensity profile.

---

[1] In the rest of the manuscript we refer to grain size or particle size rather than maximum grain size.

We also examined the effect of different opacity models and different grain porosities. As a base model we used the composition from the Ricci et al. (2010) opacities (hereafter denoted R10-0), but for compact grains (i.e., without porosity) as in the model of Rosotti et al. (2019a). Furthermore, we used the DSHARP opacity model (Birnstiel et al. 2018) and we altered the grain porosity to 10% (little porous, DSHARP-10), 50% (semi-porous, DSHARP-50), and 90% (very porous, DSHARP-90). The particle bulk densities for the different porous grains are $\rho_s = 1.508\,\mathrm{g/cm^3}$, $\rho_s = 0.838\,\mathrm{g/cm^3}$, and $\rho_s = 0.168\,\mathrm{g/cm^3}$, respectively. An important feature of the opacity models that we used is called the *opacity cliff*, which refers to the sharp drop in the opacity at 850 μm, at a maximum particle size around 0.1 mm, as defined in Rosotti et al. (2019a) (see Figure 5.1). In all the figures that are shown in this paper the R10-0 opacity model from Ricci et al. (2010) is used, unless it is explicitly stated otherwise.

5.3.5 Matching simulations

The behavior of the simulations on the size-luminosity diagram ($\mathrm{L_{mm}} - \mathrm{r_{eff}}$ plane, hereafter *SL Diagram*) depends on the time evolution of disks. According to Andrews et al. (2018a), the linear regression of the joint data between Tripathi et al. (2017) and Andrews et al. (2018a) gives a relation between the disk size and the 340 GHz luminosity. The effective radius $\mathrm{r_{eff}}$ and the luminosity $\mathrm{L_{mm}}$ are correlated as

$$\log \mathrm{r_{eff}} = (2.10^{+0.06}_{-0.03}) + (0.49^{+0.05}_{-0.03}) \log \mathrm{L_{mm}}\,, \tag{5.13}$$

with a Gaussian scatter perpendicular to that scaling with a standard deviation (1σ) of $0.20^{+0.02}_{-0.01}$ dex (where $\mathrm{r_{eff}}$ is in au and $\mathrm{L_{mm}}$ is in Jy at a distance of 140 pc).

In Figure 5.2 (top left) we show an evolution track. It is the path that the simulations follow on the luminosity-radius diagram in a chosen time span. They move from the top right (higher luminosity and radius) to the bottom left as the disk evolves. We plot the evolution track from 300 kyr to 3 Myr. The thought behind this is that at roughly 300 kyr our disks reach a quasi-steady state. Specifically, the drift speed in the drift limit is $\mathrm{V_r} = \epsilon \mathrm{V_K}$, with ϵ being the dust-to-gas ratio and $\mathrm{V_k}$ the Keplerian velocity. So after at least one order of magnitude is lost in the dust, the evolutionary time becomes too long. We refer the reader to Section 5.5, where we show the evolution of disk dust-to-gas ratio as a function of time for different cases. Longer evolutionary times than we are exploring here do not alter our results significantly, and are not included to simplify the discussion. They will be included as a topic of future research since at later stages disks are more strongly affected by dispersal. Moreover, our chosen time span covers the observed disks from the Andrews et al. (2018a) and Tripathi et al. (2017) joint sample.

In order to filter our simulations, we divided them in categories. A simulation that lies within 1σ (blue shaded region in Figure 5.2, top left, of the SLR) (Eq. 5.13) at all times in our chosen time span is considered matching (see Figure 5.2, green evolution track). On the other hand, if at any time a simulation does not lie within the area, it is considered *discrepant*. The *discrepant* simulations can be further divided into two subcategories. One that is above the SLR (see Figure 5.2, purple and yellow tracks, top left) and one below (red track). With this classification we can identify the main parameters that drive a simulation to be located in a certain spot on the

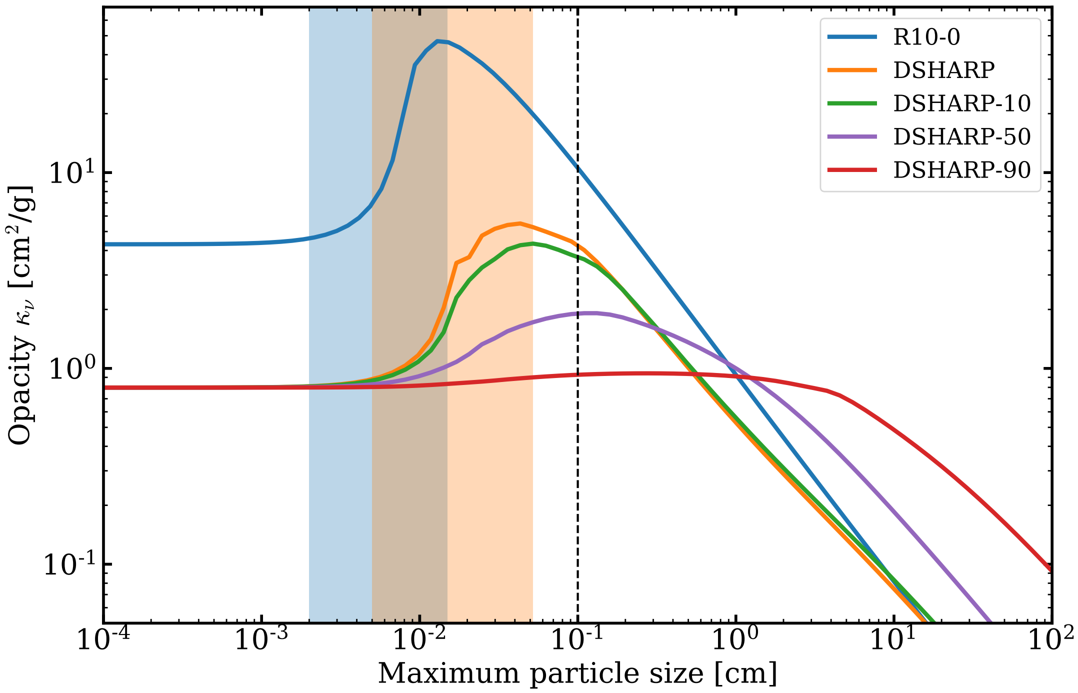

Figure 5.1: Comparison between the opacity models that we used at 850 μm as a function of the maximum particle size and for a power-law size distribution with an exponent of q = 2.5. Shown is the *opacity cliff* (see text for details) at a wavelength of 850 μm (blue and orange shaded regions). The blue line refers to the opacity model from Ricci et al. (2010) with compact grains (labeled R10-0) and the orange line to that of Birnstiel et al. (2018) with compact grains (labeled DSHARP). The green, purple, and red lines refer to 10%, 50%, and 90% porous grains in the DSHARP model. The R10-0 and DSHARP opacity values differ by a factor of ~ 8.5 at the position of the opacity cliff. As the porosity of the DSHARP model increases, the opacity cliff starts to flatten out, until it completely disappears for very porous grains (90%). The location of the cliff shifts to larger particle sizes as it diminishes in porosity. The black dashed line shows the particle size at 1 mm. The value for the R10-0 model at this size corresponds to $\kappa_\nu^{\mathrm{R10-0}} = 9.8\,\mathrm{cm}^2/\mathrm{g}$, while for the DSHARP to $\kappa_\nu^{\mathrm{DSHARP}} = 4\,\mathrm{cm}^2/\mathrm{g}$.

SL Diagram. It is worth mentioning that a fraction (~ 32%) of the observational data points lie outside the 1σ region by definition. This highlights that the definition of the matching simulations is conservative with respect to the observational data.

Later on we define the term *matching fraction* as the percentage of the matching simulations against the total number of simulations performed with a certain initial condition (see Section 5.4.1).

5.4 Results

In this section we present the main results of this analysis. In Section 5.4.1 we explain the effect of every parameter on the path of the disk in the SL diagram. In Section 5.4.2 we present the general properties that disks should have to follow the SLR, and we derive a theoretical SLR for disk with substructures in Section 5.4.2. In Section A.2 we present an additional analysis for the results discussed below.

5.4.1 Evolution tracks

In Section 5.3.5 we explain what an evolution track is, while we show some examples in Figure 5.2 (top left). Every track is affected by the initial conditions of the parameters chosen, and by the presence or not of a planet. In the following sections we explore the effect of the most important parameters of our grid model and we show how every parameter affects the evolution track on the SL Diagram in Figure 5.2, Figure 5.3, and Figure 5.4.

Since the grid consists of 100.000 simulations, single evolution tracks do not show the preferred initial conditions that allow a simulation to stay in the SLR, but only a representative case. In order to identify trends between the initial conditions and the matching fraction of every disk, we constructed histograms where on the y-axis we have the matching fraction (i.e., the percentage of simulations that stay on the SLR for the chosen time span) and on the x-axis we have the value of each parameter in our grid model. Different colors represent different simulation grids, with or without planets and with varying the planetary mass or positions (e.g., Figure 5.5). In black we show the simulations where we used a smooth surface density profile, as in Rosotti et al. (2019a). In green we show the case where the planet/star mass ratio is $q = 1 \cdot 10^{-3}$ at a location of 1/3 of the r_c (inner planet), in red the same planet at a distance of 2/3 of the r_c (outer planet), and in blue two planets of $q = 1 \cdot 10^{-3}$ at $1/3 r_c$ and $2/3 r_c$. The white hatched bars show the same cases, but using a different opacity model DSHARP (Birnstiel et al. 2018).

Effect of planetary parameters

In a smooth disk, the evolution track evolves toward smaller radii and lower luminosity as the dust drifts inward, so the emission (and size) decreases. Moreover, the opacity cliff moves farther in as the radius in the disk where the maximum particle size a_{max} is (i.e., the value for the peak opacity) decreases, due to radial drift and grain growth, as in Rosotti et al. (2019b).

In contrast, in the case where a planet is present the pressure bump that is formed stops the dust from drifting toward the host star, delaying the evolution of the disk on the SL Diagram, thus keeping the tracks on the SLR for longer times. With this in mind, we expect a less extended evolution track when we include planets, since planets are included early in the disk evolution. In Figure 5.2 (top right), we show an example of the evolution tracks of a disk with the same initial conditions, varying only the presence and the position of a planet. The red line represents the evolution track of a disk with a smooth surface density profile. If we include a planet with planet/star mass ratio $q = 10^{-3}$, Jupiter mass in this case, at a location that is close to the characteristic radius of the disk, in this case at 2/3 of the r_c, we see from the green line (number

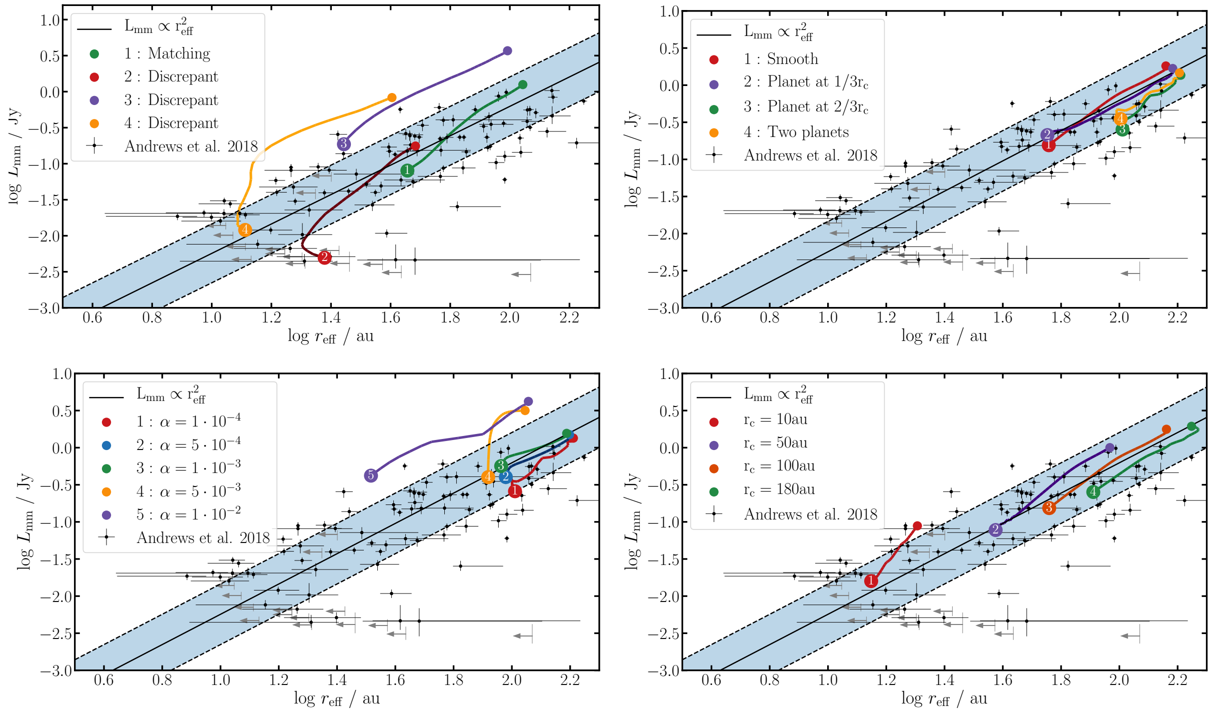

Figure 5.2: Evolution tracks and explanation of matching and discrepant simulations. Examples of a disk with the same initial conditions varying only one parameter at a time. **Top left**: SLR according to Andrews et al. (2018a) and examples of evolution tracks. The black points correspond to the observational data, and the black dashed line is Eq. 5.13, which shows the relation between the luminosity and the effective radius. Finally, the blue shaded region is the area within 1σ of the SLR where the simulations are considered to be *matching*. The green track labeled number 1 is considered a *matching* simulation since it starts and ends inside the SLR. The other tracks are considered *discrepant*. The beginning of the track is where the empty bullet is (top right) and the end is where the number is found (bottom left). **Top right**: Varying only the presence and the position of a Jupiter-mass planet. The red line (number 1) is for a smooth disk and the green line (number 3) for a disk with a Jupiter-mass planet at 2/3 of the r_c; the purple line (number 2) corresponds to a planet at 1/3 of the r_c and the yellow line (number 4) to a simulation with two planets at the positions mentioned above. **Bottom left**: Varying only the turbulence parameter α. Higher α values lead to higher luminosity. **Bottom right**: Varying only the characteristic radius r_c. Higher r_c values lead to larger and more luminous disks.

3) that both the effective radius and the luminosity increase relative to the planet-less case, and the evolution track is shorter at the same time span as in all planet cases. This is clear since the pressure bump is trapping particles and the dust mass is retained. Therefore, the luminosity does not decrease as quickly. At the same time, the fixed position of the pressure bump causes the effective radius to remain the same. Together this means that the track in the SLR comes to a halt.

On the other hand, if we place the planet close to the star, in this case at 1/3 of the r_c, we observe a much longer track similar to the one with the smooth profile (purple line). The size and the luminosity of the disk change only slightly. The smaller radius compared to the case where we have an outer planet is explained because the dust now stops at the inner pressure bump and the luminosity is roughly the same for the two cases. This could lead to the conclusion that a planet close to the star will not affect dramatically its position on the SL Diagram, but this is not true for all cases (see Section 5.4.1). Instead, the evolution track here is similar to the smooth one because the disk is too large and massive and the inner planet cannot affect the evolution track too much.

As a last point, we included two planets, one at the 2/3 of the r_c and one at 1/3. We observe a similar evolution track as in the case where we have only one planet close to the outer radius, with the disk being slightly more luminous. This is also explained by the fact that the dust from the outer disk stops at the outer pressure bump, while the dust that exists inside the outer planet stops at the pressure bump of the inner planet. Since most of the dust mass initially resides outside the outer planet, the dust that is trapped between the two planets contributes only partially to the total luminosity. When two or more planets are present the location of the outermost planet is more dominant in the evolution track.

Effect of the turbulence α-parameter

The effect of the turbulence parameter α on the evolution track is straightforward: higher α leads to higher luminosity. In Figure 5.2 (bottom left) we show the evolution tracks of a disk with the same initial conditions, varying only the α-parameter. In this case, we choose a disk where we have also inserted a Jupiter mass planet at the 2/3 of the characteristic radius (r_c) since the effect is more prominent on these disks.

To understand the trends in Figure 5.2 (bottom left), it is instructive to consider Figure 5.3, where we show an example of how different α-values affect the efficiency of trapping. In the top panel we show the dust mass local flow rate $\mathrm{M}_{\mathrm{acc,d}}(\mathrm{r})$ $[\mathrm{M}_\oplus/\mathrm{yr}]$ as a function of radius. For low α-values $1 \cdot 10^{-4}$ (red line), $5 \cdot 10^{-4}$ (blue), and $1 \cdot 10^{-3}$ (green), the mass flows toward the bump and the local flow rate for $\mathrm{r} < \mathrm{r_p}$ is low ($\leq 10^{-8}\mathrm{M}_\oplus/\mathrm{yr}$), meaning that the trapping is efficient enough to stop the dust from drifting toward the star. On the other hand, for the high α-values $5 \cdot 10^{-3}$ (yellow) and $1 \cdot 10^{-2}$ (purple), the dust mass local flow rate stays almost constant ($\leq 10^{-5}\mathrm{M}_\oplus/\mathrm{yr}$) throughout the whole disk, meaning that the bump does not trap the particles, just locally slows them down. In the bottom panel we show the cumulative mass of the disk integrated from inside out as a function of radius. For the low α-values, most of the mass is located in the bump, while for $\alpha = 5 \cdot 10^{-3}$ and $\alpha = 1 \cdot 10^{-2}$ it increases with the radius, meaning that the bump allows more grains to escape and therefore it does not contain a significant fraction of the disk mass.

Returning to Figure 5.2 (bottom left), disks with low to medium α-values (10^{-4}, $5 \cdot 10^{-4}$, 10^{-3}) are less luminous than disks with higher α-values. This is so because the ring that is formed due to the pressure bump is becoming too narrow and optically thick. The total flux emitted by an optically thick ring of a given temperature is just a function of the emitting area. Lower α will lead to a narrower ring (Dullemond et al. 2018), and thus less emitting area and therefore lower luminosity, independently of the amount of mass in the ring. On the other hand, high α-values work against trapping in various ways, leading to more luminous disks. A higher α-value decreases the particle size in the fragmentation limit, which are less efficiently trapped by radial drift (e.g., Zhu et al. 2012). It increases the diffusivity, which allows more grains to escape the bump and it increases the viscosity in the same way, so more dust sizes are traveling with the accreting gas. Furthermore it smears out the pressure peak, causing less efficient trapping by radial drift (Pinilla et al. 2012b). Moreover, with high α-values a higher dust-to-gas ratio is retained because grain growth is impeded by fragmentation, hence radial drift is much slower.

If we consider the two cases where the α-value is high ($5 \cdot 10^{-3}$, 10^{-2}), the planet cannot efficiently trap the dust and the disk evolves farther along the SLR to lower luminosities. A disk that contains a planet with $\alpha = 10^{-2}$ behaves the same as a smooth disk without a planet on the SL Diagram, implying that in this case a very massive planet (several Jupiter masses) would be needed to significantly affect disk evolution. This results in the dust grains becoming smaller since the gas turbulent velocity is increasing and the collisions between them are more destructive. Consequently, the gap is becoming shallower while there is also more diffusion.

In Figure 5.5 (top left), we show the dependence of the α-viscosity parameter on the matching fraction. As expected, all simulations tend to favor low values of the turbulence parameter $10^{-4} \leq \alpha \leq 10^{-3}$. Smooth simulations show a clear tendency toward low α-values because when they are drift dominated they remain in the SLR. On the other hand substructured disks show a preference toward $5 \cdot 10^{-4} \leq \alpha \leq 10^{-3}$. The dust trapping is efficient enough and allows the disks to retain their mass, but while moving to higher α-values $\alpha > 2.5 \cdot 10^{-3}$, the trapping stops being efficient and leads to higher chances that the evolution track will leave the SLR in the selected time span. If $\alpha < 5 \cdot 10^{-4}$ the dust rings become narrow and the luminosity is not large enough to place them in the SLR, and therefore the matching fraction decreases.

Effect of the characteristic radius r_c

In Figure 5.2 (bottom right), we plot the evolution tracks of a smooth disk with the same initial conditions while varying only the characteristic radius ($r_c = 10$ au, 50 au and 100 au, and 180 au). The same trend applies to disks where a planet is included, but for a smooth disk the evolution tracks are longer and the effect is more easily visible. The effect of the characteristic radius on the evolution tracks is straightforward. The larger the r_c the more the evolution track moves toward the top right of the plot, meaning that for a larger disk we expect higher luminosity. In more detail, increasing the characteristic radius (going from the red to green line) explains why the effective radius increases, while the luminosity increases because the total disk mass remains fixed on all these simulations. This result is consistent with the SLR from Andrews et al. (2018a).

Taking a look at Figure 5.5 (middle left), we do not observe a continuous pattern as in the other histograms. Smooth disks do not seem to depend on the characteristic radius as disks of

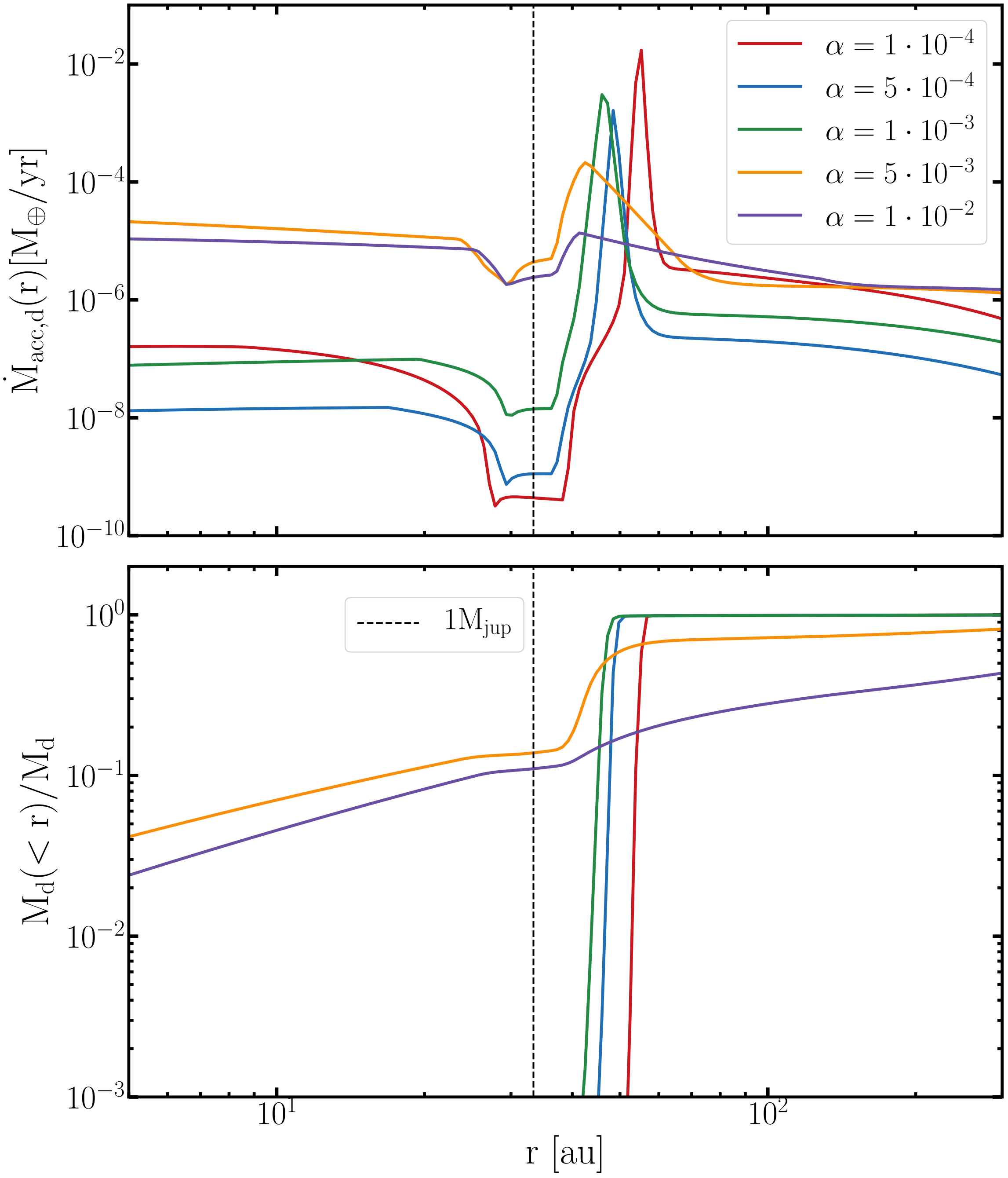

Figure 5.3: **Top panel**: Local flow rate of the dust mass in $M_\oplus$/year as a function of radius for a disk with a Jupiter mass planet at 31 au. For the low α-values $1 \cdot 10^{-4}$ (red line), $5 \cdot 10^{-4}$ (blue) and $1 \cdot 10^{-3}$ (green), we observe that the bump outside the planet location is large enough to hold the dust from drifting toward the star, while for larger α-values $5 \cdot 10^{-3}$ (yellow), 10^{-2} (purple), there is only a weak accumulation outside the planetary gap.
Bottom panel: Cumulative dust mass contained within a radius r, as function of radius. For α-values $1 \cdot 10^{-4}, 5 \cdot 10^{-4}, 1 \cdot 10^{-3}$, roughly all the mass of the disk is inside the bump that is created from the planet. For larger α-values $5 \cdot 10^{-3}, 1 \cdot 10^{-2}$, the bump is minimal and not able to hold the dust from drifting.

all sizes can reproduce the SLR. On the other hand, substructured disks with small r_c (10 au) are mostly above the correlation because they have high luminosity relative to their size (as explained by our size-luminosity estimate in Section 5.5.3) and they are unable to enter the correlation in time. For large radii (> 150 au) the disks can become too large but with low luminosity, and can end up below the correlation to the very right part of the SL diagram (see Figure 5.6).

Therefore, we observe a peak toward a specific characteristic radius, around $80 - 130$ au when a planet is at a location of 1/3 of the r_c and around $30 - 80$ au for the case where a planet is at a location of 2/3 of the r_c. The inner planet constrains the disk to a small size but with relatively high luminosity, therefore placing it above the SLR before 300 kyr, while the opposite effect occurs when an outer planet exists. When two planets are included we observe a mixed situation of the single cases. The reason is that the two pressure bumps compete with each other and each contributes in one of the ways described above.

Effect of the disk mass - M_d

In Figure 5.4 (top left) we plot the evolution tracks of a smooth disk with the same initial conditions varying only the disk mass (M_d). We choose a smooth disk to show the effect more clearly, but the same principle applies to most disks.

The disk mass contributes to both luminosity and radius. Higher disk masses lead to higher luminosities, both at the beginning and at the end of the track. Since for a fixed r_c, disks with higher M_d have higher L_{mm}, it is only logical that more material will lead to higher luminosity and vice versa. By the end of the evolution tracks, the less massive disks have left the SLR. The dramatic curvature of the SLR for the lowest M_d case ($M_d = 5 \cdot 10^{-3} M_\star$) occurs because all grain sizes become smaller than the opacity cliff. If we choose a disk that contains a planet, the massive disks ($M_d \geq 5 \cdot 10^{-2} M_\star$) will still evolve toward lower radii and luminosities on the SLR, but the less massive ones will have shorter tracks. The pressure bump will trap all the material outside of the planet position, so the emission and the effective radius will both remain almost constant. The only case where the track of a low mass disk can be long is if the planet mass is small and the pressure bump is not large enough to retain dust.

In Figure 5.5 (top right) we plot the matching fraction of the disk mass values. The tendency here is that higher disk mass leads to more simulation inside the SLR. The reason for this is that high initial disk mass places the disks above the SLR until they reach a stable state. While the dust is drifting toward the host star the luminosity decreases, allowing them in our chosen time span to reach the SLR and stay there for the remaining time. Since most of the dust is in the trap at this point, the remaining evolution time is set by the trap life time.

The difference is noticeable between the smooth and the planet(s) cases. As we see from the yellow bars, a disk with a smooth surface density profile must be initially massive ($M_d \geq 0.025\, M_\star$) to remain in the SLR. The probability of a smooth simulation to match is even greater than the cases where a planet is included.

Some of these results though are an effect of the opacity model used and the chosen time span, as we discuss in Section 5.4.1.

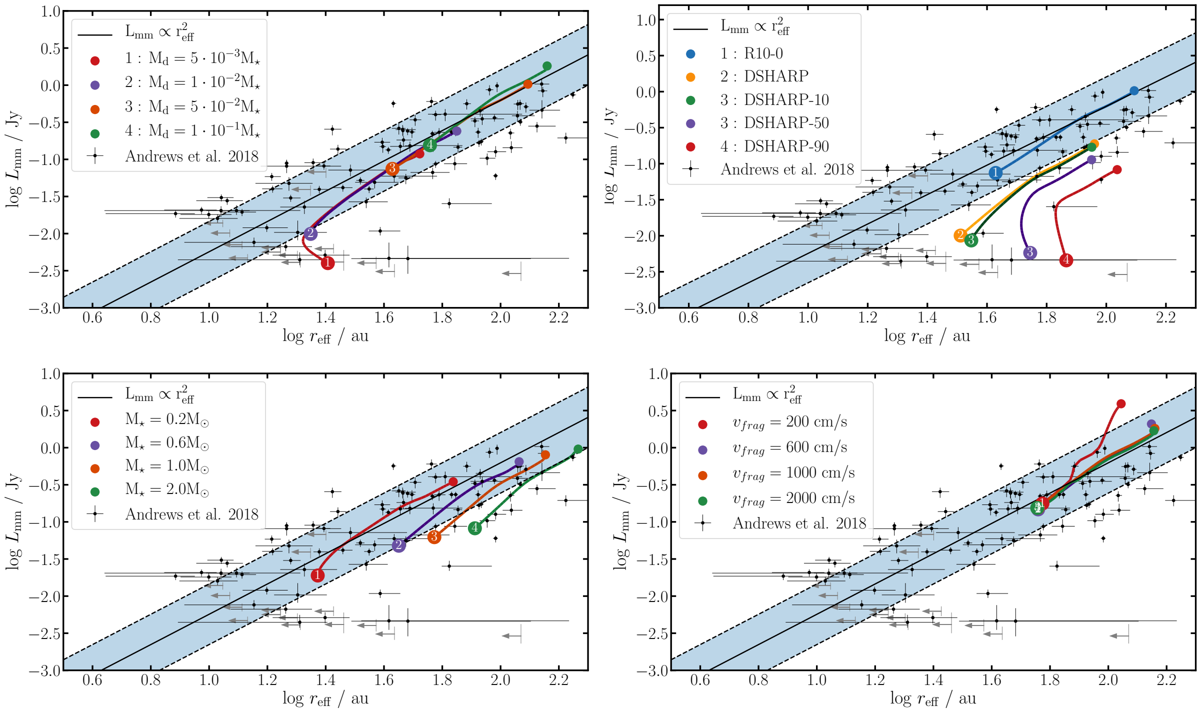

Figure 5.4: Evolution tracks with the same initial conditions varying only one parameter at a time. **Top left**: Varying the disk mass of a smooth disk. **Top right**: Varying the different opacity models and the porosity of the DSHARP model of a smooth disk. **Bottom left**: Varying the stellar mass of a disk that contains a planet. **Bottom right**: Varying the fragmentation velocity of a smooth disk.

Effect of different opacity and grain porosity

In Figure 5.4 (top right) we represent the behavior of several similar tracks varying only the opacity model. The simulations with the Ricci et al. (2010) opacity model (R10-0, blue line) produce more luminous and larger disks than those with the DSHARP model (orange line) due to the higher value of the opacity. The R10-0 opacity is 8.5 times higher than the DSHARP at the peak of the opacity cliff. If we use slightly porous grains (DSHARP-10, green line) by altering the DSHARP opacity, we observe that the effect is insignificant as the shape of the opacity is roughly the same. On the contrary, for semi-porous and very porous grains (DSHARP-50 and DSHARP-90, purple and red line, respectively) the opacity cliff starts to flatten out (Kataoka et al. 2014), leading to a disk with low luminosity and no significant change in disk size.

In all the histogram figures (Figure 5.5) the same trend stands for either the opacity from R10-0 (solid color bars) or DSHARP (Birnstiel et al. 2018) (hatched bars). The difference is that more simulations match when the R10-0 opacity model is used as opposed to the DSHARP model. Disks with the DSHARP opacity are generally less bright because they do not become optically thick in the rings and end up below the SLR. Therefore, it would need more dust (i.e., stronger traps) for them to be luminous enough. Especially for the smooth case (yellow bars), there are only a few simulations that match, hence the hatched bars are barely visible. For smooth disks the total matching fraction is 29.6% with the R10-0 opacity, while it is 0.8% with the DSHARP value. For disks with an inner planet the matching fractions are 30.2% and 15.9%, respectively (see Section 5.5.3, where we explore the overall impact of porous grains for the entire grid of models).

Effect of the stellar mass - $M_\star$

In our models the stellar mass is assumed to be directly correlated with the disk mass because we varied the stellar mass, but we always kept the disk-to-star mass ratio constant. Therefore, a higher star mass implies a higher total mass of the dust, leading to higher continuum luminosities.

In Figure 5.4 (bottom left) we plot the evolution tracks of a disk that contains a planet with the same initial conditions, varying only the stellar mass for $0.2\,M_\odot$, $0.6\,M_\odot$, $1.0\,M_\odot$, and $2.0\,M_\odot$. As expected, the highest value of $M_\star = 2.0M_\odot$ leads to the largest and most luminous disk (green line), while the opposite is true for $M_\star = 0.2M_\odot$ (red line). There is similar behavior for smooth disks, but in that case the radius of each disk is much smaller due to radial drift.

Furthermore, the stellar mass is the least important parameter when defining whether a simulation matches. The histogram in Figure 5.5 (middle right) confirms this. Even though the trend shows that using higher stellar mass has a greater matching fraction, this occurs because the stellar mass scales to the disk mass, and higher disk mass leads to more matching simulations (see Section 5.4.1).

This scaling implies that the luminosity (L_{mm}) scales with the stellar mass ($M_\star$). Our models follow a relation that is not as steep as the observed $L_{mm} \propto M_\star^{1.5}$ in Andrews et al. (2018a), because there is not a correlation between disk size and stellar mass in our simulations (see Section 5.5.5 and Figure 5.10 where we explore further this relation).

Effect of the fragmentation velocity - v_{frag}

In Figure 5.4 (bottom right) we plot the evolution tracks, of a smooth disk with the same initial conditions, varying only the fragmentation velocity for values of 200 cm/s, 600 cm/s, 1000 cm/s, and 2000 cm/s. We observe that for medium and high values of v_{frag} (in this case for $v_{frag} \geq 600$ cm/s), the evolution tracks overlap. Since most of our simulations are drift-limited we expect that no effect from the fragmentation velocity will take place for these values since particles do not grow big enough to drift, so more mass remains at large radii to produce more emission. Therefore, this effect only arises when the fragmentation velocity becomes too low, which leads to a higher luminosity in the first snapshots.

Moreover, if a disk is fragmentation-limited then it is so mostly in the inner part. Therefore, considering that the main bulk of the disk is in the outer part, the emission that defines the luminosity will still depend on the drift-limited regime hence leading to the overlapping tracks. The effect of a planet in these tracks is minimal and we expect a similar behavior to the case shown here.

This can be validated in Figure 5.5 (bottom left), where we plot the matching fraction compared to the fragmentation velocity and the tendency is to higher fragmentation velocities for all cases.

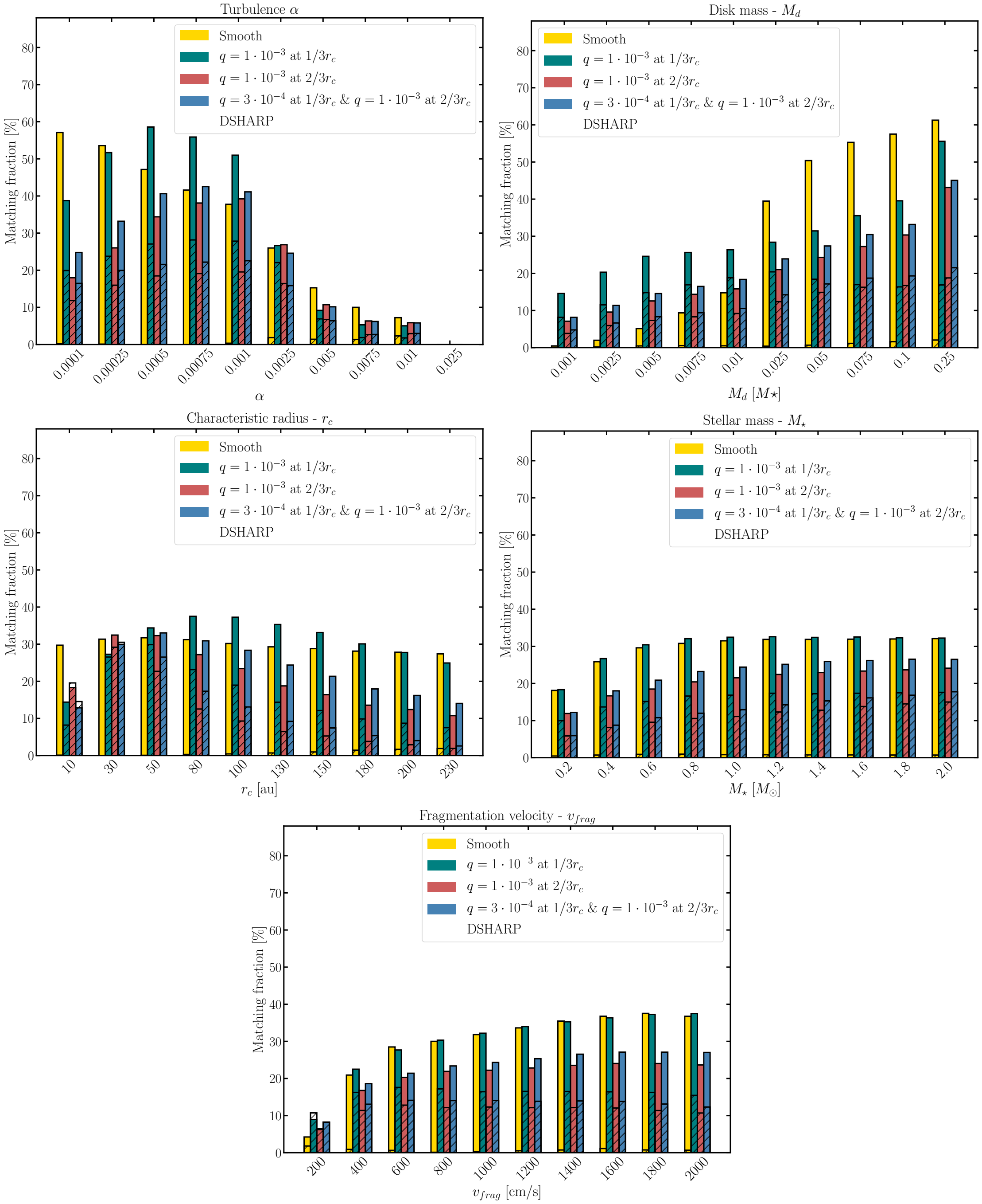

Figure 5.5: Histograms of the matching fraction for disk mass, characteristic radius, stellar mass, and fragmentation velocity. The matching fraction shows the percentage of the simulations that remained on the SLR for the chosen time span (300 kyr – 3 Myr). **Top left**: Dependence on the α-value. There is a preference to low α-values ($10^{-4} \leq \alpha \leq 10^{-3}$). **Top right**: Dependence on the disk mass. There is a preference to high disk masses ($0.025 \leq \mathrm{M_d}/\mathrm{M}_\star \leq 0.25$).
Middle left: Dependence on the characteristic radius. Smooth disks do not depend on the r_c.
Middle right: Dependence on the stellar mass. There is a slight preference to higher values.
Bottom left: Dependence on the fragmentation velocity. There is a slight preference to higher values.

More specifically, if $v_{frag} \geq 600$cm/s, there is a large number of matching simulations and it only gets larger with increasing fragmentation velocity. In this range the simulations are mostly drift-limited. For low values of v_{frag}, most of the simulations are fragmentation-limited and they lose luminosity relatively quickly, moving them out of the SLR. Low values of v_{frag} lead to smaller particles and less efficient trapping. Therefore, those disks lose their solids too quickly. This is analyzed in more detail in Section A.2.

For reference, in a recent lab experiment (Blum 2018b), $100\,\mathrm{cm/s} \leq v_{frag} \leq 1000\,\mathrm{cm/s}$ is considered a value consistent with lab work and $v_{frag} > 1000\,\mathrm{cm/s}$ a high fragmentation velocity.

5.4.2 Heat maps

Single evolution tracks give us an idea of how a single simulation evolves on the SLR, but with a large sample of simulations like the one we have it is not easy to extract global results. Since there are too many tracks to plot all of them in a single diagram, we treat the position of every simulation at every snapshot as an independent sample, and we plot them on a heat map. In these figures we plot the position of every simulation for a specific case (smooth and planet in different locations), for three different snapshots (300 kyr, 1 Myr, 3 Myr).

In Figure 5.6 we plot three different cases. In Col. 1 we show the smooth case, in the Col. 2 the case where we use a planet/star mass ratio $q = 10^{-3}$ at 1/3 of the r_c, and in the last column $q = 10^{-3}$ at 2/3 of the r_c. The snapshots are at three times as shown, as are the SLR and the standard deviation. The red line is our prediction for the cases where we include a planet (see Section 5.4.2). Instead of following the relation from Andrews et al. (2018a), they seem to follow a relation of $L_{mm} \propto r_{eff}^{5/4}$. In Section 5.4.2 and Section 5.4.2 we perform a more detailed analysis on the this topic.

We observe that most of the disks start inside and above the correlation (first row at 300 kyr). In the smooth case the disks lose a great deal of their luminosity relatively quickly and also shrink in size, making them move to the lower radii due to radial drift. We end up with a large number (29.6%) of simulations occupying and following the SLR. As we explain in Section 5.4.2, the slope is expected from Rosotti et al. (2019a), but the normalization depends on the choice of opacities.

On the other hand, when we include a planet and the time increases the disks do not decrease in size, but mainly in luminosity. This is due to the formation of the pressure bump that keeps the dust from drifting farther in, thus keeping the same effective radius. The consequence is that if the disks leave the SLR, it is due to luminosity decrease since they move vertically in the diagram. The clustering in r_{eff} that is formed in the plots with a planet are an artifact of our parameter grid. A randomly chosen value of r_c and planet position would result in a continuous (non-clustered) distribution. From the comparison of the two cases where a planet is included, there are more matching simulations when a planet is in the inner part of the disk (30.2%). Having a planet in the outer part leads the disks to the right (large radii) and bottom part of the diagram and consequently leaves them outside of the relation (20.6% of the disks match).

The difference becomes striking when we use the dust opacities from DSHARP in Figure 5.7. Since the DSHARP opacity is lower than the R10-0 (see Figure 5.1), many of the smooth disks start below the SLR. This leads the majority of them outside of the relation by the last snapshot (3 Myr) and only (0.8%) of the disks match. The same stands for the case where a planet is included. The disks have lower luminosity in the first snapshot, but the pressure bump formed is big enough to keep them in the relation for the remaining time (> 11.1%) of the disks match depending on the model.

A similar behavior for the cases where we include strong substructures is seen for the opacity model with semi-porous grains, DSHARP-50, in Figure 5.8. Even though there are fewer matching simulations in total, if the substructures are large enough, they are able to keep a significant number of simulations in the clusters on the SLR (> 10.7%). The same argument cannot be made for simulations with the smooth surface density profile. With semi-porous grains there is only a small fraction of matching simulations (0.7%). The absence of a strong opacity cliff in the opacity profile leads to low luminosities and consequently all the simulations below the SLR. An almost identical point is true looking at the heat map (Figure A.8) for the case where very porous grains are used (DSHARP-90). The complete absence of the opacity cliff does not allow a considerable fraction of smooth disks to enter the SLR (1.3%), while a similar fraction of substructured disks match, as in the DSHARP-50 case (> 10.2%). This heat map is included in Section A.4.

From these heat maps we can extract three important results:

- Disks with strong traps (i.e., massive planets) follow a different SLR than smooth disks, while smooth disks are more consistent with the SLR in terms of the shape of the relation.
- Whether a smooth disk matches or not depends heavily on the opacity model. Birnstiel et al. (2018) DSHARP opacities produce significantly fewer simulations in the SLR than the Ricci et al. (2010) R10-0 model and only a fraction of the simulations match the semi-porous and very porous grains and the model DSHARP-50 and DSHARP-90. Therefore, the porosity should be lower than 50% when the Birnstiel et al. (2018) opacities are used. However, the distribution of simulations is significantly tighter than the observed correlation for the smooth disks with the R10-0 opacity. As discussed in Section 5.5, the observed correlation can be a mixture of smooth and substructured disks that adds scatter to the simulated SLR.
- A bright disk (top right on the SL diagram) is more likely to remain in the SLR if there is a pressure bump formed in the first 1Myr, regardless of the opacity model.

Width of the pressure maxima

To understand the overall shape of the heat map for the case with massive planets (i.e., the red lines in Figure 5.6 and Figure 5.7), we derive a theoretical estimate in the following. This estimate depends on the width and position of the pressure maximum formed outside the position of the gap-opening planets. We therefore first derive a relation of the gas width versus radius r, planet/star mass ratio q, and scale height h, using hydrodynamical simulations of planet-disk interaction with the FARGO-3D code (Benítez Llambay & Masset 2015). In Section 5.4.2 we estimate the SLR based on these empirically determined widths. For a complete derivation of the two sections, we refer the reader to Section A.1 and Section A.1.1.

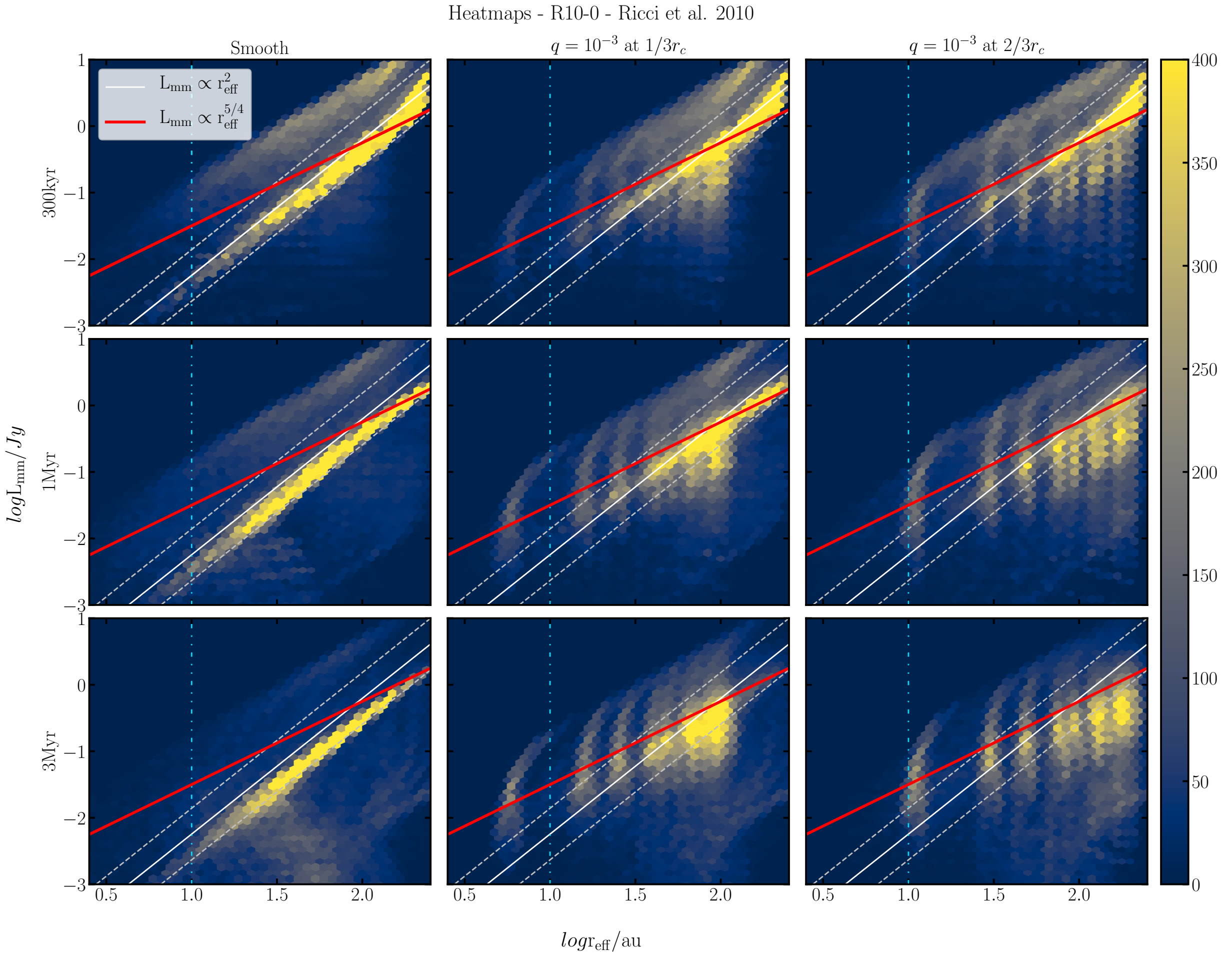

Figure 5.6: Heat maps of simulations with the R10-0 opacities. From left to right, the three columns represent the smooth case, a planet at $1/3r_c$, and a planet at $2/3r_c$. From top to bottom, the rows represent three different snapshots at 300kyr, 1Myr, and 3Myr. The white solid line is the SLR from Andrews et al. (2018a) and the red solid line our fit for the cases where a planet is included. The color bar shows the number of simulations in a single cell. The blue dash-dotted line shows the minimum limit ($r_{eff} \sim 10$ au) where observational results are available.

In addition to our two-pop-py models, we performed 24 hydrodynamical simulations with FARGO-3D (Benítez Llambay & Masset 2015) for different planet/star mass ratios, planet locations, and α-values (see Section A.3). We used these simulations to calculate the width of the outer pressure bump caused by the planet in the gas. The surface density maximum is locally well fitted by a Gaussian, which allows us to measure the width (i.e., the standard deviation) using the curvature at the maximum. By measuring all the widths of our hydrodynamical simulations we fit as a multiple power law to search how they scale with radius, scale height, and the α-parameter,

$$\sigma_g = C \cdot h^p \cdot q^k \cdot \alpha^l , \tag{5.14}$$

where C is a constant, h is the scale height, q the mass ratio, and α the turbulence parameter. We

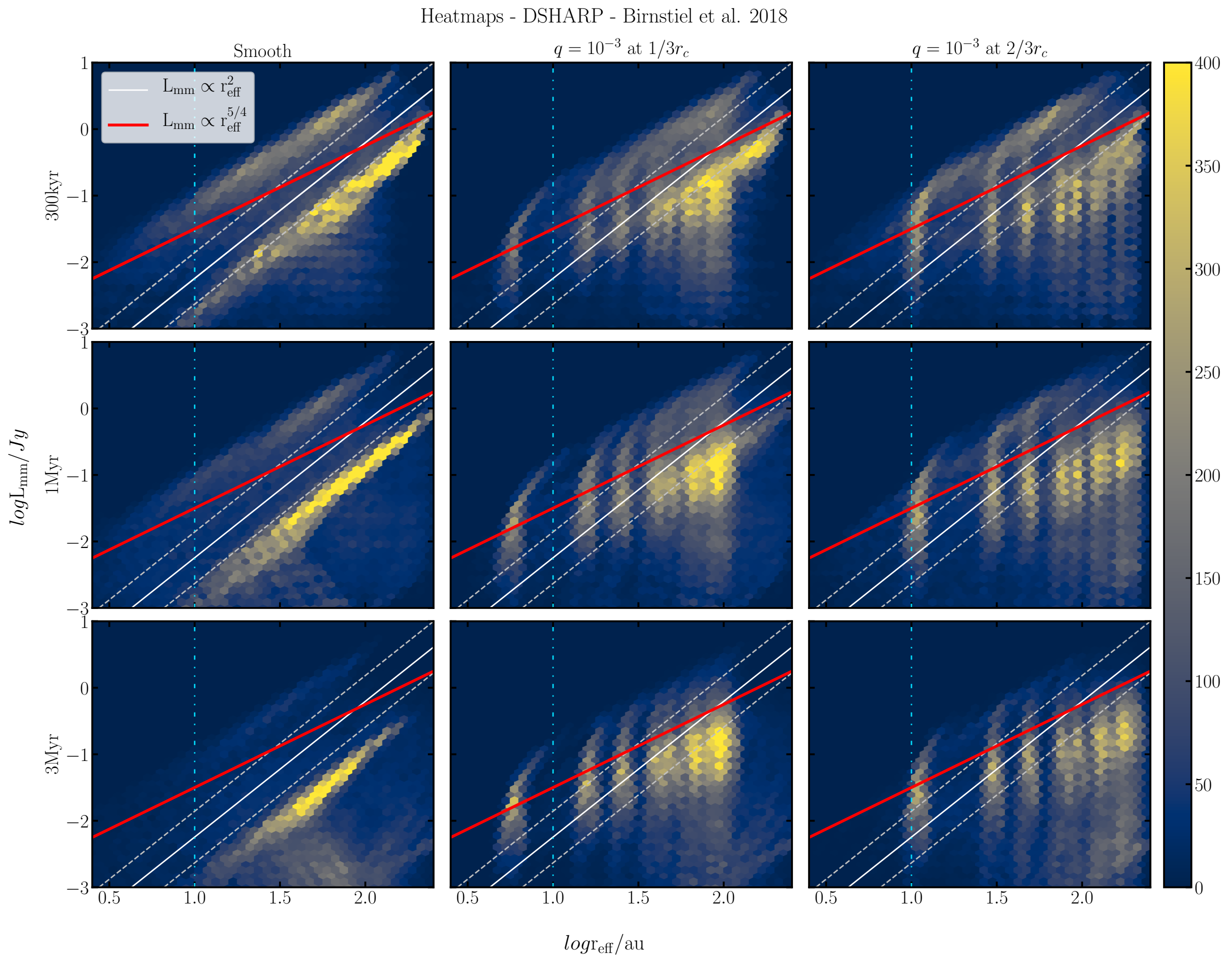

Figure 5.7: Heat maps of simulations with the Birnstiel et al. (2018) opacities. From left to right, the three different columns represent the smooth case, a planet at $1/3\mathrm{r_c}$, and a planet at $2/3\mathrm{r_c}$. From top to bottom, the rows represent three different snapshots at 300kyr, 1Myr, and 3Myr. The white solid line is the SLR from Andrews et al. (2018a) and the red solid line our fit for the cases where a planet is included. The color bar shows the number of simulations in a single cell. The blue dash-dotted line shows the minimum limit ($\mathrm{r_{eff}} \sim 10\,\mathrm{au}$) where observational results are available.

find that the width in the measured range scales approximately as

$$\sigma_g \propto h^{0.81} \cdot q^{0.14} \cdot \alpha^{0.05} \,. \tag{5.15}$$

Size-luminosity relation of disks with companions

In Figure 5.6 we show a red line that scales differently from the SLR when we include planets. We predict that this line fits with a correlation $\mathrm{L_{mm}} \propto \mathrm{r_{eff}^{5/4}}$. If we assume that all the luminosity

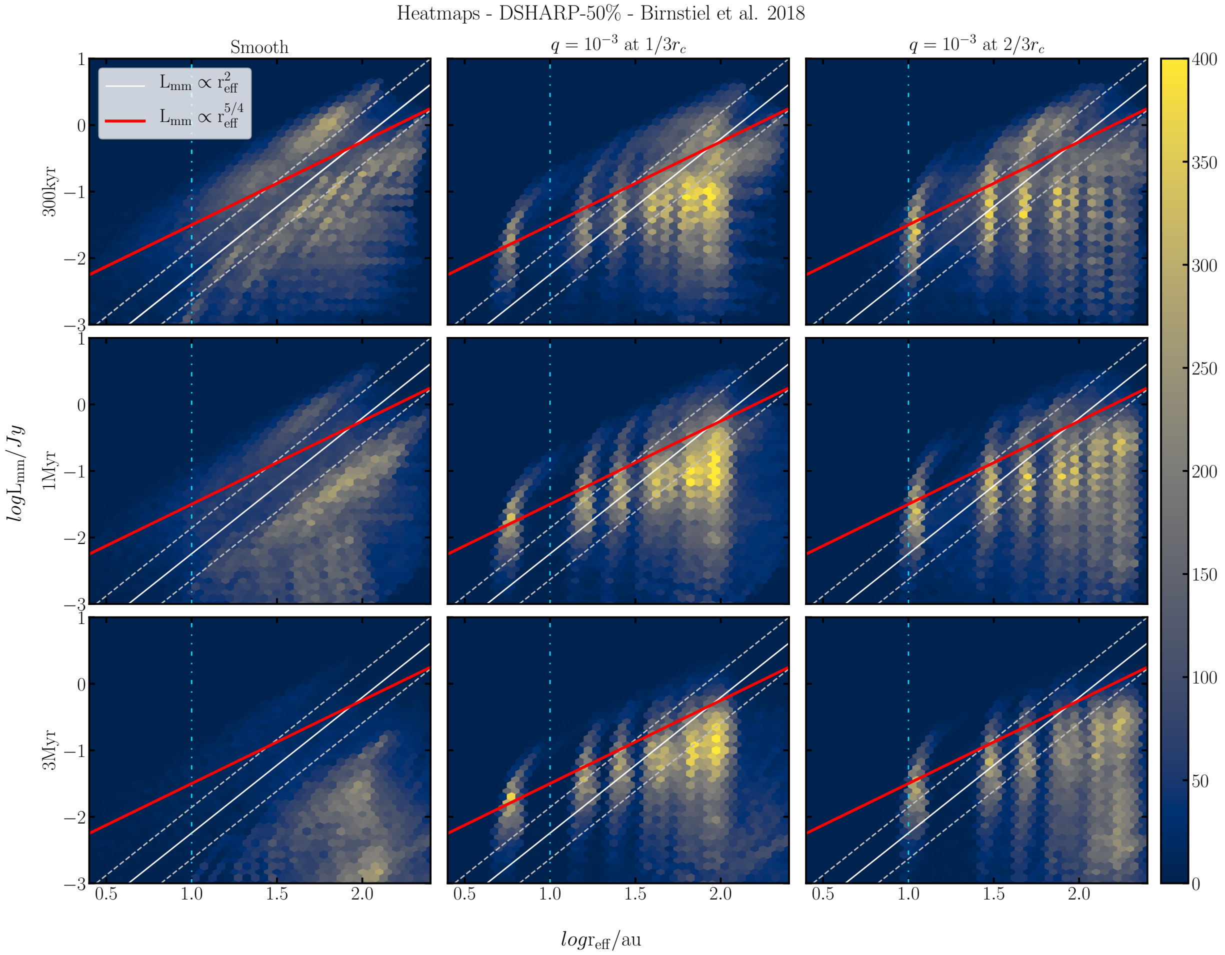

Figure 5.8: Heat maps of simulations with the Birnstiel et al. (2018) D-50 opacities with 50% porostiy. From left to right, the three columns represent the smooth case, a planet at $1/3r_c$, and a planet at $2/3r_c$. From top to bottom, the rows represent three different snapshots at 300kyr, 1Myr, and 3Myr. The white solid line is the SLR from Andrews et al. (2018a) and the red solid line our fit for the cases where a planet is included. The color bar shows the number of simulations in a single cell. The blue dash-dotted line shows the minimum limit ($r_{eff} \sim 10$ au) where observational results are available.

of a disk comes from rings that are approximately optically thick, we can approximate as

$$L \simeq A \cdot B_\nu \,, \tag{5.16}$$

where A is the area and B_ν is the Planck function. If we assume the Rayleigh–Jeans approximation to approximate the Planck function with the temperature, the equation becomes

$$L \simeq A \cdot T \,. \tag{5.17}$$

We make the assumption that the area of the pressure bump scales as $A \propto r \cdot \sigma_d$, where r is the radius and σ_d is the width of the pressure bump in the dust and there is linear scaling of σ_d with

h. The width of the dust ring depends on the width of the gas,

$$\sigma_d \propto \sigma_g \cdot \sqrt{\frac{\alpha}{St}}, \tag{5.18}$$

as in (Dullemond et al. 2018), where St is the Stokes number, while in the ring there is also effective dust trapping and diffusion. Using the relation that previously measures the gas width in Section 5.4.2, we find that the luminosity (L_{mm}) scales with the radius as

$$L_{mm} \propto r_{eff}^{5/4} \tag{5.19}$$

which is the relation that we plot with the red line in Figure 5.6, Figure 5.7, Figure 5.8, and Figure A.8. We find that this theoretical estimate nicely explains the size-luminosity scaling seen when strong substructure is present. However, toward larger radii, this relation slightly overpredicts the luminosity. For example, we could get a shallower slope looking at the heat map because toward large radii our fitting line is above the main bulk of the simulations. For a complete derivation of the two sections, we refer the reader to Section A.1 and Section A.1.1.

5.5 Discussion

To summarize the results discussed above, we explored the observed trend among the (sub-)mm disk continuum luminosity (L_{mm}) and the 68% effective radius (r_{eff}) of protoplanetary disks. Following the size-luminosity relation (SLR) obtained from Tripathi et al. (2017) and Andrews et al. (2018a), $L_{mm} \propto r_{eff}^2$, we showed which initial conditions are favorable for a disk to remain on the SLR for a time span of 300 kyr - 3 Myr. We explored the effect of every parameter on the disk evolution tracks on the SL Diagram, we got a visual representation of how the disk population moves on the same diagram, and we found relations between the parameters (Section A.2). We present a different correlation for disks that are dominated by strong substructures compared to the disks that have a monotonically decreasing surface density profile. Moreover, we investigated the effect of different opacity models with compact or porous grains and we conclude that it is a major factor in reproducing the observational results. In the following sections we briefly recap these results and we discuss in detail some of the implications.

5.5.1 Dominant parameters

In summary, our results imply that the most dominant parameters for the evolution of disks are the viscosity parameter α, the initial disk mass M_d, the location of a giant planet if present, and the opacity model that is used to derive the continuum intensity. The disks that match the SLR are characterized by low turbulence ($\alpha \leq 10^{-3}$) and high disk mass ($M_d \geq 2.5 \cdot 10^{-2} M_\star$), and they are affected strongly by the existence of a strong trap (in this study caused by a giant planet).

Turbulence-α values greater than 10^{-3} lead to smaller grains due to fragmentation, and consequently to less luminous disks that do not enter the SLR. Moreover, particles are diffused more efficiently and, due to their size, are less efficiently trapped. Finally, the dust trap is not as pronounced if the alpha viscosity is higher. All of this acts in concert to make dust trapping ineffective, and causes the disks to behave as if they were smooth (see Figure 5.3 in Section 5.4). If the fragmentation velocity is high enough, there can be simulations that stay on the SLR, but we consider these disks to have unrealistic initial conditions according to the known literature.

High initial disk mass locates the disks initially either inside or above the SLR (i.e., too bright for the given size) until they reach a quasi-steady state. This allows them to migrate to lower luminosities while they evolve up to 3 Myr and still remain in the SLR. This effect is aided by the right choice of opacity model and grain porosity. Compact grains shift the position of disks to higher luminosity (see Section 5.5.3). On the other hand, most of the less massive and smaller disks end up below the correlation at lower luminosities, characterizing them as discrepant.

Planets can alter the evolution path of the disk on the SL Diagram significantly. An effectively trapping planet causes the disk to quickly settle to a quasi-steady state on the SL Diagram, thereby leading to a shorter track and thus delaying the evolution of disks toward lower luminosity and radius. Disks with a massive planet in the inner part of the disk ($1/3\mathrm{r}_\mathrm{c}$) have more extended evolutionary tracks that are overall less luminous. In contrast, disks with a planet in the outer part ($2/3\mathrm{r}_\mathrm{c}$) have shorter and more luminous disks if all the other parameters remain the same. This can be explained by the planet trapping a large part of the disk solids at large radii. When two planets are included then both of them contribute to the luminosity while the outer one defines the effective radius of the disk. Overall, the presence of planets increases the fraction of matching simulations on the SLR, but this result is also a function of the opacity (see Section 5.5.3).

5.5.2 Position along the SLR

The position of a disk along the SLR is determined mainly by the disk mass M_d and the disk size r_c, as can be seen in Figure 5.2 and Figure 5.4. More massive and large disks are located in the top right part of the SL diagram, while small and less massive are in the middle and left parts. In Figure 5.9 we show the kernel density estimate (kde) of the luminosity for all matching simulations for four different cases and three different snapshots, and also plot the observational kde from Andrews et al. (2018a). The brightest disks that stay on the SLR are those that contain planets that are located at the outer part of the disk (2/3 of the r_c, yellow and green lines). A planet in the outer region leads to larger, more luminous disks as explained in Section 5.3.3 and Section 5.5.1. Massive planets at 1 and 3 Myr reproduce the peak of the observed brightness distribution, but overall produce too many bright and too few faint disks. The peak of the luminosity distribution for smooth disks is generally at much lower luminosities. Given these results, it is conceivable that the observed sample consists of two distinct categories of disks: a brighter and larger category due to massive outer planets that trap the dust while planets in the second category are not massive enough to trap the dust effectively and these disks evolve similarly to a smooth disk.

5.5.3 Opacity model preferences

We used different opacity models for our study. As a base model, we made use of the composition of Ricci et al. (2010) opacities (R10-0), but for compact grains (i.e., no porosity) as in Rosotti

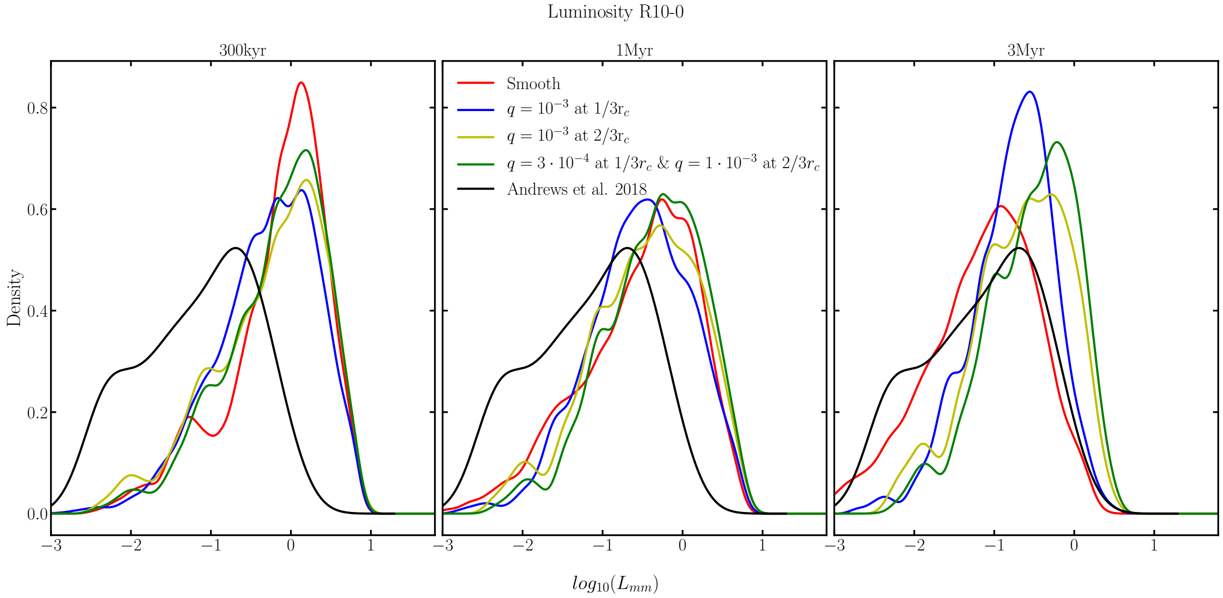

Figure 5.9: Kernel density distribution of the luminosity for all matching simulations using the Ricci et al. (2010) R10-0 opacity model, for four different cases and three different snapshots, from 300kyr – 3Myr. The black line refers to the disks from the Andrews et al. (2018a) sample. Disks with planets have higher luminosity, while smooth disks have low luminosity at 3Myr. When two planets are included the luminosity is higher than with a single planet.

et al. (2019a). Moreover we used the non-porous Birnstiel et al. (2018) opacities (DSHARP) and varied the porosity between 10% DSHARP-10, 50% DSHARP-50, and 90% DSHARP-90.

Therefore, we find that independent of the model used, relatively compact grains ($< 50\%$) are preferred instead of the highly porous grains. When compact grains are included the initial position of the disks on the SL Diagram is shifted toward higher luminosity giving it more time to evolve in the SLR on our chosen time span. Disks with the DSHARP opacity are generally less bright and end up below the SLR. We recall that the opacity at our wavelength is a factor of ~ 8.5 higher in the R10-0 case compared to DSHARP at the opacity cliff location ($\sim 0.1 - 1$mm), with the difference mainly stemming from the choice of carbonaceous material (Zubko et al. 1996 versus Henning & Stognienko 1996, see the comparison in Birnstiel et al. 2018). However, this point holds only for smooth disks and disks with weak substructures (where a disk behaves as smooth). If this is the case then only compact grains can explain the SLR; instead, when substructures are strong then any of the opacity models and the porosities tested in this work can explain the substructured SLR. The latter applies because most of the substructures become optically thick.

It can be argued that alternative compositions that also exhibit a strong opacity cliff and a high opacity would be equally suitable.

5.5.4 Types of disks on the SLR

We show that when strong traps (i.e., massive planets) are included, then disks follow a different SLR than the smooth ones. Based on measurements of the width of the pressure maxima formed by the planet in hydrodynamical simulations (see Section A.1), we derived a theoretical prediction for disks with substructures (Section 5.4.2). Smooth disks with compact or slightly porous grains seem to follow the Andrews et al. (2018a) relation $L_{mm} \propto r_{eff}^2$, while disks with massive planets follow a relation $L_{mm} \propto r_{eff}^{5/4}$.

This result does not imply that the observed disks from the Tripathi et al. (2017) sample are all free of substructure, but they might not show strong enough and optically thick substructures, such as AS209 or HD163296 (see Huang et al. 2018a). Figure 5.6 shows how smooth disks follow the SLR, while disks with strong substructures follow a different relation but intersect the SLR at the bright end (top right part of the SLR). In contrast, the less luminous disks follow the SLR if they are smooth, but disks of the same effective size with substructure are too luminous (cf. bottom left part of the SLR).

In Hendler et al. (2020, Fig. 6), disks seem to follow a universal relation (close to the SLR) in all star-forming regions (Ophiuchus, Tau/Aur, Lupus, ChaI) except for USco, the oldest region ($\sim$ 10Myr). The observed SLR therefore might flatten with age of the region. We could examine these results since we evolve our simulations to 10Myr, but our models do not include photoevaporation and that would lead to uncertainties in the results. For example, at the age of USco the detectable disk fraction is < 20%, while in our models it would be 100%.

This raises a question. If a planet is not massive at early times, but around 1 Myr has a planet/star mass ratio of $q = 10^{-3}$, will the disk follow the observed SLR or the SLR with strong substructures? According to the analysis of the evolution tracks in Section 5.4.1, most of the small and less luminous disks that do not initially have a giant planet drift toward lower radii and luminosities and even below the SLR. Therefore, strong substructures need to form in the first ~1 Myr for the disk to follow the $L_{mm} \propto r_{eff}^{5/4}$ relation. This result might imply that in most of the star-forming regions, strong substructures might not have formed early enough for small disks, or that the substructure is weak. On the other hand, bright and large disks can very clearly show strong substructures and follow the SLR at the same time. This is indeed the case for the DSHARP sample (Andrews et al. 2018b), which is biased toward bright disks and shows significant substructures in every source. The latter can be confirmed from Figure 5.9 in the previous section. The brightest disks that stay on the SLR are those that contain planets that are located in the outer part of the disk (yellow and green lines).

The SLR can be explained if there is a mixture of both smooth and strong substructured disks. Smooths disks always follow the SLR, as shown in Figure 5.6, while the bright substructured disks populate the upper right part of the SLR (Figures 5.6, 5.7, and A.8). Disks with substructures that have large r_c and low disk mass M_d populate the lower right part of the plot under the SLR. These disks are not favored by Andrews et al. (2018a), who find a tentative positive correlation between the mass of the star (or the disk) and the size of the disk. If massive small disks are excluded from the plot then the SLR could be reproduced by both substructured disks that occupy the upper right part and smooth (or weakly substructured) disks that occupy the lower left part of the SLR. Our results seem to be in agreement with the observational classification of van der

Marel & Mulders (2021) who suggest that all bright disks should have substructures formed by giant planets. Moreover, the SLR for the substructured disks is independent of the opacity model, but it slightly overpredicts the luminosity for the very large disks (see Section 5.5.3 for more about the opacity).

5.5.5 $L_{mm} - M_\star$ relation

In Section 5.4.1 we discuss that the stellar mass ($M_\star$) is directly correlated with the disks mass (M_d) and that the disk temperature is only a weak function of $L_\star$ (and therefore $M_\star$). The fact that the disk mass scales with the stellar mass implies that the luminosity (L_{mm}) scales with the stellar mass. In Figure 5.10 the $L_{mm} - M_\star$ relation is shown for three different models for all matching simulations: the smooth case (yellow lines), a planet with planet/star mass ratio $q = 10^{-3}$ at $1/3r_c$ (green lines), and a planet with the same mass ratio at $2/3r_c$ (red lines). The markers define the median value of the luminosity at 1 Myr and the error bars are the 75% percentile from the upper and lower value. The blue line is the $L_{mm} \propto M_\star^{1.5}$ correlation from Andrews et al. (2018a), a correlation that is consistent with those found from previous continuum surveys of comparable size and age (Andrews et al. 2013; Ansdell et al. 2016; Pascucci et al. 2016). For any of our models the correlation is not as steep as for the Andrews et al. (2018a) model, but the cases with strong substructures have steeper profiles than the smooth cases. The reason is that no correlation between disk size and stellar mass was imposed in the parameter grid. If a size-mass correlation as inferred by Andrews et al. (2018a) were imposed, the mass-luminosity relation is expected to steepen as disks with optically thick substructures would be larger and therefore brighter. However, reproducing the observed mass-luminosity trend will be part of a future population synthesis study. A similar manifestation of the same trend can be seen in Figure A.2. In the panel $r_c - M_d$, shown as white dots, is the mean value of the characteristic radius for every disk mass. In order for the correlation to reproduce the observations, more massive disks should have initially been larger. In other words, large low luminosity disks would be expected in the lower right of the SL diagram, but are not observed. Preliminary results indicate that these disks need to have low disk mass ($M_d < 10^{-2} M_\star$) and be large in size ($r_c > 150$ au). Moreover the turbulence parameter should be relatively small $\alpha \leq 10^{-3}$, otherwise the disk would behave as smooth and woul follow the SLR.

5.5.6 Scattering

Scattering is included in our simulations, as introduced in Section 5.3.4. Compared to the case where only the absorption opacity is used, the difference is minimal and it can be observed only in a few cases. With the inclusion of scattering, the originally brightest disks (above the SLR) tend to move toward lower luminosity (move down in the SL diagram). This happens for disks that are optically thick, hence for those that contain planets. This effect favors the SLR and allows slightly more disks ($\sim 2\%$) to enter the selected region. However, for moderately optically thick disks the emission is larger and a small fraction of disks move up (toward higher luminosity) on the SL diagram (Figure 4 in Birnstiel et al. 2018). This happens because the derived intensity (Eq. 5.11) does not saturate to the Planck function, but to a slightly smaller value for a non-zero albedo. This

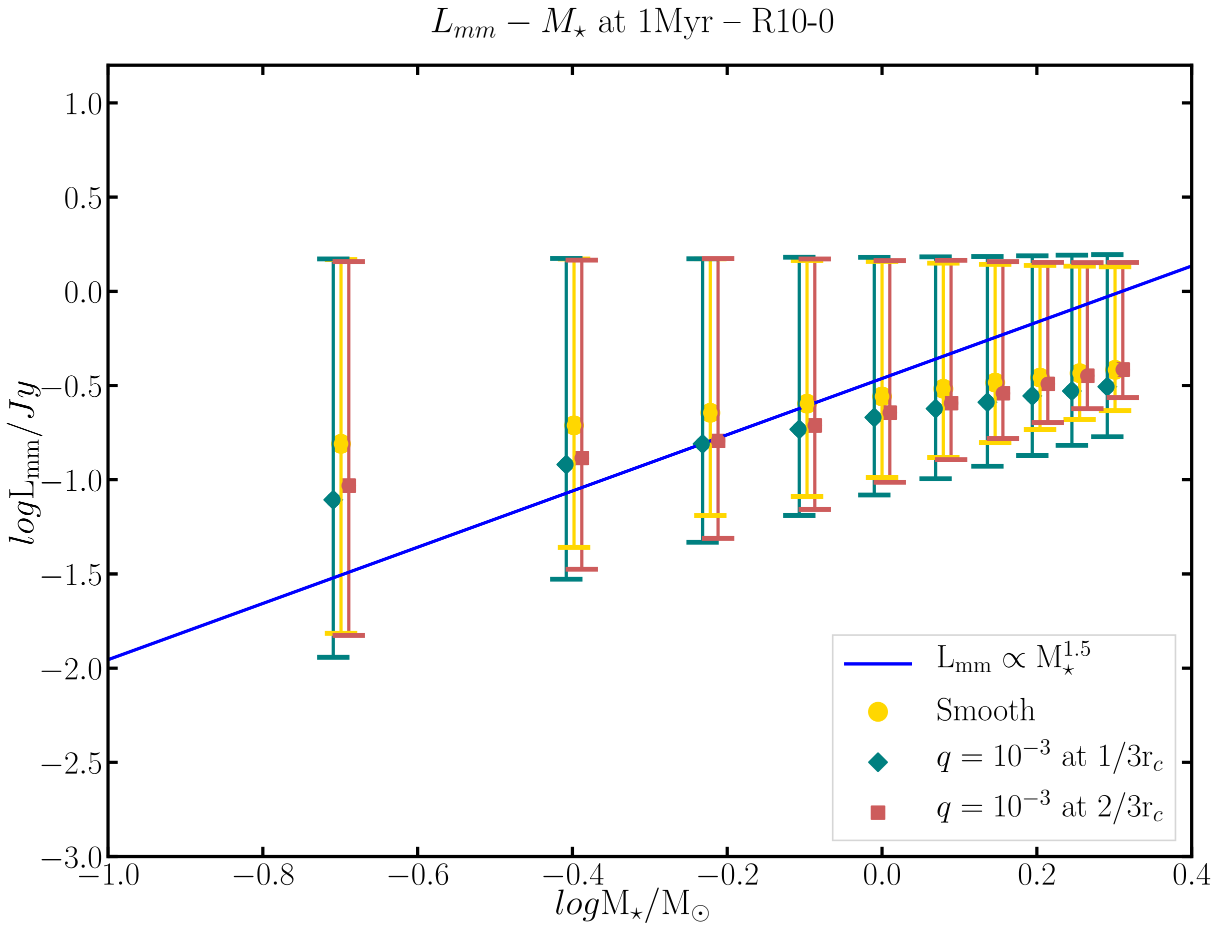

Figure 5.10: $L_{mm} - M_\star$ relation at 1Myr for three different cases for the matching simulations. Smooth case (yellow lines), a planet with planet/star mass ratio $q = 10^{-3}$ at $1/3r_c$ (green lines) and a planet with the same ratio at $2/3r_c$ (red lines). The points define the median value of the luminosity at 1Myr and the error bars are the 75% percentile from the upper and lower value. The blue line is the $L_{mm} \propto M_\star^{1.5}$ correlation from Andrews et al. (2018a).

is the well-known effect that scattering makes objects appear cooler than they are in reality. On the other hand, for small optical depths ($\tau << 1$) the effect of scattering is insignificant because the intensity (Eq. 5.11) approaches $I_\nu^{out} \longrightarrow \epsilon_\nu^{eff} B_\nu(T_d)\Delta\tau/\mu$, which is the identical solution to when κ_ν^{sca} is set to zero while κ_ν^{abs} is kept unchanged, as also shown in Birnstiel et al. (2018).

The effect of scattering also depends on the albedo ($\eta_\nu = 1 - \epsilon_\nu^{eff}$). For the compositions we use, the maximum effective albedo is 0.57 for R10-0 and 0.82 for DSHARP, while it can reach ~ 0.97 for DSHARP-90. For these compositions the effect of scattering is never more than a factor of ~ 1.7 at a particle size of 1mm. The result of scattering is higher if we increase the albedo, but by using a plausible composition the result is effectively negligible.

However, we obtain different results compared to Zhu et al. (2019). In that work the authors discusse that a completely optically thick disk with high albedo (0.9) can be constructed, which therefore lies along the SLR with the right normalization (because the high albedo and high optical depth lowers the luminosity). However our findings show that we cannot reach those results from an evolutionary perspective. For smooth disks the dust drifts to the inner part of the disk and the disk is no longer optically thick. On the other hand, disks with substructures create only rings rather than disks that are completely optically thick everywhere.

5.5.7 Predictions for longer wavelengths

A recent study (Tazzari et al. 2021), showed a flatter SLR at 3.1mm (Lmm $\propto \mathrm{r}_{\mathrm{eff}}^{1.2}$), confirming that emission at longer wavelengths becomes increasingly optically thin.

We performed a series of simulations at 3.1 mm for a comparison with these results. The disks are fainter and smaller at 3.1 mm. Two effects contribute to this. First, the value of the opacity decreases and the opacity cliff moves to larger particle sizes. This leads the disks to become optically thinner in comparison to the 850 μm case. Second, the intensity at 3.1 mm is less according to Plank's spectrum. Therefore, the luminosity will be lower.

In terms of the SLR, the slope for the smooth disks does not change since these disks are never optically thick; therefore, all disks simply move toward lower luminosities and smaller radii. On the other hand, the substructured disks that cover the SLR do not change in terms of slope, but the large and faint disks (right part of the heat map in Figure 5.6) show a larger spread in luminosity compared to the smaller wavelength. Disks that are very optically thick and moderately optically thick have the same luminosity at $\lambda = 850\mu$m, but at 3.1 mm because of the decrease in opacity the former category is still optically thick while the latter no longer is, leading to a decrease in luminosity. Therefore the SLR can become flatter if we can take into account these disks that do not belong in the SLR.

With our models the flatter relation from Tazzari et al. (2021), could be explained by substructured and large smooth disks. The heat map in Section A.4 confirms this. In this figure we plot the simulations at 3.1 mm, using the R10-0 opacity model and we overplot the SLR from Tazzari et al. (2021): $\mathrm{L}_{\mathrm{mm}} \propto \mathrm{r}_{\mathrm{eff}}^{1.2}$. Substructured disks can explain this relation very well since it is similar to the scaling relation we calculated for disks with strong substructures in Section 5.4.2. Small and smooth disks, on the other hand, cannot enter the relation because they are too faint since the particles cannot grow to a size where the opacity cliff is at 3.1 mm.

We should mention the possibility that the flatter relation can be due to observational bias toward large disks, which tend to be substructured. If small and faint disks are included in the sample, the observed SLR could be steeper and closer to the SLR from Andrews et al. (2018a). Future observational surveys should investigate this possibility further.

5.5.8 Limitations

It is important to keep in mind the limitations of this paper. The time span used for the simulations displayed in this paper and the figures is from 300 kyr to 3 Myr. This does not exclude the possibility that some disks with high disk mass might evolve a great deal on the SLR diagram for 10 Myr-20 Myr. Disk dissipation has not been modeled in this paper, but it will be considered for future work. In Figure 5.11 we show the kde of the global dust-to-gas ratio[2] for three different snapshots between 300 kyr – 1 Myr – 3 Myr and for three different cases. Smooth disks lose dust relatively quickly due to radial drift, while disks with planets retain a much higher dust-to-gas ratio because of the strong trap. In the second panel there are cases where the dust-to-gas ratio increases over the initial 0.01. These are substructured disks with intermediate α-values, high fragmentation velocities ($> 1000\,\mathrm{cm/s}$), and small sizes ($< 60\,\mathrm{au}$). The gas is removed more quickly than the dust, leading to a higher dust-to-gas ratio. Large values of α would lead to less trapping and the dust would drift as usual, while low α would mean that the disk does not evolve significantly.

As mentioned in Section 5.3, the stellar luminosity is not evolved in the simulation. If this were the case the disk luminosity would scale approximately linearly with the stellar luminosity and would be further modulated by resulting changes in the dust evolution. We therefore expect a general shift of the disks toward lower luminosities, but with the trends that have explored in Section 5.4 remaining the same. Since most of the simulations need to be brighter to remain in the SLR, a change in the luminosity favors higher α-values and lower fragmentation velocities than the values shown before. An example of a heat map in shown in Section A.4.1.

In our models the planets are already included at the beginning of the simulations and they open a gap in the initially smooth surface density profile relatively quickly. Realistically, the timescales in the outer part of the disk are much longer and the timescale for planet formation changes with the distance to the star (Johansen & Lambrechts 2017). Therefore, we would expect that the inner planet should form first and the outer planet later, as has been suggested (e.g., Pinilla et al. 2015). Since both planets start at the same time, the inner one might trap more of the total disk mass and the outer bump might be less bright than in our models in reality. The latter will be included in a future work by including the outer planet later in the simulation.

5.6 Conclusions

In this paper we performed a large population study of 1D models of gas and dust evolution in protoplanetary disks to study how the effective radius and disk continuum emission evolves with time. We varied a range of initial parameters and we included both smooth disks and disks that contain planets. We compared our results with the observed trend between continuum sizes and luminosities from Andrews et al. (2018a) and we managed to constrain the initial conditions. Our findings are as follows:

1. Disks with strong traps (i.e., massive planets) follow a different SLR than smooth disks. Smooth disks follow the Andrews et al. (2018a) relation, $\mathrm{L_{mm}} \propto \mathrm{r}_{\mathrm{eff}}^{2}$, as shown by Rosotti et al. (2019a), while disks with massive planets follow $\mathrm{L_{mm}} \propto \mathrm{r}_{\mathrm{eff}}^{5/4}$. This could mean that not all disks in the Tripathi et al. (2017) and Andrews et al. (2018a) joint sample have a substructure as significant as HD163296, for example. We explained this result with a simple analytical derivation and we find that if the gas width scales as we measured it from

---

[2] The dust-to-gas ratio in the disk changes with radius and time and this quantity is simply $\mathrm{M_{dust}/M_{gas}}$.

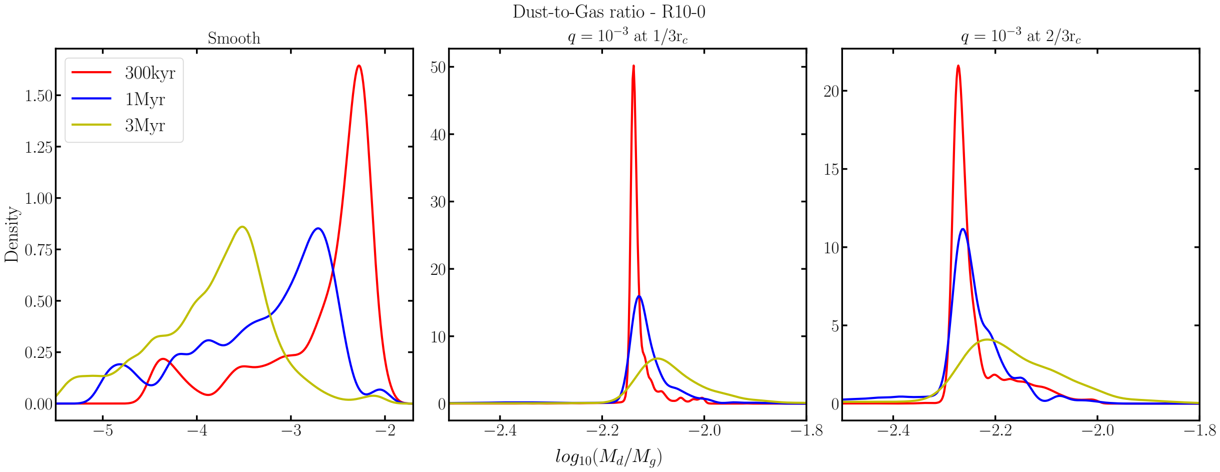

Figure 5.11: Evolution of the global disk dust-to-gas ratio of all matching simulations with the Ricci et al. (2010) R10-0 opacity model, for three different cases and three different snapshots, from 300 kyr – 3 Myr. From left to right, the smooth case, a planet with planet/star mass ratio at $1/3\mathrm{r_c}$, and a planet with the same ratio at $2/3\mathrm{r_c}$. Different limits are used on the x-axis to highlight the evolution of the dust-to-gas ratio. The initial dust-to-gas ratio is 0.01. For the smooth case the dust-to-gas ratio decreases by three orders of magnitude up to 3 Myr. When a planet is included the disk dust mass is retained and leads to a much higher dust-to-gas ratio. In the case where the planet is the inner part of the disk (middle column), there are cases at 3 Myr where the ratio is higher than 0.01. The gas mass moves faster than the dust mass in this case.

FARGO-3D and if the dust width scales as we expect it from trapping and fragmentation, then theoretically the luminosity scales as $\mathrm{L_{mm}} \propto \mathrm{r_{eff}^{5/4}}$.

2. Whether disks follow the SLR depends heavily on the opacity model. When the DSHARP (Birnstiel et al. 2018) opacity is used, disks are not as luminous in the first 300 kyr and the majority of them end up below the SLR. Especially for smooth disks, the DSHARP opacities produce a much lower number of simulations on the SLR compared to models using the Ricci et al. (2010) R10-0 opacities (0.8% with DSHARP and 29.6% with R10-0). Therefore, with this opacity model, only disks with substructures can populate the SLR. On the other hand, R10-0 opacities can reproduce disks both with and without substructures since the absolute value of the opacity at 850 μm is ∼ 8.5 times higher than DSHARP for particle sizes around ∼ 0.1 mm (position of the opacity cliff) and the disks become luminous enough to enter the relation.

3. The SLR is more widely populated when substructures are included in contrast to a tight correlation for smooth disks. Substructured disks cover mostly the upper right part (large and bright disks) of the SL diagram, while the lower left (small and faint) is covered by smooth disks. This is an indication that the SLR can be explained if there is a mixture of both smooth and strong substructured disks.

4. The grain porosity can drastically affect the evolution track of the disk. Throughout our models, relatively compact grains ($< 50\%$ porosity) are preferred for simulations that follow the SLR. If we use slightly porous grains (10%) by altering the DSHARP opacity, the effect is insignificant, as the shape of the opacity cliff is roughly the same. On the contrary, for semi-porous (50%) and porous grains (90%) the opacity cliff flattens out, leading to disks with low luminosity. Only compact grains can explain the SLR for smooth disks, while any porosity can explain it when strong substructures are included.

5. High initial disk mass gives a higher probability for a simulation to follow the SLR. If this applies, the disk starts initially above the SLR (bright) until it reaches a stable state at around ~ 300 kyr. By this time it will enter the relation, and depending on the other initial conditions it will either remain there and be considered a matching simulation or will leave it.

6. There is a preference toward low α-values (lower than 10^{-3}). This result is in line with other more direct methods of determining α (e.g., Flaherty et al. 2018). There are multiple reasons for this tendency. For $\alpha \geq 2.5 \cdot 10^{-3}$, disks tend to be more fragmentation dominated, the particle size decreases, and consequently they are not trapped by the pressure bump (if any) leading them outside the relation. Moreover the diffusivity increases and the peak of the pressure bump smears out, leading to inefficient trapping. On the other hand, if α is low, the ring that is formed becomes too narrow and disks tend to have lower luminosity.

7. The location of the planet as a function of the characteristic radius plays a major role in the final outcome. If a planet is included in the inner part of the disk ($1/3\mathrm{r_c}$), the disk has to be significantly larger in order to retain the correct ratio of luminosity to effective radius to stay in the SLR. Instead, when an outer planet ($2/3\mathrm{r_c}$) is included the disk tends to be smaller in size. When two planets are included, the location of the outermost one defines the size of the disk, but a combination of the two defines the luminosity. These results are also affected by the opacity model.

8. We expect a less extended evolution track when substructure is included. The pressure bump halts the dust from drifting farther in, constraining this way the size of the disk and not allowing it to evolve further on the SLR. Furthermore, when two planets are included there is an indication that the inner planet should form first, otherwise there will not be a big enough reservoir of material in order to form.

9. We are not able to construct optically thick disks with high albedo (0.9) that lie along the SLR with an evolutionary procedure, as opposed to Zhu et al. (2019). Smooth disks are not optically thick due to radial drift, while disks with substructure create only optically thick rings rather than a uniform optically thick distribution.

10. We chose different gap profiles based on Kanagawa et al. (2016) and compared them again to hydrodynamical simulations. We conclude that the depth of the gap does not play an important role to the evolution of the disk on the SLR as long as the planet is big enough

to stop the particles from drifting. Instead, the width of the gap is the important parameter (see Section A.3, where we compare the different profiles for different parameters.)

This study shows how the combination of observed and simulated populations allows us to put constraints on crucial unknowns such as the disk turbulence, or the dust opacity. Future work is required to also investigate the effects of disk build-up and dissipation as well as planet migration and planetesimal formation.

Chapter 6

Final remarks

Since the discovery of the first exoplanet almost three decades ago, our understanding of how other worlds are created has changed and is evolving rapidly. The discovery of exoplanets and exoplanet systems in the past years, show that planetary systems vary widely from our own solar system. New theories are being developed, new data from observations are generated in a continuous basis and the development of new instruments like JWST is expected to give a new insight in the underlying processes in the interior of the protoplanetary disks. Moreover, in recent years, the Atacama Large Millimeter/Submillimeter Array (ALMA) has not only provided a sizable number of highly resolved observations of protoplanetary disks in dust-continuum but due to its high sensitivity, it also enabled several large, mid-resolution (of the order of 100 mas) surveys of different star-forming regions providing crucial information on population properties such as distributions of disk sizes, fluxes, or spectral indices for disks across stars of different masses and ages and across star-forming regions in different environments.

ALMA will continue to provide data with exquisite detail that are going to be responsible for the statistical signatures we observe today, therefore more population studies are expected to be produced.

6.1 Main results

Two studies on two tangentially related topics have been performed in this dissertation, one motivated by the pebble accretion model and one by the abundance of data regarding the size and the luminosity of protoplanetary disks.

6.1.1 Pebble accretion in radiative disks

Planet formation is a process far from having a complete, robust and widely accepted theory. The new systems and planets that are being observed show large differences compared to the picture we had drawn only a few years back. These findings challenged our understanding of planetary origins but the current planet formation models cannot reproduce timely the formation of the observed population. Several mechanisms have successfully reduced the time required to form giant planetary cores. One of them is the pebble accretion scenario, which however requires that a barrier must be overcome in order to reach the core mass necessary to ignite the rapid gas accretion phase. A growing planet is able to open a partial gap in the surrounding gaseous disk by generating a pressure maximum, which effectively halts the inward drift of solids in the disks, in particular the pebble component. This limit is the pebble isolation mass (Lambrechts & Johansen 2014) that follows a similar scaling as the gap opening mass

$$M_{iso,peb} \simeq 25 M_{\oplus} \left(\frac{H/r}{0.05}\right) \left(\frac{M_{\star}}{M_{\odot}}\right)$$

where H/r is the gas disk scale height.

In chapter 4 we examined the solid accretion rate efficiency on different planetary cores of different masses. We performed multiple high-resolution 3D hydrodynamical simulations with embedded solids with the code PLUTO. Using a ideal equation of state and radiative cooling for different planetary cores at the location of Jupiter (5.2 AU), we found that this mass is reduced to less than 10 $\mathrm{M}_{\oplus}$. The main reason is that radiative transfer produces a cooler and thinner disk (lower H/r). This allows the growing planet to enhance its efficiency at halting the flux of pebbles. Since this limit becomes lower than 10 $\mathrm{M}_{\oplus}$, which corresponds to the mass at which the core can start its runaway gas accretion, this result can explain the observed, relatively low gas giant planet frequency but it sets another barrier to giant planet formation in the inner part of the disk.

6.1.2 Disk Population Synthesis

The second and main project of this dissertation was focused in the population synthesis of different planetary systems. To understand planet formation, high-resolution observations and large surveys of the birthplaces of planets, the protoplanetary disks (PPDs) are essential. In recent years, the Atacama Large Millimeter/Submillimeter Array (ALMA) has not only provided a sizeable number of highly resolved observations of PPDs in dust-continuum but due to its high sensitivity, it also enabled several large, mid-resolution (of the order of 100 mas) surveys of different star-forming regions providing crucial information on population properties such as distributions of disk sizes, fluxes, or spectral indices for disks across stars of different masses and ages and across star-forming regions in different environments. These surveys open up a new range of questions that cannot be answered by studying individual disks: disk population studies, which are able to check for correlations in disk-star observables and can test general gas and dust evolution models. One of these correlations is the (sub-) mm disk Size-Luminosity relation (SLR), firstly shown in a pre-ALMA study (Tripathi et al. 2017) and later confirmed by ALMA surveys (e.g. (Andrews et al. 2018a)). They showed that disks follow a SLR in the Taurus star-forming region ($1-3$ Myr old) that could point towards radial drift of particles ruling the evolution of the disk (Rosotti et al. 2019a) or alternatively be explained by optically thick ring structures (Tripathi et al. 2017).

We used an updated version of the disk evolution code from Birnstiel et al. (2012) (twopoppy2) with a typical run-time of a few seconds, to carry out 1D gas- and dust evolution models for 10 Myr. With the purpose of running a population study, we used a large grid of parameters and we explored which physical mechanisms and parameters (turbulence, disk mass, particle properties, etc) are needed to reproduce observational properties of large disk surveys, namely disk sizes ($r_{\rm eff}$) and luminosities ($L_{\rm mm}$). By mimicking the presence of planets (Kanagawa et al. 2016) we introduced sub-structures and we ran a grid of 100.000 models.

We found that disks with strong traps (i.e. massive planets) follow a different SLR than smooth disks. Smooth disks follow the observed relation $L_{\rm mm} \propto {\rm reff}^2$ as shown by Rosotti et al. (2019a), while disks with massive planets follow a flatter $L_{\rm mm} \propto {\rm reff}^{5/4}$. This could mean that not all disks in the observed sample have sub-structure as significant as e.g. HD163296. We explained this result with a simple analytical derivation and we found that if the gas width scales as we measured it from hydrodynamical simulations and if the dust width scales as we expect it from trapping and fragmentation, then theoretically the luminosity scales as the red line in our figures in Section 5.4.2. This suggests that the SLR can be explained if there is a mixture of both smooth and strong sub-structured disks that cover the lower and the upper part of the SLR respectively. These results seem to be in agreement with the observational classification from (van der Marel & Mulders 2021) which suggests that bright and massive disks should have sub-structures formed by giant planets. Furthermore, we found that only disks with a low α-turbulence parameter ($\alpha \leq 10^{-3}$) can reproduce the SLR. Disks with higher α values tend to be more fragmentation dominated, the particle size decreases and consequently are not trapped by the pressure bump (if any) leading them below the relation. Moreover, the diffusivity increases and the peak of the pressure bump smears out, leading to inefficient trapping. On the other hand, if α is very low, the ring that is formed is becoming too narrow and disks tend to have smaller luminosity.

6.1.3 Applications to other studies

Mass determination of protoplanetary disks

In the recent years there have been numerous studies to measure the disk mass, gas or dust. A relatively new approach to measure the disk gas mass is to use theoretical models. Since the drift is derived by equating the growth and drift time-scale, there is a maximum grain size $\alpha_{\rm max} \propto \Sigma_{\rm d}$. In two studies, Powell et al. (2017, 2018) assumed that these time-scales are equal to the disk age, setting this way another constraint for the dust-to-gas ratio. Therefore, they linked the maximum radial extent of the emission at a specific wavelength, what is called the dust line, to the local gas surface density at that position. In summary, knowing the dust line location can lead to the estimation of the local surface density. In these two studies, multi-wavelength observations of dust continuum emission have been used to derive the grain size distribution and to estimate the gas surface density distribution for different protoplanetary disks.

This is where the disk population model developed in this thesis come into play. In a study performed by Franceschi et al. (2022), they used the Powell et al. (2017, 2018) method to explore which disk conditions can lead to the dust-line location to be a good surface density and consequently a good disk mass estimator.

Using the model described in chapter 5, they used different stellar and disk properties to create a disk-population-synthesis like study, changing properties like the disk mass, the stellar mass,

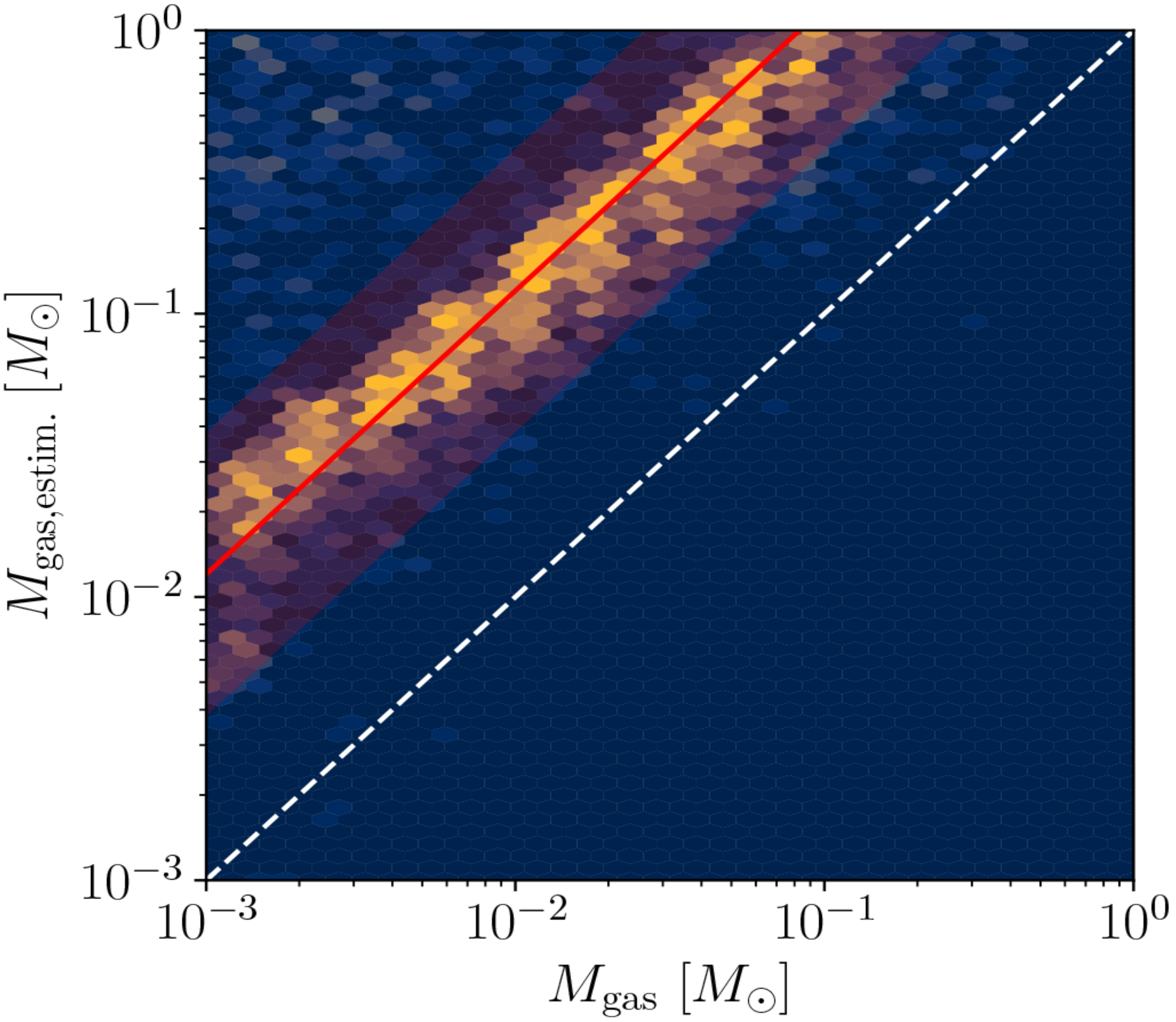

Figure 6.1: Comparison between input disk masses and the estimates from the dust line location. The shaded red area includes the best 68% of the disks, the red line is the median mass of these disks, and the white line is the correlation function for a perfect match. The dust line location systematically overestimates the disk mass by about one order of magnitude. Figure taken from Franceschi et al. (2022).

the disk age, the dust-to-gas ratio and the presence or not of sub-structures. They showed that the determination of the dust line location is a relatively good approach to define the disk mass but it greatly affects the results the underlying structure of the disk and if it contains sub-structures. When sub-structures are present the formed radial pressure bumps can alter the location of the dust line by up to ~ 10 au, while its location is mainly determined by the disk mass. On the other hand when these sub-structures act as strong dust traps the method fails. These results can been seen in Figure 6.1 where it is shown that the dust line location systematically overestimates the disk mass by about one order of magnitude.

6.2 Future work

There are a large number of attractive directions into which the disk population synthesis project can be expanded and a few questions that can be answered. It can work as a predictive tool to show if a simulation with a set of initial conditions is consistent with the observed SLR or not. Thus, it can be used to quickly test the impact of an arbitrary process on the SLR and thus to explore any directions that may emerge from the theoretical and observational progress. We can explore the disks that are large but low in luminosity and they are located below the SLR as in Figure 5.6. Are these transition disks and if so, which conditions and mechanisms are leading to this path? An observation by van der Marel et al. (2022) shows that these disks exist.

More correlations have been observed that can be directly compared with this model. The dust mass vs stellar accretion rate correlation (Manara et al. 2016), or the dust mass vs stellar mass correlation (Pascucci et al. 2016), that seems to steepen with the age of the star-forming region. Therefore, more observational properties are needed and can be produced (i.e. spectral indices, mass distributions, accretion rates, etc). There are also several ways in which the model can be improved. The current version lacks disk build-up and dispersion, therefore multiple physical mechanisms can be included to make it more accurate. Planet migration, dust-gas back reaction, planetesimal formation, photoevaporation and disk winds models are only some of them. The planet formation groups in Munich (LMU, ESO) are currently working on these mechanisms (Gárate et al. 2020) and can provide us with key information. Furthermore, using the state-of-the-art dust coagulation and evolution model DustPy (Stammler & Birnstiel 2022) we can model individual disks with great detail to derive constraints in the initial conditions and compare afterward to the full population model.

A more sophisticated planet mass recipe can be included that is based on the isolation mass from the hydrodynamical simulation and can work as a potential link between the two projects.

6.3 The future of planet formation

The future of planet formation studies depends on the understanding of the underlying structure of protoplanetary disks. This includes all the processes that have been discussed including, how dust drifts and grows, how pebbles accumulate to form planets and how the planets interact with the surrounding disk. To the current date, there is no individual model (viscous or not) that can match the observations of protoplanetary disks. A major inconsistency is that all existing models include various assumptions. These usually include observational properties that cannot be easily determined, limitations in the models due to computational needs or implementation difficulties. Furthermore, if a complicated model can be constructed then it will be limited to specific sets of disk parameters. Therefore, viscous one-dimensional models that can test multiple disk parameters that have been explored in this thesis are a powerful tool for an initial understanding and exploration, but more complex modeling, such as models that can connect dust evolution and planetesimal formation are the main bottleneck in the future of the field. The latter is a fast expanding field and more accurate models start to emerge.

A natural way forward to create such an an all-encompassing approach would be to connect as many disciplines as possible. Disk and planet population synthesis models can constrain the free parameters. Observations of protoplanetary disks need to be combined with the studies for debris disks, exoplanets, meteorites, cosmochemical and various numerical models. Every piece of information can be crucial to the underlying understanding of the holy grail that is planet formation and a connection between different fields and sciences can only move the progress forward.

Appendix A

Derivation of gap width and SLR

In this section we show the complete derivation of the width versus radius r, planet/star mass ratio q, and scale height h relation, as explained in Section 5.4.2, and the derivation of the SLR of disks with strong substructures, as shown in Section 5.4.2.

A.1 Derivation of the gap width

In addition to our two-pop-py models, we performed 24 hydrodynamical simulations with FARGO-3D (Benítez Llambay & Masset 2015) for different planet/star mass ratios, planet locations, and α-values (see Section A.3 in Section A.3). We used these simulations to calculate the width of the outer pressure bump caused by the planet in the gas. The surface density maximum is locally well fitted by a Gaussian, which allows us to measure the width (i.e., the standard deviation) using the curvature at the maximum,

$$y(x) = \frac{1}{\sqrt{2\pi}\sigma_g} e^{-\frac{(x-x_0)^2}{2\sigma^2}} , \tag{A.1}$$

where x_0 is the location of the surface density maximum. We took the logarithmic derivative of the Gaussian,

$$\frac{\partial ln y}{\partial ln x} = \frac{x}{y} \frac{1}{\sqrt{2\pi}\sigma_g} \left(-\frac{x-x_0}{\sigma^2}\right) e^{-\frac{(x-x_0)^2}{2\sigma_g^2}} , \tag{A.2}$$

which gives us

$$\frac{\partial ln y}{\partial ln x} = -x \frac{x-x_0}{\sigma_g^2} . \tag{A.3}$$

If we are close to the pressure maximum, we can approximate that $x \longrightarrow x_0 + \delta x$, and the equation yields

$$\frac{d ln y}{d ln x} = -\frac{x_0 \delta x}{\sigma_g^2} . \tag{A.4}$$

If we take the normal derivative of the above expression, we end up with the following expression:

$$\frac{\partial}{\partial \delta x}\frac{\partial lny}{\partial lnx} = -\frac{x_0}{\sigma_g^2}. \tag{A.5}$$

Solving for $\sigma_{\rm g}$, we measure the width of the maximum by calculating this derivative at the peak location for the azimuthally averaged surface density profile derived from the FARGO3D runs:

$$\sigma = \sqrt{-\frac{x_0}{\frac{\partial}{\partial \delta x}\frac{\partial lny}{\partial lnx}}}. \tag{A.6}$$

We measured all the widths of our hydrodynamical simulations, and we investigated how they scale with radius, scale height, and the α-parameter. We fit the width of the pressure bump as multiple power-law as

$$\sigma_g = C \cdot h^p \cdot q^k \cdot q^l\,, \tag{A.7}$$

where C is a constant, h is the scale height, q the mass ratio, and α the turbulence parameter. We find that the width in the measured range scales approximately as

$$\sigma_g \propto h^{0.81} \cdot q^{0.14} \cdot \alpha^{0.05}\,. \tag{A.8}$$

A.1.1 Derivation of SLR of disks with companions

To understand the overall shape of the heat map for the case with strong substructures (i.e., the red lines in Figure 5.6 and Figure 5.7), we present here the complete derivation of the theoretical estimate from Section 5.4.2. This estimate is based on the empirically determined widths (see Section A.1), as explained in Section 5.4.2, and the position of the pressure maximum formed outside the position of the gap-opening planets.

Assuming that all the luminosity of a disk comes from rings that are approximately optically thick, we can approximate

$$L \simeq A \cdot B_\nu\,, \tag{A.9}$$

where A is the area and B_ν is the Planck function. If we assume the Rayleigh–Jeans approximation, then we can substitute the Planck function with the temperature T and the equation becomes

$$L \propto A \cdot T. \tag{A.10}$$

We make the assumption that the area of the pressure bump scales as $A \propto r \cdot \sigma_d$, where r is the radius and $\sigma_{\rm d}$ is the width of the pressure bump in the dust and there is linear scaling of $\sigma_{\rm d}$ with h. The temperature is $T \propto r^{-1/2}$ and $h \propto r^{5/4}$. Combining the above relations, we obtain the theoretical expression for the luminosity:

$$L_{mm} \propto r^{7/4}. \tag{A.11}$$

In the previous section we determined how the width of the pressure maximum depends on the scale height $\sigma_{\rm g} \propto h^{0.81}$, so we need to find a relation between the σ_g and σ_d. In the pressure maximum, we assume that the disk is optically thick and that it is fragmentation-limited since there is no radial drift. If the latter applies, then

$$\sigma_d \propto \sigma_g \cdot \sqrt{\frac{\alpha}{St}}, \tag{A.12}$$

as in (Dullemond et al. 2018), where St is the Stokes number. Moreover,

$$St \propto \frac{1}{\alpha \cdot c_s^2}, \tag{A.13}$$

where c_s is the sound speed. Combining these two, we obtain that

$$h_d \propto h_g \cdot \alpha \cdot c_s. \tag{A.14}$$

The sound speed is

$$c_s \propto r^{-1/4}. \tag{A.15}$$

Using all the above equations we conclude that

$$\sigma_d \propto \sigma_g \cdot r^{-1/4}, \tag{A.16}$$

or, if we express the radius as a function of the scale height,

$$\sigma_d \propto \sigma_g \cdot h^{-1/5}. \tag{A.17}$$

The scale height is $h = c_s/\Omega$, where $\Omega = \sqrt{GM_\star/r^3}$ the Keplerian angular velocity, leading to a dependency $h \propto r^{5/4}$. Therefore, we can use Eq. A.8 and express the calculated σ_g as a function of radius:

$$\sigma_g \propto r^{1.01}. \tag{A.18}$$

Finally, we can calculate the dust width σ_d as a function of both the scale height and radius. Substituting into Eq. A.17 we obtain

$$\sigma_d \propto h^{0.61}, \tag{A.19}$$

and into Eq. A.16 we obtain

$$\sigma_d \propto r^{0.75}. \tag{A.20}$$

If we calculate again how the luminosity scales and replace the scaling of the dust width $\sigma_d \propto r^{0.75}$, we find that

$$L_{mm} \propto r^{5/4}, \tag{A.21}$$

which is the value that we fit with the red line in Figure 5.6.

A.2 Corner plots

To search for further correlations between the parameters we visualized the results similar to a corner plot; however, for a grid of parameters instead of the usual sample density. The corner plots are projections of a multi-dimensional parameter space to several two-dimensional planes. In these visualizations every box of the plot is a 2D histogram of a parameter pair, while the color varies according to the number of simulations in every cell. The color bar is given in the upper part of the plot. These visualizations contain only the simulations that match the SLR as the histograms in Figure 5.5.

In Figure A.1 we show the corner plot for the smooth case. The corner plots overall confirm the results discussed in the previous sections. In the upper left part of the plot, we show the correlation between the turbulence parameter α and the fragmentation velocity. The results show that all these plots are heavily dependent on whether the disks are drift- or fragmentation-limited. The white dots confirm that a scaling $\propto \sqrt{\alpha}$ nicely explains the correlation: simulations above this relation are strongly fragmentation-limited, and therefore do not follow the SLR (see Rosotti et al. 2019b). The bottom left cell (corresponding to $\alpha = 10^{-4}$ and $v_{\mathrm{frag}} = 200\,\mathrm{cm/s}$) is empty because it is fragmentation-limited and increasing the α-value only makes the disks more fragmentation-dominated. As the fragmentation velocity increases then the *allowed* α-value increases as well.

In Figure A.2 and Figure A.3, we show the corner plots of the cases where a planet with a planet/star mass ratio $q = 10^{-3}$ is included at 1/3 and 2/3 of the r_c, respectively. In both cases we obtain similar results. In the second column a mild covariance can be seen between the turbulence parameter α and the disk mass. Most of the simulations are toward low α-values and high disk masses, confirming once again the results from the 1D histograms, but showing that these two are the most dominant parameters.

In the bottom panel a strong correlation between α and r_c (for a limited α-range) is shown. With vertical white dots we indicate the $\alpha = 5 \cdot 10^{-3}$ value, where there is a gradual boundary from matching to discrepant simulations. This relation is visible in the second and third columns of Figure 5.6. In summary, the leftmost clump of simulations above the correlation is the case where $r_c = 10\,\mathrm{au}$. This clump is mostly above the correlation (unless $\alpha = 10^{-4}$), and it explains the empty row for $r_c = 10\,\mathrm{au}$ in the corner plots of Figure A.2 and Figure A.3.

With low α-values there is more trapping in the pressure bump and the emission is optically thick, hence the disks are brighter. Since the disks should not be too bright (because that would locate them above the SLR) or not bright enough (this would locate them below the SLR), this yields only a range of permitted α-values. This range depends on r_c. Moreover, when α increases, the emission is not optically thick anymore because the dust gets through the trap. More specifically, for $\alpha \geq 5 \cdot 10^{-3}$ (as seen in Figure 5.3), the bump can no longer efficiently trap and this is why this transition from matching to discrepant simulations occurs.

Therefore, in the case where a planet is included the strongest correlation is between α-value and the characteristic radius r_c. The area of the parameter space with the highest fraction of matching simulations is where we have small disks (around $\sim 50\,\mathrm{au}$) and low α-values. This allows us once again to constrain the disk characteristic radius to a value that is not larger than

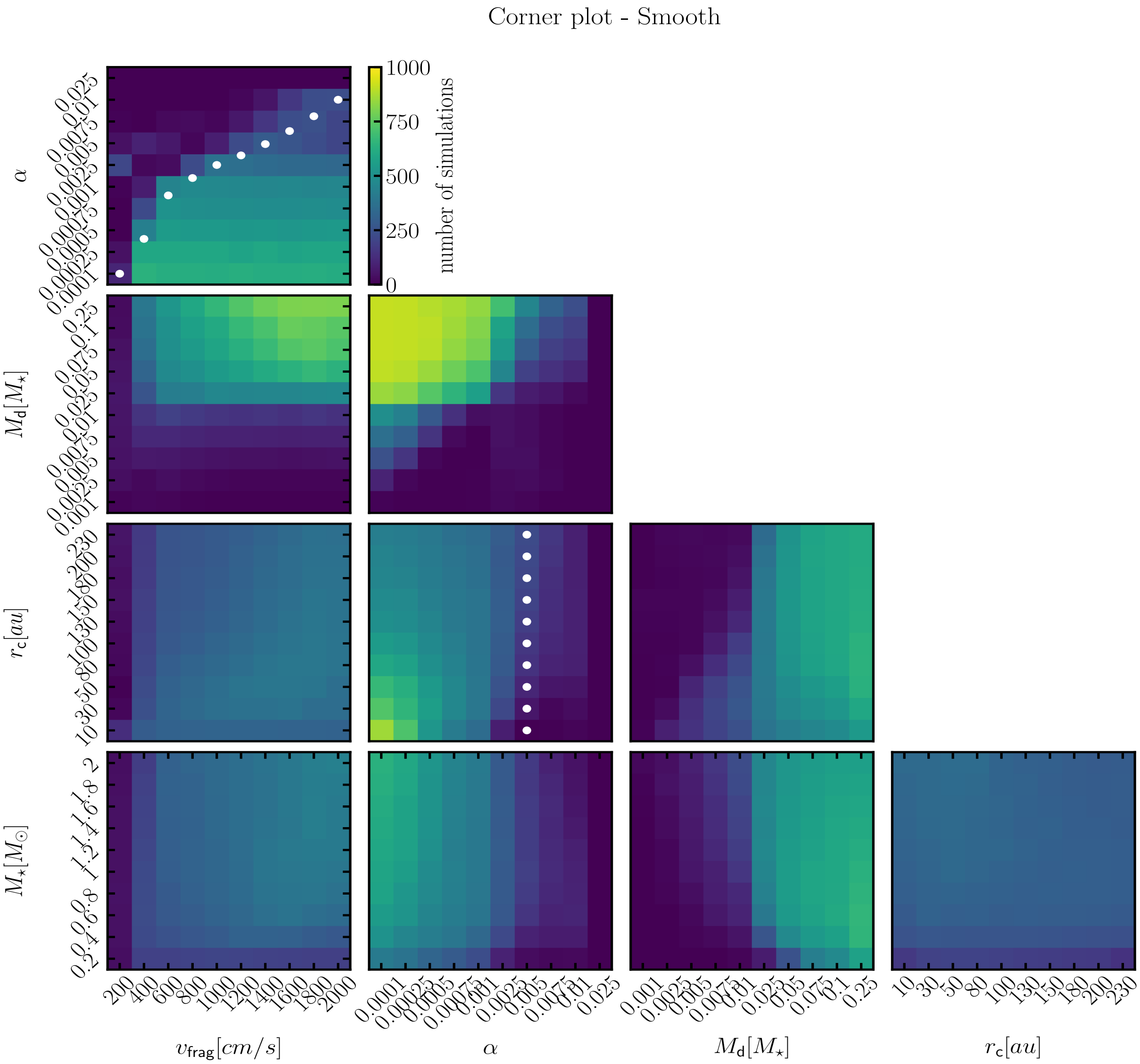

Figure A.1: Corner plot of the smooth case. From left to right: Fragmentation velocity $v_{frag}[cm/s]$, turbulence α-value, disk mass $M_d[M_\star]$, characteristic radius $r_c[au]$. From top to bottom: α, $M_d[M_\star]$, $r_c[au]$, $M_\star[M_\odot]$. In the upper left plot the white dots show the track where the distinction between the fragmentation- and the drift-limited regime is. In the middle plot ($r_c - \alpha$) the white dots show the α-value where the pressure bump cannot hold the dust efficiently anymore. In the panel r_c- M_d, the mean value of the characteristic radius for each disk mass is shown as a white dot.

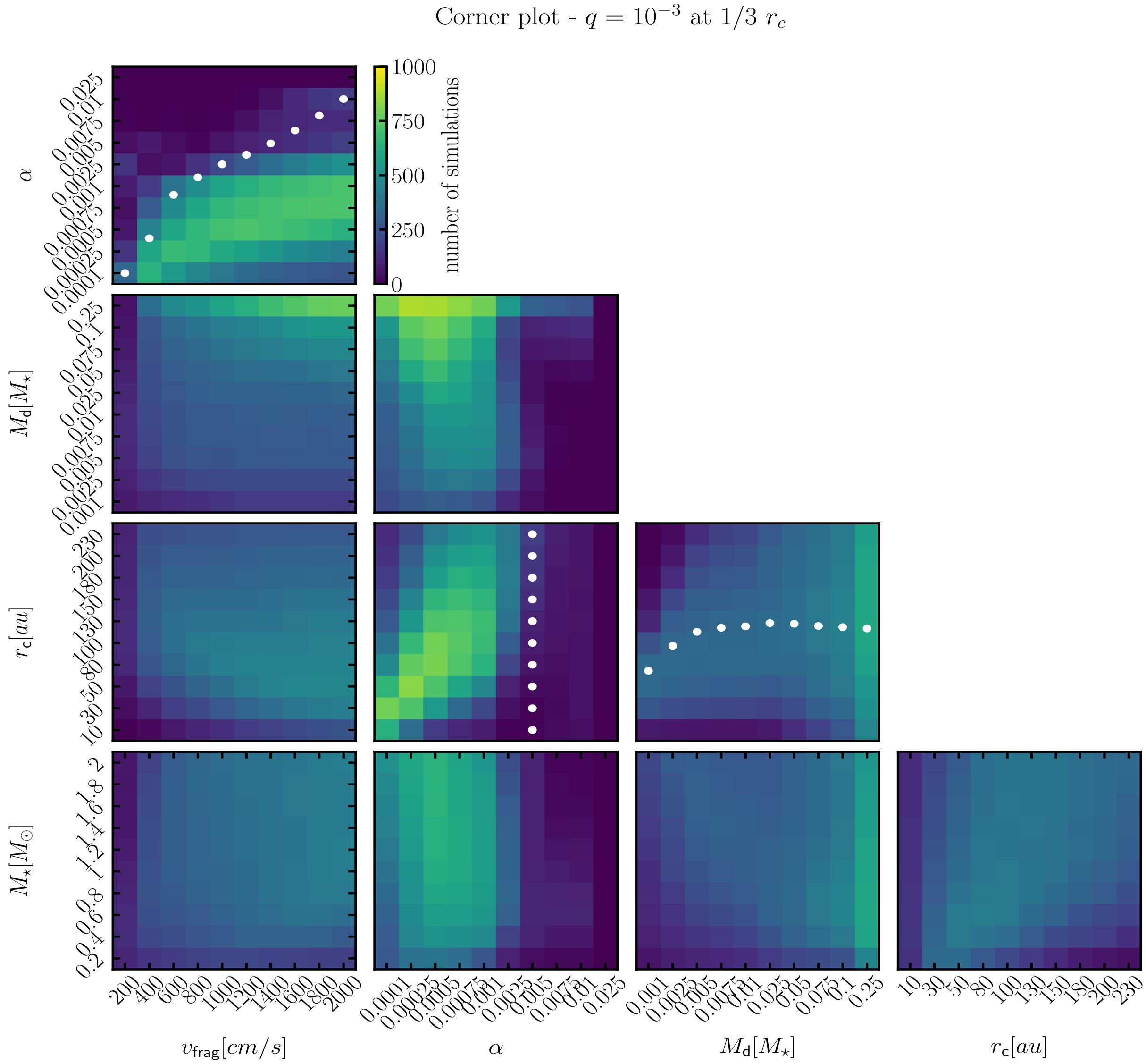

Figure A.2: Corner plot with a planet with of a planet/star mass ratio 10^{-3} at a location of the $1/3r_c$. From left to right: Fragmentation velocity $v_{frag}[cm/s]$, turbulence α-value, disk mass $M_d[M_\star]$, characteristic radius $r_c[au]$. From top to bottom: α, $M_d[M_\star]$, $r_c[au]$, $M_\star[M_\odot]$. In the upper left plot the white dots show the track where the distinction between the fragmentation and the drift limited regime is. In the middle plot ($r_c - \alpha$) the white dots show the α-value where the pressure bump cannot hold the dust efficiently anymore. In the panel r_c- M_d, shown as white dots, is the mean value of the characteristic radius for every disk mass.

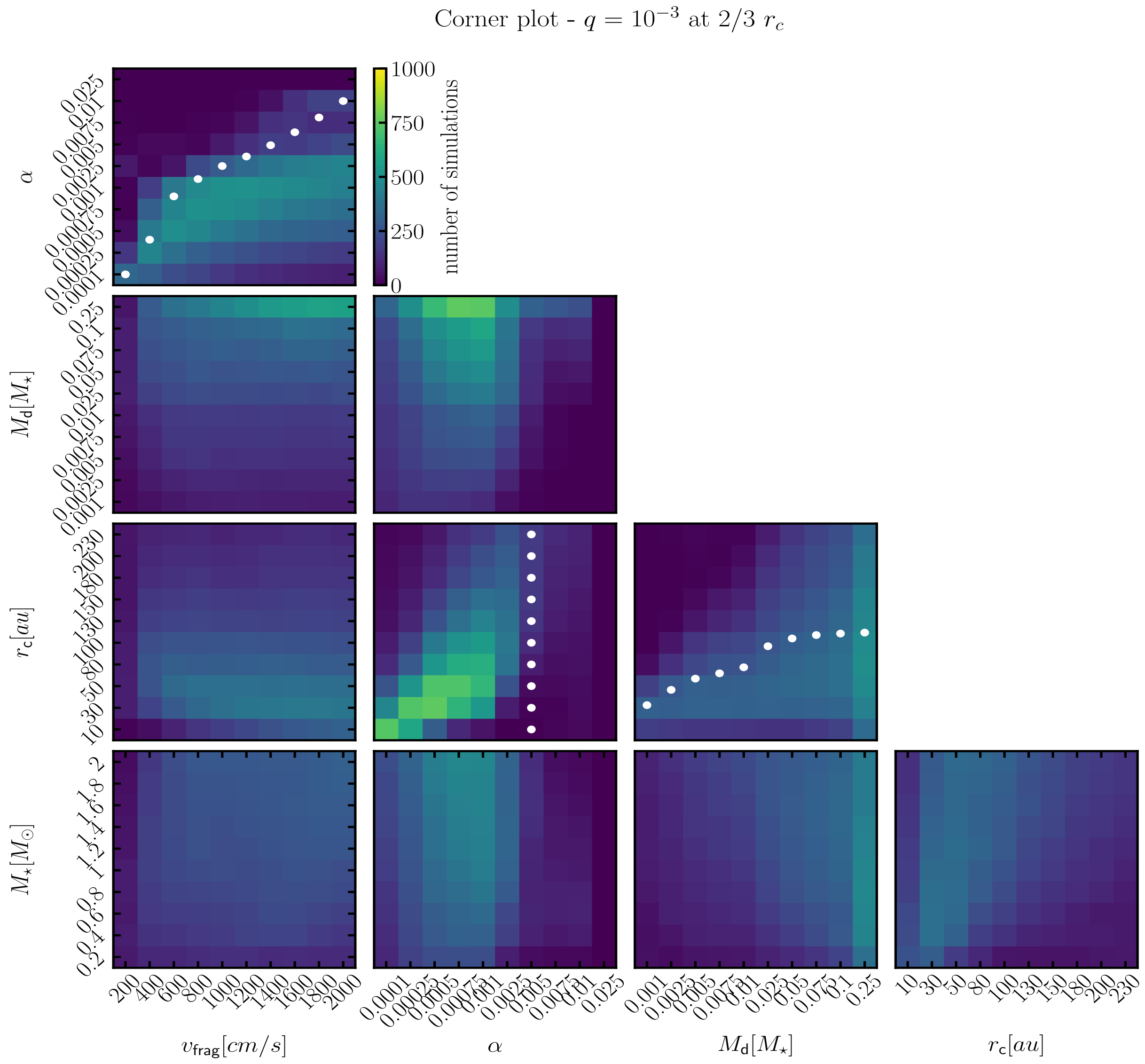

Figure A.3: Corner plot where we have a Jupiter-mass planet at a location of $2/3 r_c$. From left to right: Fragmentation velocity $v_{frag}[cm/s]$, turbulence α-value, disk mass $M_d[M_\star]$, characteristic radius $r_c[au]$. From top to bottom: α, $M_d[M_\star]$, $r_c[au]$, $M_\star[M_\odot]$. In the upper left plot the white dots show the track where the distinction between the fragmentation- and the drift-limited regime is. In the middle plot ($r_c - \alpha$) the white dots show the α-value where the pressure bump cannot hold the dust efficiently anymore. In the panel r_c- M_d, shown as white dots, is the mean value of the characteristic radius for every disk mass.

100 au.

A.3 Gap profiles

As discussed in Section 5.3, we compared the planet profile from Kanagawa et al. (2016) to hydrodynamical simulations using FARGO (Benítez Llambay & Masset 2015). We varied the turbulence parameter α, the planet/star mass ratio q, and the position of the planetary gap r_p. After obtaining the planet profile from the hydrodynamical simulation, we evolved the disk with two-pop-py (Birnstiel et al. 2012) without gas evolution to avoid diffusion of the planetary gap. We obtained the disk continuum luminosity and the effective radius, and we plotted the evolution tracks on the SLR. We evolved the simulations for 330 kyr. The parameters that we used for this test are summarized in the following table.

Table A.1: Parameters for the gap comparison

Parameter	Description	Values
α	viscosity parameter	10^{-4}, 10^{-3}, 10^{-3}
r_p [au]	planet position	30, 60, 100
q	planet/star mass ratio	$3 \cdot 10^{-4}$, 10^{-3}, $3 \cdot 10^{-3}$

In Figures A.4, A.5, and A.6 we show the comparison between the gap that is obtained from the hydrodynamical simulation and the profile from Kanagawa et al. (2016). In Figure A.4 we compare the gap profile for a small planet with planet/star mass ratio of $q = 3 \cdot 10^{-4}$ for the three different values of the α-parameter. From the low α-value (first row, first column, $\alpha = 10^{-4}$), we observe that the Kanagawa et al. (2016) profile fits the width of the gap reasonably well, but there is an offset for the depth. As we look at their evolution tracks we do not observe any major difference. For $\alpha = 10^{-3}$ (second row, first column) we have a good fit for the depth and the width in Figure A.5 and A.6. On the evolution track there is a small fluctuation, but at the end of the simulation they converge to the same point. For the high α-value (third row, first column) the profile nicely fits the width and the depth of the gap. As a result, the evolution tracks of the simulations (third row, second column) are almost identical.

Similarly, for the other cases we can observe that even if the profile does not perfectly fit the bottom of the gap, the difference in the evolution tracks is minimal. The track can be affected only if the width of the gap is not fitted properly. Therefore, we conclude that our chosen profile will not affect the main point of the paper, which is based on the observable quantities.

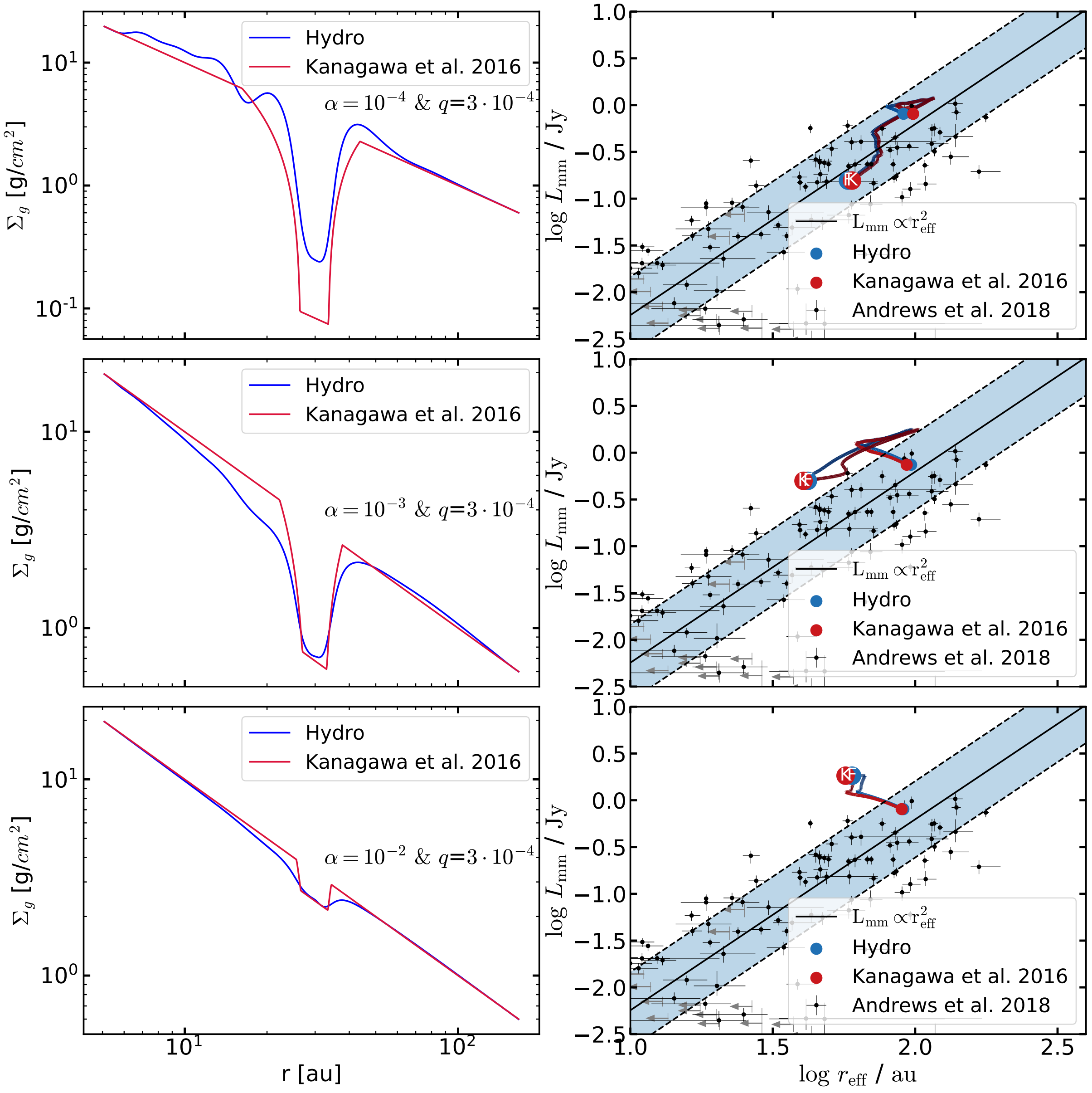

Figure A.4: Comparison between a hydrodynamical and our dust evolution simulation for different α-values and for a planet/star mass ratio q = 3 · 10^{-4} at 30 au. In the left column are the different gap profiles for different α-values and in the right column the corresponding evolution tracks. Even though the profile from Kanagawa et al. (2016) does not overlapping with that obtained from the hydrodynamical simulation, the tracks in the right column produce similar results.

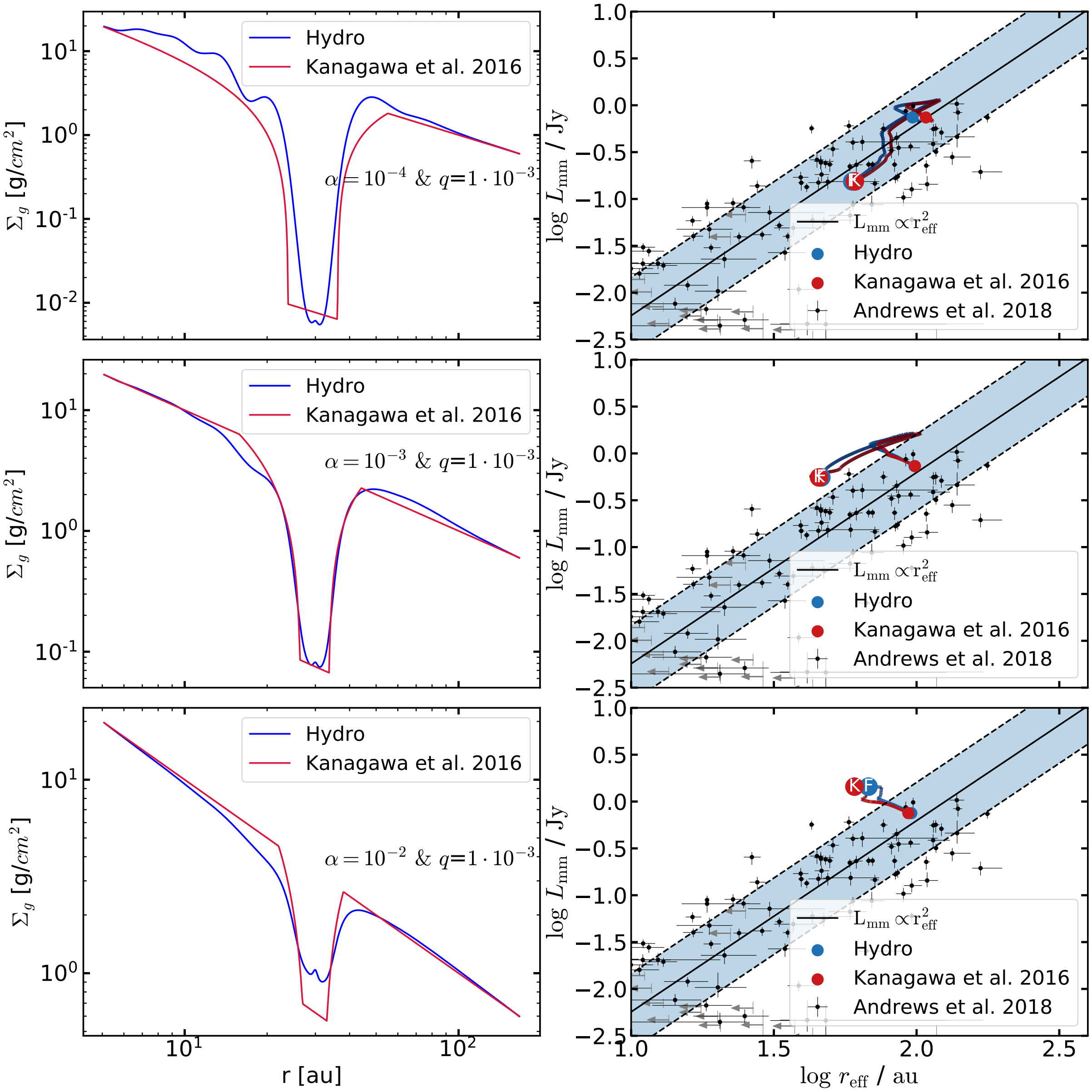

Figure A.5: Comparison between a hydrodynamical and our dust evolution simulation for different α-values and for a planet/star mass ratio q = 10^{-3} at 30 au. In the left column are the different gap profiles for different α-values and in the right column the corresponding evolution tracks. Even though the profile from Kanagawa et al. (2016) does not overlapping with that obtained from the hydrodynamical simulation, the tracks in the right column produce similar results.

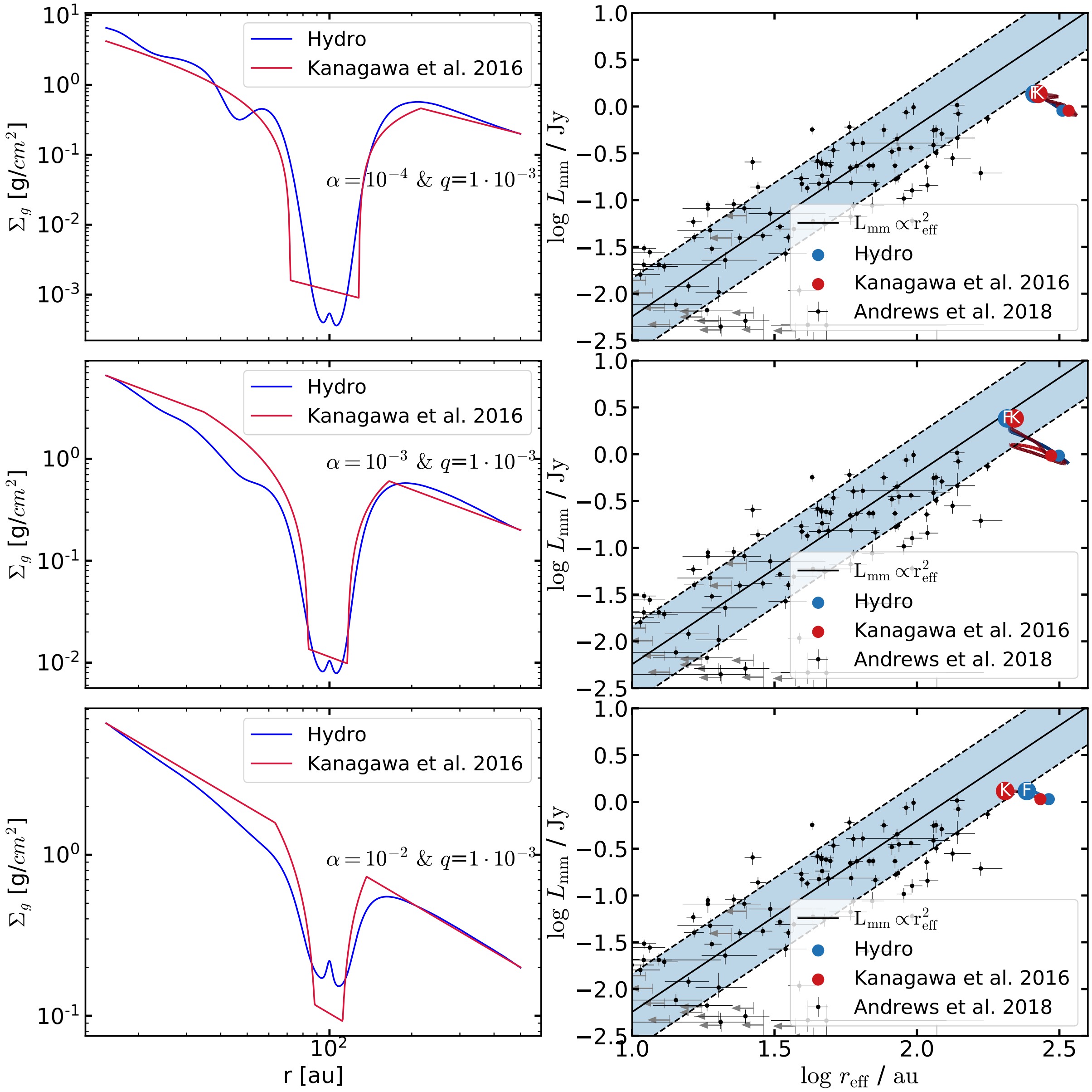

Figure A.6: Comparison between a hydrodynamical and our dust evolution simulation for different α-values and for a planet/star mass ratio $q = 3 \cdot 10^{-3}$ at 100 au. In the left column are the different gap profiles for different α-values and in the right column the corresponding evolution tracks. Even though the profile from Kanagawa et al. (2016) does not overlapping with that obtained from the hydrodynamical simulation, the tracks in the right column produce similar results.

A.4 Additional heat maps

In this section we add the additional heat maps where the 10% porosity (DSHARP-10) and 90% porosity (DSHARP-90) opacity is used. We plot the position of every simulation for three different snapshots (300 kyr, 1 Myr, 3 Myr). For DSHARP-10 (Figure A.7) we obtain similar results to the DSHARP case Figure 5.7 (with no porosity) as the two opacities are similar to one another (see Figure 5.1). For the DSHARP-90 case (Figure A.8), the complete absence of the opacity cliff does not allow a considerable amount of smooth disks to enter the SLR, while the same fraction of substructured disks match, as in the DSHARP-50 Figure 5.8 case.

A.4.1 Changing the stellar luminosity

In Section 5.5.8 we performed a test where we used the luminosity of the star at 3 Myr instead of 1 Myr, which is used throughout this work. Since the stellar luminosity decreases from 1 Myr to 3 Myr, there is an overall movement of disks to lower luminosities that is shown in Figure A.10 in the right panel. In this example we plot the heat map of a case where there is a planet at $1/3 r_c$ at a snapshot of 1 Myr.

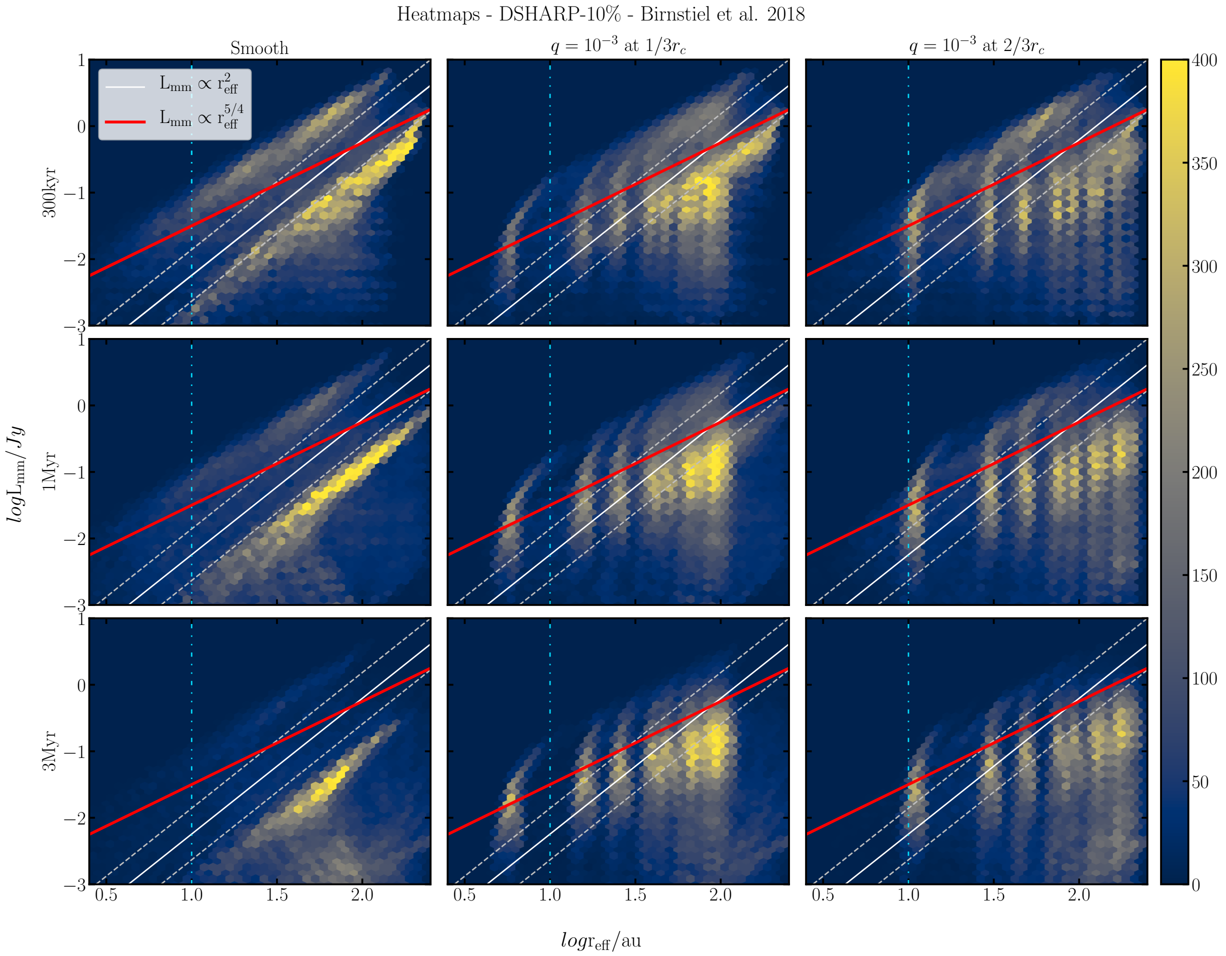

Figure A.7: Heat maps of representative simulations with the Birnstiel et al. (2018) D-10 opacities with 10% porosity. From left to right, the three columns represent the smooth case, a planet at $1/3r_c$, and a planet at $2/3r_c$. From top to bottom, the rows represent three different snapshots at 300 kyr, 1 Myr, and 3 Myr. The white solid line is the SLR from Andrews et al. (2018a) and the red solid line our fit for the cases where we include a planet. The color bar shows the number of simulations in a single cell. The blue dash-dotted line shows the minimum limit ($r_{eff} \sim 10$ au) where observational results are available.

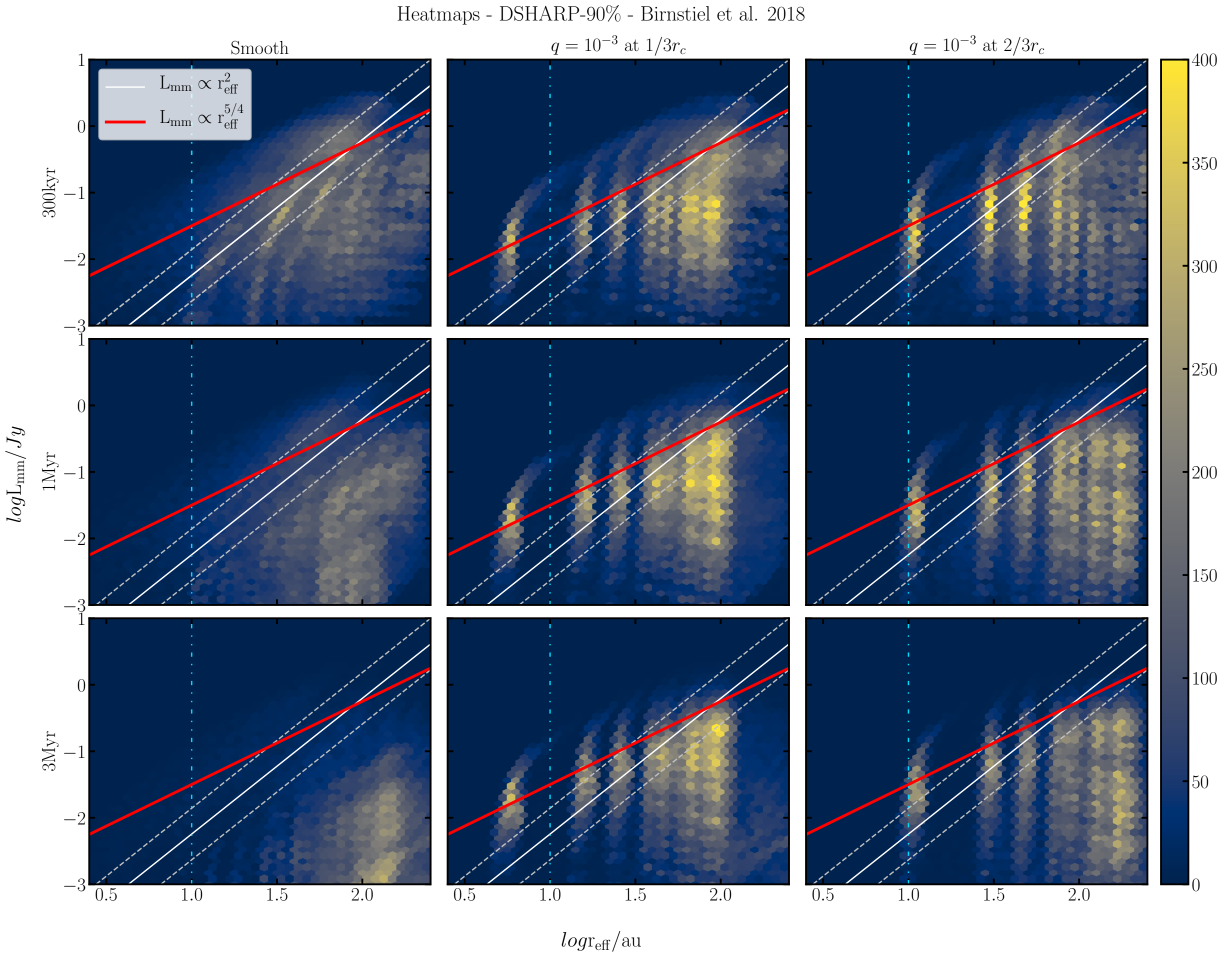

Figure A.8: Heat maps of representative simulations with the Birnstiel et al. (2018) D-90 opacities with 90% porosity. From left to right, the three columns represent the smooth case, a planet at $1/3r_c$, and a planet at $2/3r_c$. From top to bottom, the rows represent three different snapshots at 300 kyr, 1 Myr, and 3 Myr. The white solid line is the SLR from Andrews et al. (2018a) and the red solid line our fit for the cases where we include a planet. The color bar shows the number of simulations in a single cell. The blue dash-dotted line shows the minimum limit ($r_{eff} \sim 10$ au) where observational results are available.

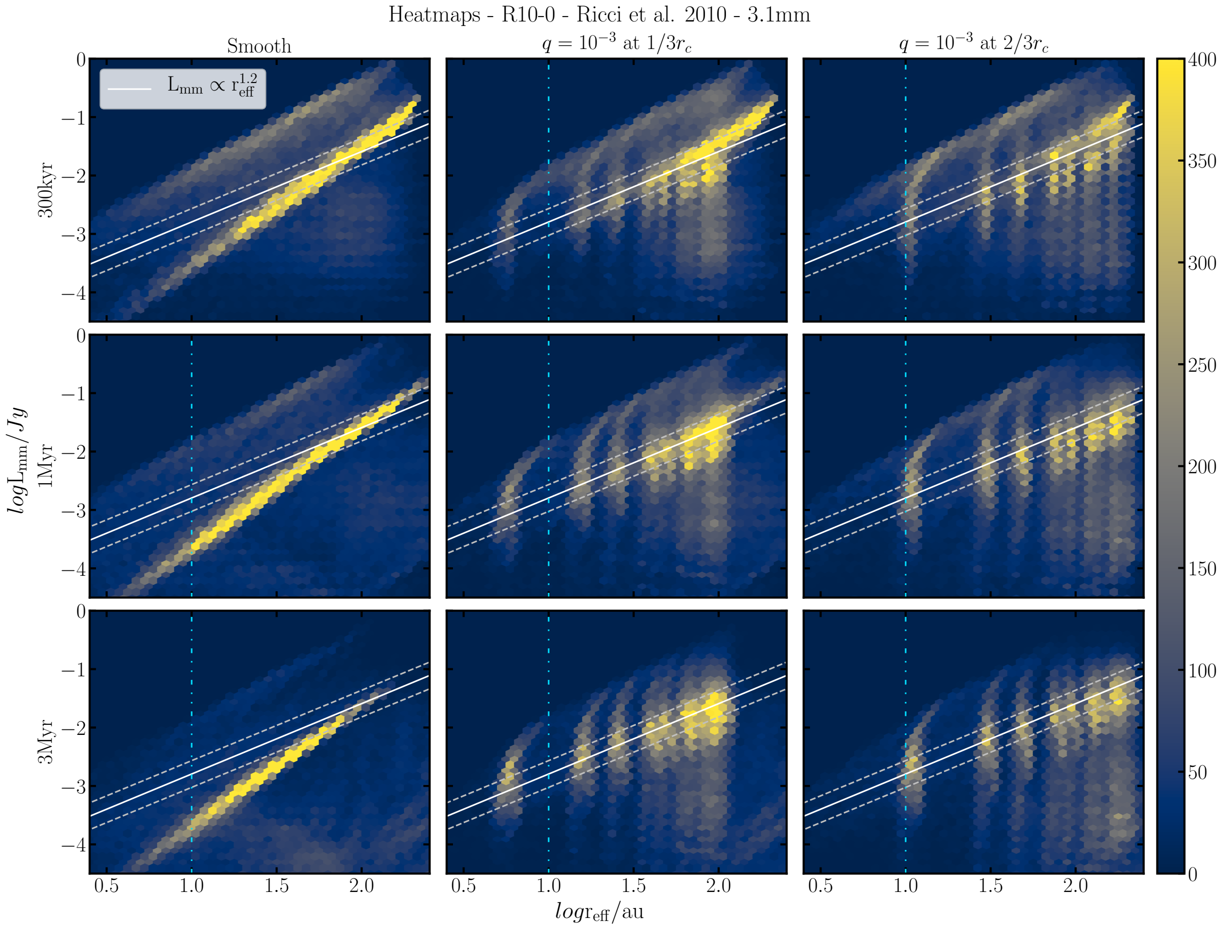

Figure A.9: Heat maps of representative simulations with the R10-0 opacity at 3.1 mm for a direct comparison with Tazzari et al. (2021). From left to right, the three columns represent the smooth case, a planet at $1/3r_c$, and a planet at $2/3r_c$. From top to bottom, the rows represent three different snapshots at 300 kyr, 1 Myr, and 3 Myr. The white solid line is the SLR from Tazzari et al. (2021). The color bar shows the number of simulations in a single cell. The blue dash-dotted line shows the minimum limit ($r_{eff} \sim 10$ au) where observational results are available.

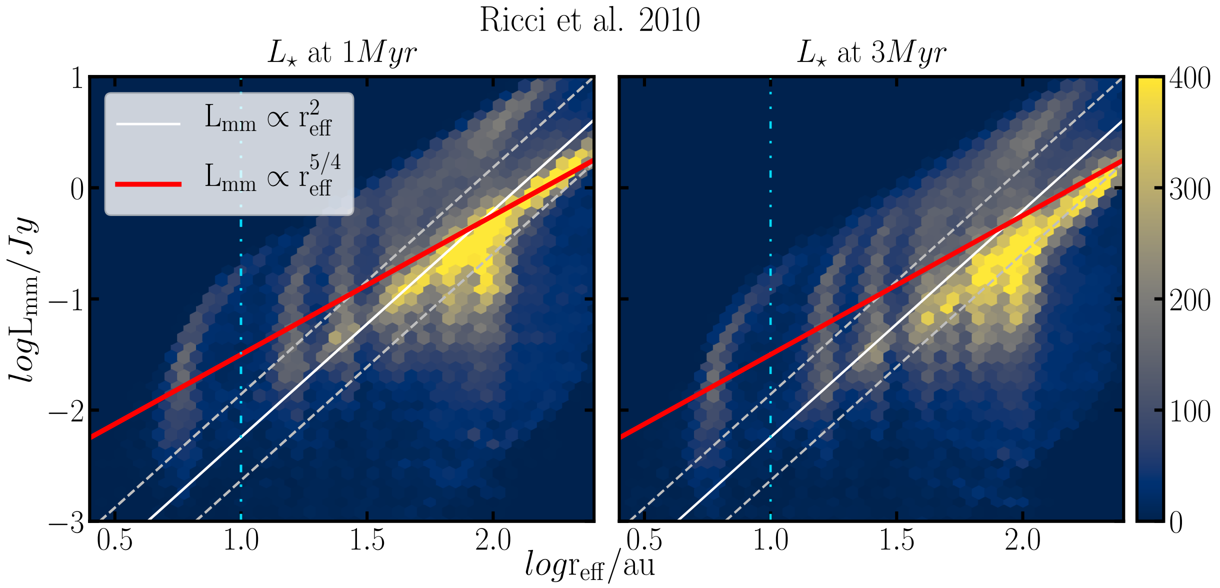

Figure A.10: Heat map comparison between disks where the stellar luminosity at 3 Myr (right panel) is used instead of 1 Myr (left panel). There is an overall shift toward lower luminosities, but the trend remains the same.

List of Acronyms and Abbreviations

Acronym	**Full name**
Instruments	
ALMA	Atacama Large Millimeter/submillimeter Array
JWST	James Webb Space Telescope
VLA	(Karl G. Jansky) Very Large Array
VLT	Very Large Telescope
Other	
DSHARP	Disk Substructures at High Angular Resolution Project
fIR	far-infrared
FLD	Flux Limited Diffusion
GI	Gravitational Instability
HD	Hydrodynamics
IR	infrared
ISM	Interstellar medium
MCMC	Markov chain Monte Carlo
MHD	Magneto-hydrodynamics
MMSN	Minimum Mass Solar Nebula
MRI	Magneto-Rotational Instability
MRN	Mathis-Rumpl-Nordsieck (particle size distribution)
PPD	Proto-Planetary Disk
RT	Radiative Transfer
SI	Streaming Instability
SLR	Size-Luminosity Relation
TD	Transition Disk
SED	Spectral Energy Distribution
VSI	Vertical shear instability
YSO	Young Stellar Object
Software	
MPI	Message Passing Interface
PETSc	Portable Extensible Toolkit for Scientific Computation

List of Astrophysical constants

Name	**Symbol**	**Number**	**CGS-Unit**
Astronomical unit	au	1.496×10^{13}	cm
Boltzmann constant	k	1.381×10^{-16}	$\mathrm{ergK^{-1}}$
Gravitational constant	G	6.67×10^{-8}	$\mathrm{cm^3g^{-1}s^{-2}}$
Earth mass	$\mathrm{M_{\oplus}}$	5.974×10^{27}	g
Hydrogen atom mass	$\mathrm{m_H}$	1.6733×10^{-24}	g
Jupiter mass	$\mathrm{M_j}$	1.899×10^{30}	g
Parsec	pc	3.086×10^{18}	cm
Planck constant	h	6.626×10^{-27}	ergs
Proton mass	$\mathrm{m_H}$	1.6726×10^{-24}	g
Solar mass	$\mathrm{M_{\odot}}$	1.989×10^{33}	g
Solar radius	$\mathrm{R_{\odot}}$	6.963×10^{10}	cm
Speed of light	c	2.998×10^{-10}	$\mathrm{cms^{-1}}$
year	yr	3.1557600×10^{7}	s

List of Publications

van der Marel Nienke, Williams Jonathan P., Picogna Giovanni, van Terwisga Sierk, Facchini Stefano, Manara Carlo F., **Zormpas Apostolos**, Ansdell, Megan, "High-resolution ALMA observations of transition disk candidates in Lupus", arXiv:2204.08225

A. Zormpas, T. Birnstiel, G.P. Rosotti, S.M. Andrews, "A Large Population study of Protoplanetary Disks: Explaining the Size-Luminosity relation with or without sub-structures", Astronomy and Astrophysics (2022), vol. 661, A66

R. Franceschi, T. Birnstiel, T. Henning, P. Pinilla, D. Semenov, **A. Zormpas**, "Mass determination of protoplanetary disks from dust evolution, Astronomy and Astrophysics (2022)", vol. 657, A74

A. Zormpas, Picogna, Ercolano, Kley, "Solid accretion onto planetary cores in radiative disks", Astronomy and Astrophysics (2020), vol. 638, A97

Bibliography

Akiyama, E., Hashimoto, J., Liu, H. B., et al. 2016, Spiral Structure and Differential Dust Size Distribution in the LKHα 330 Disk, *Astronomical Journal*, **152**:222

Alibert, Y., Venturini, J., Helled, R., et al. 2018, The formation of Jupiter by hybrid pebble-planetesimal accretion, *Nature Astronomy*, **2**:873–877

ALMA Partnership, Brogan, C. L., Pérez, L. M., et al. 2015, The 2014 ALMA Long Baseline Campaign: First Results from High Angular Resolution Observations toward the HL Tau Region, *The Astrophysical Journal Letters*, **808**:L3

Andrews, S. M. 2020, Observations of Protoplanetary Disk Structures, *Annual Review of Astronomy and Astrophysics*, **58**:483–528

Andrews, S. M., Rosenfeld, K. A., Kraus, A. L., & Wilner, D. J. 2013, The Mass Dependence between Protoplanetary Disks and their Stellar Hosts, *The Astrophysical Journal*, **771**:129

Andrews, S. M., Rosenfeld, K. A., Wilner, D. J., & Bremer, M. 2011, A Closer Look at the LkCa 15 Protoplanetary Disk, *The Astrophysical Journal Letters*, **742**:L5

Andrews, S. M., Terrell, M., Tripathi, A., et al. 2018a, Scaling Relations Associated with Millimeter Continuum Sizes in Protoplanetary Disks, *The Astrophysical Journal*, **865**:157

Andrews, S. M., Wilner, D. J., Hughes, A. M., Qi, C., & Dullemond, C. P. 2010, Protoplanetary Disk Structures in Ophiuchus. II. Extension to Fainter Sources, *The Astrophysical Journal*, **723**:1241–1254

Andrews, S. M., Wilner, D. J., Hughes, A. M., et al. 2012, The TW Hya Disk at 870 μm: Comparison of CO and Dust Radial Structures, *The Astrophysical Journal*, **744**:162

Andrews, S. M., Wilner, D. J., Zhu, Z., et al. 2016, Ringed Substructure and a Gap at 1 au in the Nearest Protoplanetary Disk, *The Astrophysical Journal Letters*, **820**:L40

Andrews, S. M., Huang, J., Pérez, L. M., et al. 2018b, The Disk Substructures at High Angular Resolution Project (DSHARP). I. Motivation, Sample, Calibration, and Overview, *The Astrophysical Journal Letters*, **869**:L41

Ansdell, M., Williams, J. P., Manara, C. F., et al. 2017, An ALMA Survey of Protoplanetary Disks in the σ Orionis Cluster, *Astronomical Journal*, **153**:240

Ansdell, M., Williams, J. P., van der Marel, N., et al. 2016, ALMA Survey of Lupus Protoplanetary Disks. I. Dust and Gas Masses, *The Astrophysical Journal*, **828**:46

Ansdell, M., Williams, J. P., Trapman, L., et al. 2018, ALMA Survey of Lupus Protoplanetary Disks. II. Gas Disk Radii, *The Astrophysical Journal*, **859**:21

Armitage, P. J. 2010, Astrophysics of Planet Formation

Ataiee, S., Baruteau, C., Alibert, Y., & Benz, W. 2018, How much does turbulence change the pebble isolation mass for planet formation?, *Astronomy and Astrophysics*, **615**:A110

Ayliffe, B. A., Laibe, G., Price, D. J., & Bate, M. R. 2012, On the accumulation of planetesimals near disc gaps created by protoplanets, *Monthly Notices of the Royal Astronomical Society*, **423**:1450–1462

Balbus, S. A., & Hawley, J. F. 1991, A Powerful Local Shear Instability in Weakly Magnetized Disks. I. Linear Analysis, *The Astrophysical Journal*, **376**:214

Ballering, N. P., & Eisner, J. A. 2019, Protoplanetary Disk Masses from Radiative Transfer Modeling: A Case Study in Taurus, *Astronomical Journal*, **157**:144

Barenfeld, S. A., Carpenter, J. M., Ricci, L., & Isella, A. 2016, ALMA Observations of Circumstellar Disks in the Upper Scorpius OB Association, *The Astrophysical Journal*, **827**:142

Beckwith, S. V. W., Sargent, A. I., Chini, R. S., & Guesten, R. 1990, A Survey for Circumstellar Disks around Young Stellar Objects, *Astronomical Journal*, **99**:924

Bell, C. P. M., Naylor, T., Mayne, N. J., Jeffries, R. D., & Littlefair, S. P. 2013, Pre-main-sequence isochrones - II. Revising star and planet formation time-scales, *Monthly Notices of the Royal Astronomical Society*, **434**:806–831

Benítez Llambay, P., & Masset, F. 2015, FARGO3D: Hydrodynamics/magnetohydrodynamics code

Benz, W., Ida, S., Alibert, Y., Lin, D., & Mordasini, C. 2014, Planet Population Synthesis, in *Protostars and Planets VI, ed. H. Beuther, R. S. Klessen, C. P. Dullemond, & T. Henning*, p. 691

Bergin, E. A., Cleeves, L. I., Gorti, U., et al. 2013, An old disk still capable of forming a planetary system, *Nature*, **493**:644–646

Béthune, W. 2019, Self-gravitating planetary envelopes and the core-nucleated instability, *Monthly Notices of the Royal Astronomical Society*, **490**:3144–3157

Birnstiel, T., & Andrews, S. M. 2014, On the Outer Edges of Protoplanetary Dust Disks, *The Astrophysical Journal*, **780**:153

Birnstiel, T., Andrews, S. M., Pinilla, P., & Kama, M. 2015, Dust Evolution Can Produce Scattered Light Gaps in Protoplanetary Disks, *The Astrophysical Journal Letters*, **813**:L14

Birnstiel, T., Dullemond, C. P., & Brauer, F. 2009, Dust retention in protoplanetary disks, *Astronomy and Astrophysics*, **503**:L5–L8

Birnstiel, T., Dullemond, C. P., & Brauer, F. 2010, Gas- and dust evolution in protoplanetary disks, *Astronomy and Astrophysics*, **513**:A79

Birnstiel, T., Klahr, H., & Ercolano, B. 2012, A simple model for the evolution of the dust population in protoplanetary disks, *Astronomy and Astrophysics*, **539**:A148

Birnstiel, T., Ormel, C. W., & Dullemond, C. P. 2011, Dust size distributions in coagulation/fragmentation equilibrium: numerical solutions and analytical fits, *Astronomy and Astrophysics*, **525**:A11

Birnstiel, T., Dullemond, C. P., Zhu, Z., et al. 2018, The Disk Substructures at High Angular Resolution Project (DSHARP). V. Interpreting ALMA Maps of Protoplanetary Disks in Terms of a Dust Model, *The Astrophysical Journal Letters*, **869**:L45

Bitsch, B., Morbidelli, A., Johansen, A., et al. 2018, Pebble-isolation mass: Scaling law and implications for the formation of super-Earths and gas giants, *Astronomy & Astrophysics*, **612**:A30

Blum, J. 2018a, Dust Evolution in Protoplanetary Discs and the Formation of Planetesimals. What Have We Learned from Laboratory Experiments?, *Space Science Reviews*, **214**:52

Blum, J. 2018b, Dust Evolution in Protoplanetary Discs and the Formation of Planetesimals. What Have We Learned from Laboratory Experiments?, *Space Science Reviews*, **214**:52

Blum, J., & Wurm, G. 2000, Experiments on Sticking, Restructuring, and Fragmentation of Preplanetary Dust Aggregates, *Icarus*, **143**:138–146

Blum, J., & Wurm, G. 2008, The growth mechanisms of macroscopic bodies in protoplanetary disks., *Annual Review of Astronomy and Astrophysics*, **46**:21–56

Blum, J., Gundlach, B., Krause, M., et al. 2017, Evidence for the formation of comet 67P/Churyumov-Gerasimenko through gravitational collapse of a bound clump of pebbles, *Monthly Notices of the Royal Astronomical Society*, **469**:S755–S773

Boehler, Y., Ricci, L., Weaver, E., et al. 2018, The Complex Morphology of the Young Disk MWC 758: Spirals and Dust Clumps around a Large Cavity, *The Astrophysical Journal*, **853**:162

Bohlin, R. C., Savage, B. D., & Drake, J. F. 1978, A survey of interstellar H I from Lalpha absorption measurements. II., *The Astrophysical Journal*, **224**:132–142

Booth, A. S., Walsh, C., Ilee, J. D., et al. 2019, The First Detection of $^{13}C^{17}O$ in a Protoplanetary Disk: A Robust Tracer of Disk Gas Mass, *The Astrophysical Journal Letters*, **882**:L31

Boss, A. P. 1997, Giant planet formation by gravitational instability., *Science*, **276**:1836–1839

Brauer, F., Dullemond, C. P., & Henning, T. 2008, Coagulation, fragmentation and radial motion of solid particles in protoplanetary disks, *Astronomy and Astrophysics*, **480**:859–877

Brouwers, M. G., & Ormel, C. W. 2019, How planets grow by pebble accretion II: Analytical calculations on the evolution of polluted envelopes, *arXiv e-prints*, p. arXiv:1908.02742

Cameron, A. G. W. 1978, Physics of the Primitive Solar Accretion Disk, *Moon and Planets*, **18**:5–40

Carney, M. T., Fedele, D., Hogerheijde, M. R., et al. 2018, Probing midplane CO abundance and gas temperature with DCO^+ in the protoplanetary disk around HD 169142, *Astronomy and Astrophysics*, **614**:A106

Carrera, D., Davies, M. B., & Johansen, A. 2016, Survival of habitable planets in unstable planetary systems, *Monthly Notices of the Royal Astronomical Society*, **463**:3226–3238

Casassus, S., van der Plas, G. M., Perez, S., et al. 2013, Flows of gas through a protoplanetary gap, *Nature*, **493**:191–194

Cassan, A., Kubas, D., Beaulieu, J. P., et al. 2012, One or more bound planets per Milky Way star from microlensing observations, *Nature*, **481**:167–169

Chiang, E. I., & Goldreich, P. 1997, Spectral Energy Distributions of T Tauri Stars with Passive Circumstellar Disks, *The Astrophysical Journal*, **490**:368–376

Cleeves, L. I., Öberg, K. I., Wilner, D. J., et al. 2016, The Coupled Physical Structure of Gas and Dust in the IM Lup Protoplanetary Disk, *The Astrophysical Journal*, **832**:110

Cumming, A., Butler, R. P., Marcy, G. W., et al. 2008, The Keck planet search: detectability and the minimum mass and orbital period distribution of extrasolar planets, *Publications of the Astronomical Society of the Pacific*, **120**:531

D'Alessio, P., Calvet, N., & Hartmann, L. 1997, The Structure and Emission of Accretion Disks Irradiated by Infalling Envelopes, *The Astrophysical Journal*, **474**:397–406

D'Alessio, P., Cantö, J., Calvet, N., & Lizano, S. 1998, Accretion Disks around Young Objects. I. The Detailed Vertical Structure, *The Astrophysical Journal*, **500**:411–427

Dipierro, G., & Laibe, G. 2017, An opening criterion for dust gaps in protoplanetary discs, *Monthly Notices of the Royal Astronomical Society*, **469**:1932–1948

Dong, R., Zhu, Z., & Whitney, B. 2015, Observational Signatures of Planets in Protoplanetary Disks I. Gaps Opened by Single and Multiple Young Planets in Disks, *The Astrophysical Journal*, **809**:93

Dong, S., & Zhu, Z. 2013, Fast Rise of "Neptune-size" Planets (4-8 R $_{\oplus}$) from P $\sim$10 to $\sim$250 Days—Statistics of Kepler Planet Candidates up to $\sim$0.75 AU, *The Astrophysical Journal*, **778**:53

Drążkowska, J., Li, S., Birnstiel, T., Stammler, S. M., & Li, H. 2019, Including Dust Coagulation in Hydrodynamic Models of Protoplanetary Disks: Dust Evolution in the Vicinity of a Jupiter-mass Planet, *The Astrophysical Journal*, **885**:91

Drazkowska, J., Bitsch, B., Lambrechts, M., et al. 2022, Planet Formation Theory in the Era of ALMA and Kepler: from Pebbles to Exoplanets, *arXiv e-prints*, p. arXiv:2203.09759

Dullemond, C. P., Hollenbach, D., Kamp, I., & D'Alessio, P. 2007, Models of the Structure and Evolution of Protoplanetary Disks, in *Protostars and Planets V, ed. B. Reipurth, D. Jewitt, & K. Keil*, p. 555

Dullemond, C. P., Birnstiel, T., Huang, J., et al. 2018, The Disk Substructures at High Angular Resolution Project (DSHARP). VI. Dust Trapping in Thin-ringed Protoplanetary Disks, *The Astrophysical Journal Letters*, **869**:L46

Espaillat, C., Muzerolle, J., Najita, J., et al. 2014, An Observational Perspective of Transitional Disks, in *Protostars and Planets VI, ed. H. Beuther, R. S. Klessen, C. P. Dullemond, & T. Henning*, p. 497

Facchini, S., Birnstiel, T., Bruderer, S., & van Dishoeck, E. F. 2017, Different dust and gas radial extents in protoplanetary disks: consistent models of grain growth and CO emission, *Astronomy and Astrophysics*, **605**:A16

Facchini, S., van Dishoeck, E. F., Manara, C. F., et al. 2019, High gas-to-dust size ratio indicating efficient radial drift in the mm-faint CX Tauri disk, *Astronomy and Astrophysics*, **626**:L2

Fedele, D., Carney, M., Hogerheijde, M. R., et al. 2017, ALMA unveils rings and gaps in the protoplanetary system HD 169142: signatures of two giant protoplanets, *Astronomy and Astrophysics*, **600**:A72

Fedele, D., Tazzari, M., Booth, R., et al. 2018, ALMA continuum observations of the protoplanetary disk AS 209. Evidence of multiple gaps opened by a single planet, *Astronomy and Astrophysics*, **610**:A24

Flaherty, K. M., Hughes, A. M., Teague, R., et al. 2018, Turbulence in the TW Hya Disk, *The Astrophysical Journal*, **856**:117

Franceschi, R., Birnstiel, T., Henning, T., et al. 2022, Mass determination of protoplanetary disks from dust evolution, *Astronomy and Astrophysics*, **657**:A74

Fressin, F., Torres, G., Charbonneau, D., et al. 2013, The False Positive Rate of Kepler and the Occurrence of Planets, *The Astrophysical Journal*, **766**:81

Gammie, C. F. 1996, Layered Accretion in T Tauri Disks, *The Astrophysical Journal*, **457**:355

Gárate, M., Birnstiel, T., Drążkowska, J., & Stammler, S. M. 2020, Gas accretion damped by dust back-reaction at the snow line, *Astronomy and Astrophysics*, **635**:A149

Gillon, M., Triaud, A. H. M. J., Demory, B.-O., et al. 2017, Seven temperate terrestrial planets around the nearby ultracool dwarf star TRAPPIST-1, *Nature*, **542**:456–460

Grady, C. A., Muto, T., Hashimoto, J., et al. 2013, Spiral Arms in the Asymmetrically Illuminated Disk of MWC 758 and Constraints on Giant Planets, *The Astrophysical Journal*, **762**:48

Guillot, T., Ida, S., & Ormel, C. W. 2014, On the filtering and processing of dust by planetesimals. I. Derivation of collision probabilities for non-drifting planetesimals, *Astronomy and Astrophysics*, **572**:A72

Gundlach, B., & Blum, J. 2015, The Stickiness of Micrometer-sized Water-ice Particles, *The Astrophysical Journal*, **798**:34

Güttler, C., Blum, J., Zsom, A., Ormel, C. W., & Dullemond, C. P. 2010a, The outcome of protoplanetary dust growth: pebbles, boulders, or planetesimals?. I. Mapping the zoo of laboratory collision experiments, *Astronomy and Astrophysics*, **513**:A56

Güttler, C., Blum, J., Zsom, A., Ormel, C. W., & Dullemond, C. P. 2010b, The outcome of protoplanetary dust growth: pebbles, boulders, or planetesimals?. I. Mapping the zoo of laboratory collision experiments, *Astronomy and Astrophysics*, **513**:A56

Haisch, Karl E., J., Lada, E. A., & Lada, C. J. 2001, Disk Frequencies and Lifetimes in Young Clusters, *The Astrophysical Journal Letters*, **553**:L153–L156

Hayashi, C. 1981, Structure of the Solar Nebula, Growth and Decay of Magnetic Fields and Effects of Magnetic and Turbulent Viscosities on the Nebula, *Progress of Theoretical Physics Supplement*, **70**:35–53

Heese, S., Wolf, S., Dutrey, A., & Guilloteau, S. 2017, Spread of the dust temperature distribution in circumstellar disks, *Astronomy and Astrophysics*, **604**:A5

Hendler, N., Pascucci, I., Pinilla, P., et al. 2020, The Evolution of Dust Disk Sizes from a Homogeneous Analysis of 1-10 Myr old Stars, *The Astrophysical Journal*, **895**:126

Hendler, N. P., Mulders, G. D., Pascucci, I., et al. 2017, Hints for Small Disks around Very Low Mass Stars and Brown Dwarfs, *The Astrophysical Journal*, **841**:116

Henning, T., & Stognienko, R. 1996, Dust opacities for protoplanetary accretion disks: influence of dust aggregates., *Astronomy and Astrophysics*, **311**:291–303

Hildebrand, R. H. 1983, The determination of cloud masses and dust characteristics from submillimetre thermal emission., *Astronomy and Geophysics*, **24**:267–282

Howard, A. W., Marcy, G. W., Bryson, S. T., et al. 2012, Planet Occurrence within 0.25 AU of Solar-type Stars from Kepler, *Astrophysical Journal Supplement Series*, **201**:15

Huang, J., Andrews, S. M., Dullemond, C. P., et al. 2018a, The Disk Substructures at High Angular Resolution Project (DSHARP). II. Characteristics of Annular Substructures, *The Astrophysical Journal Letters*, **869**:L42

Huang, J., Andrews, S. M., Pérez, L. M., et al. 2018b, The Disk Substructures at High Angular Resolution Project (DSHARP). III. Spiral Structures in the Millimeter Continuum of the Elias 27, IM Lup, and WaOph 6 Disks, *The Astrophysical Journal Letters*, **869**:L43

Ikoma, M., Nakazawa, K., & Emori, H. 2000, Formation of Giant Planets: Dependences on Core Accretion Rate and Grain Opacity, *The Astrophysical Journal*, **537**:1013–1025

Isella, A., Pérez, L. M., & Carpenter, J. M. 2012, On the Nature of the Transition Disk around LkCa 15, *The Astrophysical Journal*, **747**:136

Isella, A., Guidi, G., Testi, L., et al. 2016, Ringed Structures of the HD 163296 Protoplanetary Disk Revealed by ALMA, *Physical Review Letters,*, **117**:251101

Isella, A., Huang, J., Andrews, S. M., et al. 2018, The Disk Substructures at High Angular Resolution Project (DSHARP). IX. A High-definition Study of the HD 163296 Planet-forming Disk, *The Astrophysical Journal Letters*, **869**:L49

Johansen, A., Blum, J., Tanaka, H., et al. 2014, The Multifaceted Planetesimal Formation Process, *Protostars and Planets VI*, pp. 547–570

Johansen, A., & Lambrechts, M. 2017, Forming Planets via Pebble Accretion, *Annual Review of Earth and Planetary Sciences*, **45**:359–387

Johansen, A., Oishi, J. S., Mac Low, M.-M., et al. 2007, Rapid planetesimal formation in turbulent circumstellar disks, *Nature*, **448**:1022–1025

Kama, M., Trapman, L., Fedele, D., et al. 2020, Mass constraints for 15 protoplanetary discs from HD 1-0, *Astronomy and Astrophysics*, **634**:A88

Kanagawa, K. D., Muto, T., Okuzumi, S., et al. 2018, Impacts of Dust Feedback on a Dust Ring Induced by a Planet in a Protoplanetary Disk, *The Astrophysical Journal*, **868**:48

Kanagawa, K. D., Muto, T., Tanaka, H., et al. 2016, Mass constraint for a planet in a protoplanetary disk from the gap width, *Publications of the Astronomical Society of Japan*, **68**:43

Kataoka, A., Okuzumi, S., Tanaka, H., & Nomura, H. 2014, Opacity of fluffy dust aggregates, *Astronomy and Astrophysics*, **568**:A42

Kenyon, S. J., & Hartmann, L. 1987, Spectral Energy Distributions of T Tauri Stars: Disk Flaring and Limits on Accretion, *The Astrophysical Journal*, **323**:714

Kenyon, S. J., Yi, I., & Hartmann, L. 1996, A Magnetic Accretion Disk Model for the Infrared Excesses of T Tauri Stars, *The Astrophysical Journal*, **462**:439

Klahr, H., & Bodenheimer, P. 2006, Formation of Giant Planets by Concurrent Accretion of Solids and Gas inside an Anticyclonic Vortex, *The Astrophysical Journal*, **639**:432–440

Klahr, H., & Kley, W. 2006, 3D-radiation hydro simulations of disk-planet interactions-I. Numerical algorithm and test cases, *Astronomy & Astrophysics*, **445**:747–758

Klahr, H., & Schreiber, A. 2020, Turbulence Sets the Length Scale for Planetesimal Formation: Local 2D Simulations of Streaming Instability and Planetesimal Formation, *The Astrophysical Journal*, **901**:54

Kley, W. 1989, Radiation hydrodynamics of the boundary layer in accretion disks. I - Numerical methods, *Astronomy and Astrophysics*, **208**:98–110

Kley, W., Bitsch, B., & Klahr, H. 2009, Planet migration in three-dimensional radiative discs, *Astronomy and Astrophysics*, **506**:971–987

Kokubo, E., & Ida, S. 1996, On Runaway Growth of Planetesimals, *Icarus*, **123**:180–191

Kolb, S. M., Stute, M., Kley, W., & Mignone, A. 2013, Radiation hydrodynamics integrated in the PLUTO code, *Astronomy & Astrophysics*, **559**:A80

Kratter, K., & Lodato, G. 2016, Gravitational Instabilities in Circumstellar Disks, *Annual Review of Astronomy and Astrophysics*, **54**:271–311

Kraus, S., Kreplin, A., Fukugawa, M., et al. 2017, Dust-trapping Vortices and a Potentially Planet-triggered Spiral Wake in the Pre-transitional Disk of V1247 Orionis, *The Astrophysical Journal Letters*, **848**:L11

Krijt, S., Ormel, C. W., Dominik, C., & Tielens, A. G. G. M. 2016, A panoptic model for planetesimal formation and pebble delivery, *Astronomy and Astrophysics*, **586**:A20

Kuiper, G. P. 1951, On the Origin of the Solar System, *Proceedings of the National Academy of Science*, **37**:1–14

Lada, C. J. 1987, Star formation: from OB associations to protostars., in *Star Forming Regions, ed. M. Peimbert & J. Jugaku, Vol. 115*, p. 1

Lada, C. J., & Wilking, B. A. 1984, The nature of the embedded population in the rho Ophiuchi dark cloud : mid-infrared observations., *The Astrophysical Journal*, **287**:610–621

Lambrechts, M., & Johansen, A. 2012, Rapid growth of gas-giant cores by pebble accretion, *Astronomy and Astrophysics*, **544**:A32

Lambrechts, M., & Johansen, A. 2014, Forming the cores of giant planets from the radial pebble flux in protoplanetary discs, *Astronomy & Astrophysics*, **572**:A107

Lambrechts, M., Johansen, A., & Morbidelli, A. 2014, Separating gas-giant and ice-giant planets by halting pebble accretion, *Astronomy & Astrophysics*, **572**:A35

Levison, H. F., Thommes, E., & Duncan, M. J. 2010, Modeling the Formation of Giant Planet Cores. I. Evaluating Key Processes, *Astronomical Journal*, **139**:1297–1314

Li, R., & Youdin, A. N. 2021, Thresholds for Particle Clumping by the Streaming Instability, *The Astrophysical Journal*, **919**:107

Lin, D. N. C., & Papaloizou, J. C. B. 1993, On the Tidal Interaction Between Protostellar Disks and Companions, in *Protostars and Planets III, ed. E. H. Levy & J. I. Lunine*, p. 749

Lin, D. N. C., & Pringle, J. E. 1987, A viscosity prescription for a self-gravitating accretion disc, *Monthly Notices of the Royal Astronomical Society*, **225**:607–613

Lissauer, J. J., & Stewart, G. R. 1993, Growth of Planets from Planetesimals, in *Protostars and Planets III, ed. E. H. Levy & J. I. Lunine*, p. 1061

Long, F., Pinilla, P., Herczeg, G. J., et al. 2018, Gaps and Rings in an ALMA Survey of Disks in the Taurus Star-forming Region, *The Astrophysical Journal*, **869**:17

Long, F., Herczeg, G. J., Harsono, D., et al. 2019, Compact Disks in a High-resolution ALMA Survey of Dust Structures in the Taurus Molecular Cloud, *The Astrophysical Journal*, **882**:49

Lovelace, R. V. E., Li, H., Colgate, S. A., & Nelson, A. F. 1999, Rossby Wave Instability of Keplerian Accretion Disks, *The Astrophysical Journal*, **513**:805–810

Lynden-Bell, D., & Pringle, J. E. 1974a, The evolution of viscous discs and the origin of the nebular variables., *Monthly Notices of the Royal Astronomical Society*, **168**:603–637

Lynden-Bell, D., & Pringle, J. E. 1974b, The evolution of viscous discs and the origin of the nebular variables., *Monthly Notices of the Royal Astronomical Society*, **168**:603–637

Mamajek, E. E. 2009, Initial Conditions of Planet Formation: Lifetimes of Primordial Disks, in *American Institute of Physics Conference Series, Vol. 1158, Exoplanets and Disks: Their Formation and Diversity, ed. T. Usuda, M. Tamura, & M. Ishii*, pp. 3–10

Manara, C. F., Rosotti, G., Testi, L., et al. 2016, Evidence for a correlation between mass accretion rates onto young stars and the mass of their protoplanetary disks, *Astronomy and Astrophysics*, **591**:L3

Manara, C. F., Tazzari, M., Long, F., et al. 2019, Observational constraints on dust disk sizes in tidally truncated protoplanetary disks in multiple systems in the Taurus region, *Astronomy and Astrophysics*, **628**:A95

Marino, S., Perez, S., & Casassus, S. 2015, Shadows Cast by a Warp in the HD 142527 Protoplanetary Disk, *The Astrophysical Journal Letters*, **798**:L44

Mathis, J. S., Rumpl, W., & Nordsieck, K. H. 1977, The size distribution of interstellar grains., *The Astrophysical Journal*, **217**:425–433

Maury, A. J., André, P., Men'shchikov, A., Könyves, V., & Bontemps, S. 2011, The formation of active protoclusters in the Aquila rift: a millimeter continuum view, *Astronomy and Astrophysics*, **535**:A77

Mayer, L., Quinn, T., Wadsley, J., & Stadel, J. 2002, Formation of Giant Planets by Fragmentation of Protoplanetary Disks, *Science*, **298**:1756–1759

Mayor, M., & Queloz, D. 1995, A Jupiter-mass companion to a solar-type star, *Nature*, **378**:355–359

Mayor, M., Marmier, M., Lovis, C., et al. 2011, The HARPS search for southern extra-solar planets XXXIV. Occurrence, mass distribution and orbital properties of super-Earths and Neptune-mass planets, *arXiv e-prints*, p. arXiv:1109.2497

Mignone, A., Bodo, G., Massaglia, S., et al. 2007, PLUTO: a numerical code for computational astrophysics, *The Astrophysical Journal Supplement Series*, **170**:228

Min, M., Rab, C., Woitke, P., Dominik, C., & Ménard, F. 2016, Multiwavelength optical properties of compact dust aggregates in protoplanetary disks, *Astronomy and Astrophysics*, **585**:A13

Miotello, A., Kamp, I., Birnstiel, T., Cleeves, L. I., & Kataoka, A. 2022, Setting the Stage for Planet Formation: Measurements and Implications of the Fundamental Disk Properties, *arXiv e-prints*, p. arXiv:2203.09818

Miotello, A., van Dishoeck, E. F., Kama, M., & Bruderer, S. 2016, Determining protoplanetary disk gas masses from CO isotopologues line observations, *Astronomy and Astrophysics*, **594**:A85

Miyake, K., & Nakagawa, Y. 1993, Effects of Particle Size Distribution on Opacity Curves of Protoplanetary Disks around T Tauri Stars, *Icarus*, **106**:20–41

Mizuno, H. 1980, Formation of the giant planets, *Progress of Theoretical Physics*, **64**:544–557

Mizuno, H. 1980, Formation of the Giant Planets, *Progress of Theoretical Physics*, **64**:544–557

Morbidelli, A., & Nesvorny, D. 2012, Dynamics of pebbles in the vicinity of a growing planetary embryo: hydro-dynamical simulations, *Astronomy and Astrophysics*, **546**:A18

Morbidelli, A., & Raymond, S. N. 2016, Challenges in planet formation, *Journal of Geophysical Research (Planets)*, **121**:1962–1980

Mordasini, C. 2014, Grain opacity and the bulk composition of extrasolar planets. II. An analytical model for grain opacity in protoplanetary atmospheres, *Astronomy and Astrophysics*, **572**:A118

Mulders, G. D., Pascucci, I., Apai, D., & Ciesla, F. J. 2018, The Exoplanet Population Observation Simulator. I. The Inner Edges of Planetary Systems, *Astronomical Journal*, **156**:24

Muto, T., Grady, C. A., Hashimoto, J., et al. 2012, Discovery of Small-scale Spiral Structures in the Disk of SAO 206462 (HD 135344B): Implications for the Physical State of the Disk from Spiral Density Wave Theory, *The Astrophysical Journal Letters*, **748**:L22

Nakagawa, Y., Sekiya, M., & Hayashi, C. 1986, Settling and growth of dust particles in a laminar phase of a low-mass solar nebula, *Icarus*, **67**:375–390

Natta, A. 1993, The Temperature Profile of T Tauri Disks, *The Astrophysical Journal*, **412**:761

Natta, A., Testi, L., Calvet, N., et al. 2007, Dust in Protoplanetary Disks: Properties and Evolution, in *Protostars and Planets V, ed. B. Reipurth, D. Jewitt, & K. Keil*, p. 767

Nelson, R. P., Gressel, O., & Umurhan, O. M. 2013, Linear and non-linear evolution of the vertical shear instability in accretion discs, *Monthly Notices of the Royal Astronomical Society*, **435**:2610–2632

Nesvorný, D., & Vokrouhlický, D. 2019, Binary survival in the outer solar system, *Icarus*, **331**:49–61

Okuzumi, S., Tanaka, H., & Sakagami, M.-a. 2009, Numerical Modeling of the Coagulation and Porosity Evolution of Dust Aggregates, *The Astrophysical Journal*, **707**:1247–1263

Ormel, C. W. 2014, An Atmospheric Structure Equation for Grain Growth, *The Astrophysical Journal Letters*, **789**:L18

Ormel, C. W. 2017, The Emerging Paradigm of Pebble Accretion, in *Astrophysics and Space Science Library, Vol. 445, Formation, Evolution, and Dynamics of Young Solar Systems, ed. M. Pessah & O. Gressel*, p. 197

Ormel, C. W., & Klahr, H. H. 2010, The effect of gas drag on the growth of protoplanets. Analytical expressions for the accretion of small bodies in laminar disks, *Astronomy and Astrophysics*, **520**:A43

Paardekooper, S. J., & Mellema, G. 2006, Dust flow in gas disks in the presence of embedded planets, *Astronomy and Astrophysics*, **453**:1129–1140

Pascucci, I., Testi, L., Herczeg, G. J., et al. 2016, A Steeper than Linear Disk Mass-Stellar Mass Scaling Relation, *The Astrophysical Journal*, **831**:125

Pérez, L. M., Carpenter, J. M., Andrews, S. M., et al. 2016a, Spiral density waves in a young protoplanetary disk, *Science*, **353**:1519–1521

Pérez, L. M., Carpenter, J. M., Andrews, S. M., et al. 2016b, Spiral density waves in a young protoplanetary disk, *Science*, **353**:1519–1521

Pérez, L. M., Benisty, M., Andrews, S. M., et al. 2018, The Disk Substructures at High Angular Resolution Project (DSHARP). X. Multiple Rings, a Misaligned Inner Disk, and a Bright Arc in the Disk around the T Tauri star HD 143006, *The Astrophysical Journal Letters*, **869**:L50

Perri, F., & Cameron, A. G. 1974, Hydrodynamic instability of the solar nebula in the presence of a planetary core, *Icarus*, **22**:416–425

Pfalzner, S., Steinhausen, M., & Menten, K. 2014, Short Dissipation Times of Proto-planetary Disks: An Artifact of Selection Effects?, *The Astrophysical Journal Letters*, **793**:L34

Picogna, G., Stoll, M. H. R., & Kley, W. 2018, Particle accretion onto planets in discs with hydrodynamic turbulence, *Astronomy and Astrophysics*, **616**:A116

Piétu, V., Guilloteau, S., Di Folco, E., Dutrey, A., & Boehler, Y. 2014, Faint disks around classical T Tauri stars: Small but dense enough to form planets, *Astronomy and Astrophysics*, **564**:A95

Pinilla, P., Benisty, M., & Birnstiel, T. 2012a, Ring shaped dust accumulation in transition disks, *Astronomy and Astrophysics*, **545**:A81

Pinilla, P., Birnstiel, T., Ricci, L., et al. 2012b, Trapping dust particles in the outer regions of protoplanetary disks, *Astronomy and Astrophysics*, **538**:A114

Pinilla, P., Birnstiel, T., & Walsh, C. 2015, Sequential planet formation in the HD 100546 protoplanetary disk?, *Astronomy and Astrophysics*, **580**:A105

Pinilla, P., Natta, A., Manara, C. F., et al. 2018, Resolved millimeter-dust continuum cavity around the very low mass young star CIDA 1, *Astronomy and Astrophysics*, **615**:A95

Pinilla, P., Pascucci, I., & Marino, S. 2020, Hints on the origins of particle traps in protoplanetary disks given by the M_{dust} - $M_{\star}$ relation, *Astronomy and Astrophysics*, **635**:A105

Pinte, C., Price, D. J., Ménard, F., et al. 2018, Kinematic Evidence for an Embedded Protoplanet in a Circumstellar Disk, *The Astrophysical Journal Letters*, **860**:L13

Piso, A.-M. A., Youdin, A. N., & Murray-Clay, R. A. 2015, Minimum Core Masses for Giant Planet Formation with Realistic Equations of State and Opacities, *The Astrophysical Journal*, **800**:82

Pollack, J. B., Hubickyj, O., Bodenheimer, P., et al. 1996, Formation of the giant planets by concurrent accretion of solids and gas, *icarus*, **124**:62–85

Poppe, T., Blum, J., & Henning, T. 2000, Analogous Experiments on the Stickiness of Micron-sized Preplanetary Dust, *The Astrophysical Journal*, **533**:454–471

Powell, D., Murray-Clay, R., & Schlichting, H. E. 2017, Using Ice and Dust Lines to Constrain the Surface Densities of Protoplanetary Disks, *The Astrophysical Journal*, **840**:93

Powell, D., Zhang, X., Gao, P., & Parmentier, V. 2018, Formation of Silicate and Titanium Clouds on Hot Jupiters, *The Astrophysical Journal*, **860**:18

Rafikov, R. R. 2006, Atmospheres of Protoplanetary Cores: Critical Mass for Nucleated Instability, *The Astrophysical Journal*, **648**:666–682

Rafikov, R. R. 2016, Protoplanetary Disk Heating and Evolution Driven by Spiral Density Waves, *The Astrophysical Journal*, **831**:122

Ribas, Á., Bouy, H., & Merín, B. 2015, Protoplanetary disk lifetimes vs. stellar mass and possible implications for giant planet populations, *Astronomy and Astrophysics*, **576**:A52

Ribas, Á., Merín, B., Bouy, H., & Maud, L. T. 2014, Disk evolution in the solar neighborhood. I. Disk frequencies from 1 to 100 Myr, *Astronomy and Astrophysics*, **561**:A54

Ricci, L., Testi, L., Natta, A., et al. 2010, Dust properties of protoplanetary disks in the Taurus-Auriga star forming region from millimeter wavelengths, *Astronomy and Astrophysics*, **512**:A15

Rice, W. K. M., Armitage, P. J., Wood, K., & Lodato, G. 2006, Dust filtration at gap edges: implications for the spectral energy distributions of discs with embedded planets, *Monthly Notices of the Royal Astronomical Society*, **373**:1619–1626

Rosotti, G. P., Booth, R. A., Tazzari, M., et al. 2019a, On the millimetre continuum flux-radius correlation of proto-planetary discs, *Monthly Notices of the Royal Astronomical Society*, **486**:L63–L68

Rosotti, G. P., Tazzari, M., Booth, R. A., et al. 2019b, The time evolution of dusty protoplanetary disc radii: observed and physical radii differ, *Monthly Notices of the Royal Astronomical Society*, **486**:4829–4844

Safronov, V. S. 1969, Evoliutsiia doplanetnogo oblaka.

Sanchis, E., Testi, L., Natta, A., et al. 2021, Measuring the ratio of the gas and dust emission radii of protoplanetary disks in the Lupus star-forming region, *Astronomy and Astrophysics*, **649**:A19

Schäfer, U., Yang, C.-C., & Johansen, A. 2017, Initial mass function of planetesimals formed by the streaming instability, *Astronomy and Astrophysics*, **597**:A69

Schwarz, K. R., Bergin, E. A., Cleeves, L. I., et al. 2016, The Radial Distribution of H_2 and CO in TW Hya as Revealed by Resolved ALMA Observations of CO Isotopologues, *The Astrophysical Journal*, **823**:91

Seizinger, A., & Kley, W. 2013, Bouncing behavior of microscopic dust aggregates, *Astronomy and Astrophysics*, **551**:A65

Seizinger, A., Speith, R., & Kley, W. 2013, Tensile and shear strength of porous dust agglomerates, *Astronomy and Astrophysics*, **559**:A19

Shakura, N. I., & Sunyaev, R. A. 1973, Black holes in binary systems. Observational appearance., *Astronomy and Astrophysics*, **24**:337–355

Shlosman, I., & Begelman, M. C. 1989, Evolution of Self-Gravitating Accretion Disks in Active Galactic Nuclei, *The Astrophysical Journal*, **341**:685

Siess, L., Dufour, E., & Forestini, M. 2000, An internet server for pre-main sequence tracks of low- and intermediate-mass stars, *Astronomy and Astrophysics*, **358**:593–599

Simon, J. B., Armitage, P. J., Li, R., & Youdin, A. N. 2016, The Mass and Size Distribution of Planetesimals Formed by the Streaming Instability. I. The Role of Self-gravity, *The Astrophysical Journal*, **822**:55

Stammler, S. M., & Birnstiel, T. 2022, DustPy: A Python Package for Dust Evolution in Protoplanetary Disks, *The Astrophysical Journal*, **935**:35

Stammler, S. M., Drążkowska, J., Birnstiel, T., et al. 2019, The DSHARP Rings: Evidence of Ongoing Planetesimal Formation?, *The Astrophysical Journal Letters*, **884**:L5

Stoll, M. H. R., & Kley, W. 2014, Vertical shear instability in accretion disc models with radiation transport, *Astronomy and Astrophysics*, **572**:A77

Stoll, M. H. R., & Kley, W. 2016, Particle dynamics in discs with turbulence generated by the vertical shear instability, *Astronomy and Astrophysics*, **594**:A57

Stoll, M. H. R., Picogna, G., & Kley, W. 2017, Planet-disc interaction in laminar and turbulent discs, *Astronomy and Astrophysics*, **604**:A28

Takeuchi, T., & Lin, D. N. C. 2002, Radial Flow of Dust Particles in Accretion Disks, *The Astrophysical Journal*, **581**:1344–1355

Tazaki, R., Lazarian, A., & Nomura, H. 2017, Radiative Grain Alignment In Protoplanetary Disks: Implications for Polarimetric Observations, *The Astrophysical Journal*, **839**:56

Tazaki, R., Tanaka, H., Okuzumi, S., Kataoka, A., & Nomura, H. 2016, Light Scattering by Fractal Dust Aggregates. I. Angular Dependence of Scattering, *The Astrophysical Journal*, **823**:70

Tazzari, M., Clarke, C. J., Testi, L., et al. 2021, Multiwavelength continuum sizes of protoplanetary discs: scaling relations and implications for grain growth and radial drift, *Monthly Notices of the Royal Astronomical Society*, **506**:2804–2823

Teague, R., Bae, J., Bergin, E. A., Birnstiel, T., & Foreman-Mackey, D. 2018, A Kinematical Detection of Two Embedded Jupiter-mass Planets in HD 163296, *The Astrophysical Journal Letters*, **860**:L12

Terebey, S., Shu, F. H., & Cassen, P. 1984, The collapse of the cores of slowly rotating isothermal clouds, *The Astrophysical Journal*, **286**:529–551

Testi, L., Birnstiel, T., Ricci, L., et al. 2014, Dust Evolution in Protoplanetary Disks, in *Protostars and Planets VI, ed. H. Beuther, R. S. Klessen, C. P. Dullemond, & T. Henning*, p. 339

Thamm, E., Steinacker, J., & Henning, T. 1994, Ambiguities of parametrized dust disk models for young stellar objects., *Astronomy and Astrophysics*, **287**:493–502

Tobin, J. J., Sheehan, P. D., Megeath, S. T., et al. 2020, The VLA/ALMA Nascent Disk and Multiplicity (VANDAM) Survey of Orion Protostars. II. A Statistical Characterization of Class 0 and Class I Protostellar Disks, *The Astrophysical Journal*, **890**:130

Toomre, A. 1964, On the gravitational stability of a disk of stars., *The Astrophysical Journal*, **139**:1217–1238

Trapman, L., Ansdell, M., Hogerheijde, M. R., et al. 2020, Constraining the radial drift of millimeter-sized grains in the protoplanetary disks in Lupus, *Astronomy and Astrophysics*, **638**:A38

Tripathi, A., Andrews, S. M., Birnstiel, T., & Wilner, D. J. 2017, A millimeter Continuum Size–Luminosity Relationship for Protoplanetary Disks, *The Astrophysical Journal*, **845**:44

Tsukagoshi, T., Nomura, H., Muto, T., et al. 2016, A Gap with a Deficit of Large Grains in the Protoplanetary Disk around TW Hya, *The Astrophysical Journal Letters*, **829**:L35

Tsukagoshi, T., Muto, T., Nomura, H., et al. 2019, Discovery of An au-scale Excess in Millimeter Emission from the Protoplanetary Disk around TW Hya, *The Astrophysical Journal Letters*, **878**:L8

Turner, N. J., Fromang, S., Gammie, C., et al. 2014, Transport and Accretion in Planet-Forming Disks, in *Protostars and Planets VI, ed. H. Beuther, R. S. Klessen, C. P. Dullemond, & T. Henning*, p. 411

Tychoniec, Ł., Tobin, J. J., Karska, A., et al. 2018, The VLA Nascent Disk and Multiplicity Survey of Perseus Protostars (VANDAM). IV. Free-Free Emission from Protostars: Links to Infrared Properties, Outflow Tracers, and Protostellar Disk Masses, *Astrophysical Journal Supplement Series*, **238**:19

van der Marel, N., Dong, R., di Francesco, J., Williams, J. P., & Tobin, J. 2019, Protoplanetary Disk Rings and Gaps across Ages and Luminosities, *The Astrophysical Journal*, **872**:112

van der Marel, N., & Mulders, G. D. 2021, A Stellar Mass Dependence of Structured Disks: A Possible Link with Exoplanet Demographics, *Astronomical Journal*, **162**:28

van der Marel, N., van Dishoeck, E. F., Bruderer, S., et al. 2016, Resolved gas cavities in transitional disks inferred from CO isotopologs with ALMA, *Astronomy and Astrophysics*, **585**:A58 van der Marel, N., van Dishoeck, E. F., Bruderer, S., et al. 2013, A Major Asymmetric Dust Trap in a Transition Disk, *Science*, **340**:1199–1202

van der Marel, N., Williams, J. P., Picogna, G., et al. 2022, High-resolution ALMA observations of transition disk candidates in Lupus, *arXiv e-prints*, p. arXiv:2204.08225

Wada, K., Tanaka, H., Suyama, T., Kimura, H., & Yamamoto, T. 2008, Numerical Simulation of Dust Aggregate Collisions. II. Compression and Disruption of Three-Dimensional Aggregates in Head-on Collisions, *The Astrophysical Journal*, **677**:1296–1308

Wada, K., Tanaka, H., Suyama, T., Kimura, H., & Yamamoto, T. 2009, Collisional Growth Conditions for Dust Aggregates, *The Astrophysical Journal*, **702**:1490–1501

Weber, P., Benítez-Llambay, P., Gressel, O., Krapp, L., & Pessah, M. E. 2018, Characterizing the Variable Dust Permeability of Planet-induced Gaps, *The Astrophysical Journal*, **854**:153

Weidenschilling, S. J. 1977, Aerodynamics of solid bodies in the solar nebula., *Monthly Notices of the Royal Astronomical Society*, **180**:57–70

Wetherill, G. W., & Stewart, G. R. 1989, Accumulation of a swarm of small planetesimals, *Icarus*, **77**:330–357

Whipple, F. L. 1972, On certain aerodynamic processes for asteroids and comets, in *From Plasma to Planet, ed. A. Elvius*, p. 211

Windmark, F., Birnstiel, T., Güttler, C., et al. 2012, Planetesimal formation by sweep-up: how the bouncing barrier can be beneficial to growth, *Astronomy and Astrophysics*, **540**:A73

Youdin, A. N. 2011, The Exoplanet Census: A General Method Applied to Kepler, *The Astrophysical Journal*, **742**:38

Youdin, A. N., & Goodman, J. 2005, Streaming Instabilities in Protoplanetary Disks, *The Astrophysical Journal*, **620**:459–469

Youdin, A. N., & Lithwick, Y. 2007, Particle stirring in turbulent gas disks: Including orbital oscillations, *Icarus*, **192**:588–604

Zhang, K., Blake, G. A., & Bergin, E. A. 2015, Evidence of Fast Pebble Growth Near Condensation Fronts in the HL Tau Protoplanetary Disk, *The Astrophysical Journal Letters*, **806**:L7

Zhang, S., Zhu, Z., Huang, J., et al. 2018, The Disk Substructures at High Angular Resolution Project (DSHARP). VII. The Planet-Disk Interactions Interpretation, *The Astrophysical Journal Letters*, **869**:L47

Zhu, Z., Nelson, R. P., Dong, R., Espaillat, C., & Hartmann, L. 2012, Dust Filtration by Planet-induced Gap Edges: Implications for Transitional Disks, *The Astrophysical Journal*, **755**:6

Zhu, Z., Zhang, S., Jiang, Y.-F., et al. 2019, One Solution to the Mass Budget Problem for Planet Formation: Optically Thick Disks with Dust Scattering, *The Astrophysical Journal Letters*, **877**:L18

Ziampras, A., Ataiee, S., Kley, W., Dullemond, C. P., & Baruteau, C. 2019, The impact of planet wakes on the location and shape of the water iceline in a protoplanetary disk, *arXiv e-prints*, arXiv:1910.08560 [astro-ph.EP]

Zormpas, A., Birnstiel, T., Rosotti, G. P., & Andrews, S. M. 2022, A large population study of protoplanetary disks. Explaining the millimeter size-luminosity relation with or without substructure, *Astronomy and Astrophysics*, **661**:A66

Zormpas, A., Picogna, G., Ercolano, B., & Kley, W. 2020, Solid accretion onto planetary cores in radiative disks, *Astronomy and Astrophysics*, **638**:A97

Zubko, V. G., Mennella, V., Colangeli, L., & Bussoletti, E. 1996, Optical constants of cosmic carbon analogue grains - I. Simulation of clustering by a modified continuous distribution of ellipsoids, *Monthly Notices of the Royal Astronomical Society*, **282**:1321–1329

Aknowledgments

As last part I leave the most important one. To express my gratitude to the people that made this possible and I could not start without thanking anyone else than my parents. Not only because they supported me, as they did with my brothers, during all my studies from high school until the start of my Ph.D., but most importantly because they gave me the freedom and the educational basis to choose my own path and follow my own desire even if this meant for me to live a couple of thousands of kilometers away. For every little expense, for every vacation they sacrificed then, they can certainly enjoy a beer now, whenever they visit.

To my advisor Til Birnstiel, the supervisor as they supposed to be. Who gave me the opportunity to work with him, and he was always there for every little question that I had, but also gave me the freedom to work on my own and develop on many aspects academically and professionally. For all the guidance, patience, hints, tips and tricks. For showing me that the Ph.D. can be a relaxing and productive period in the life of a student. Maybe after this, I will find some time for one more plot, just let me know!

To Barbara Ercolano, who is the person that first believed in me during my Master's studies and continued to support me during the Ph.D., Grazie mille! I will most likely meet you on the slopes from now on!

I cannot leave out of this my office mates through the years. To Joanna, Sebastian, Matias, Kristina, Giovanni, Raphael, David, Tommaso, Joseph, Fabian and Thomas (annd Til again). For every tasty Tuesday, wonderful Wednesday, fancy Friday, biergarten group meetings, for every banter, for every USM (and not only) party and for the unlimited Instagram boomerangs. To external colleagues that inspired and helped me grow. To Giovanni Rosotti, for the collaboration, the countless meetings and great insights. To Kees Dullemond and the late Willy Kley, two remarkable teachers and scientists. To Sean Andrews, who with a few hundred comments pushed the paper on steroids.

And finally, to Ioanna. Who certainly made my academic life more difficult but made my life better.

Thank you!